MALAGASY CLIMATE VARIABILITY, CHARACTERISTICS, MODES, MECHANISMS, MODELLING, TELECONNECTION AND PREDICTION

A THESIS SUBMITTED TO THE SCHOOL OF GRADUATE STUDIES OF ADDIS ABABA UNIVERSITY IN PARTIAL FULFILLMENT OF THE REQUIREMENTS FOR THE DEGREE OF Ph.D. IN PHYSICS

Presented by

Tatiana Andry Arivelo

On December 14, 2009
Addis Ababa, Ethiopia

Approved by the board members:

Advisor: Dr Abebe Yeshanew	Signature:
Co-Advisor: Dr Araya Asfaw	Signature:
Chairman: Dr Fesseha Kassahun	Signature:
External Examiner: Pr Yuh-Lang Lin	Signature :
Internal Examiner: Dr Gizaw Mengistu	Signature:

Table of contents

List of Figures **4**

List of Tables **7**

General abstract **8**

Part I: Malagasy rainfall climatology **11**

Summary *11*

1. Introduction *11*
1.1. Meteorological pattern 11
1.2. Orographic influence 19

2. Data and methodology *20*
2.1. Data analysis 21
2.2. Methods 24

3. Results and discussions *26*
3.1. Seasonal cumulative precipitation analysis from 1950 to 2003 26
3.2. Monthly analysis of the regionalized rainfall data 31
3.3. Spatial representation of the Malagasy rainfall over 50 years 36

4. Conclusion *37*

Part II: Connectivity of Madagascar rainfall modes of variability **39**

Summary *39*

Chapter 1: Principal Component Analysis applied to Madagascar rainfall and its link with climate phenomena over the period 1951-2000 ..... **40**

1.1. Introduction *40*

1.2. Data used *41*
a) Rainfall 41
b) Data index values 42
c) Atmospheric dynamic variables 43

1.3. Methods *43*
a) Principal Component Analysis 44
b) Interpretation of PCA 46
c) Links mode of Malagasy rainfall 47
d) Dynamics atmospheric variables 47

1.4. Results and discussions *50*
1.4.1. Madagascar rainfall modes 50
1.5.1. Atmospheric circulations for Malagasy rainfall modes 59

1.6. Conclusion *70*

Chapter 2: Tropical cyclone role in the modification of Madagascar climate **72**

2.1. Introduction *72*

2.2. Data and Method ... *73*

2.3. Results ... *73*
a) Cyclogenesis scenario in the Indian Ocean basin ... 73
b) Tropical cyclone impact over Madagascar ... 76
c) Characteristics of the basin during the active phase of the austral summer season ... 79
d) Local contribution of the tropical cyclone ... 83

2.4. Conclusion ... *86*

Part III: Extreme value theory applied to the regional precipitation data of Madagascar ... 87

Summary ... *87*

Chapter 1: Standardized Precipitation Index ... 88

1.1-Introduction ... *88*

1.2. Data ... *89*

1.3. Methods ... *90*
a) Factors affecting rainfall anomalies ... 90
b) Standardized Precipitation Index ... 92

1.4 Results and interpretations ... *95*

1.5 Conclusion ... *98*

Chapter 2: Generalized extreme value and generalized Pareto distribution ... *100*

2.1. Introduction ... *100*

2.2. Data ... *101*

2.3. Method of analysis ... *101*
a) Fisher & Tippet theorem ... 101
b) Generalized Pareto Distribution ... 102
c) Modeling threshold excesses ... 104
d) Return Levels ... 110

2.4. Discussions and results ... *110*

2.5. Conclusion ... *117*

Part IV: Dynamics of Southern region rainfall ... 119

Summary ... *119*

Chapter 1: Atmospheric dynamics for dry episodes over Southern Madagascar ... 120

1. Introduction ... *120*

1.2. Data ... *121*
a) Precipitation data *(c.f. Part II, chap1, §1.2, a)* ... 121
b) Meteorological data ... 121

1.3. Methods ... *122*
a) Pearson correlation ... 122
b) Atmospheric variables (c.f. Part II, Chap 1, §1.3, b) ... 122

c) Composite analysis 122

1.4. Results *123*
a) Rainfall regimes 123
b) Causes of dry events in southern Madagascar 124
c) Modeling the governing dynamics for drought years 129

1.5. Conclusion *133*

Chapter 2: Comparison of predicted results by model with the observed rainfall data of southern Madagascar 134

2.1 Introduction *134*

2.2. Data *135*
a) Rainfall 135
b) The NCEP-NCAR reanalysis 135

2.3. Methods *136*
a) Teleconnection analysis and definition of key areas 136
b) Strategy in stepwise regression 137
c) Validation of prediction models 137

2.4. Results and discussions *138*
a) Target and predictors 138
b) Validation test 143
c) Extreme events analysis 145

2.5. Conclusion *147*

General Conclusion 149

Bibliography 153

Appendix 158

List of Figures

Figure 1 : Climatological mean 1 000 hPa wind pattern over the south Indian Ocean during 1952-2002 austral winter 12
Figure 2: Climatological mean 1000-hPa wind pattern over the south Indian Ocean during 1952-2002 austral summer. 13
Figure 3 : Climatological monthly mean of wind speed over the southwest Indian Ocean (10^oS-25^oS, 55^oE-65^oE). 14
Figure 4 : Climatological monthly mean of a) specific humidity flux and b) specific humidity over the southwest Indian Ocean (10^oS-25^oS, 55^oE-65^oE). 15
Figure 5 : Time-altitude climatological monthly mean of vertical a) humidity and b) pseudoequivalent potential temperature (KJ Kg-1) over Reunion Island (21^oS-55^oE)..... 16
Figure 6: Climatological monthly mean of specific humidity flux and large scale precipitation during a) austral winter and b) austral summer over Indian Ocean during 1952-2002 period. 17
Figure 7: Longitude-time climatological mean of 1000hPa wind speed during the period from 1952 to 2002 for 25°S-35°S latitude band geographical area. 18
Figure 8: Monthly mean of 1000-hPa meridional wind speed during the period 1952-2002 of the geographical area (0^oS-10^oS; 40^oE-55^oE)..... 18
Figure 9: Geographical map of Madagascar 19
Figure 10: Climatological monthly mean of vertical wind during a) austral winter and b) austral summer over Indian Ocean. 20
Figure 11: Locations of the rainfall stations..... 21
Figure 12: Evolution of the number of the stations from 1926 to 2003..... 22
Figure 13: Evolution in time of the missing data of the cumulative rainfall between 56 stations22
Figure 14: Final network which responds to the criteria requested 24
Figure 15: Average summer rainfall season from the north eastern region 27
Figure 16: Average summer rainfall season from the eastern coastal region 28
Figure 17: Average summer rainfall season from the south eastern region. 28
Figure 18: Average summer rainfall season from the south western region. 29
Figure 19: Average summer rainfall season from the highland region. 30
Figure 20: Average summer rainfall season from the northwest coastal region. 30
Figure 21: Density of the probability rainfall distribution of the north eastern coast of Madagascar in the period 1950-2002. 32
Figure 22: Density of the probability rainfall distribution of the Middle Eastern coast of Madagascar in the period 1950-2002. 32
Figure 23: Density of the probability rainfall distribution of the south eastern coast of Madagascar in the period 1950-2002. 33
Figure 24: Density of the probability rainfall distribution of the northern highland of Madagascar in the period 1950-2002. 34
Figure 25: Density of the probability rainfall distribution of the southern highland of Madagascar in the period 1950-2002. 35
Figure 26: Density of the probability rainfall distribution of the south western coast of Madagascar in the period 1950-2002. 36
Figure 27: Monthly mean precipitation based on the climatogical period 1951-2003 37
Figure 28: The spatial and temporal pattern of the first component. (“Temps”=time)..... 51
Figure 29: The spatial and temporal pattern of the second component. 52
Figure 30: The spatial and temporal pattern of the third component. 54
Figure 31: The time course of the first component plotted with the QBO index. 55
Figure 32: The time course of the first component plotted with the TC index. 56

Figure 33: The time course of the second component plotted with the ENSO index. 57
Figure 34: The time course of the first component plotted with the SOI index..... 58
Figure 35: Global tropical SST composite pattern (^{o}C) of the first mode..... 60
Figure 36: Regional composite wind circulation at 200mb related to the first mode. 61
Figure 37: Tropical and extra-tropical flows are co-operating to generate low-level convergent and upper level divergent flows to produce strong ascent with respect to the continuity equation. 62
Figure 38: Regional composite omega pattern in the mid level..... 62
Figure 39: Regional Composite OLR pattern related to the first mode illustrating convective activity for negative values. 63
Figure 40: Regional composite specific humidity pattern in the mid level linked to the leading mode. 63
Figure 41: Leading mode composite upper Velocity Potential pattern significantly defining contrast between the Indian Ocean and the Pacific Ocean..... 64
Figure 42: Global tropical SST composite pattern (^{o}C) of the second mode. 65
Figure 43: Regional composite wind circulation in the upper level. 65
Figure 44: Regional composite OLR pattern. 66
Figure 45: Regional composite specific humidity pattern in the mid level. 66
Figure 46: Regional Composite surface precipitable water pattern. 67
Figure 47: Global tropical SST composite pattern (^{o}C). 67
Figure 48: Regional composite wind circulation pattern in the upper level. 68
Figure 49: Regional composite specific humidity pattern in the mid level. 69
Figure 50: Global Composite OLR pattern. 69
Figure 51: Composite upper Velocity Potential pattern significantly defining contrast between the Indian Ocean and the Pacific Ocean..... 70
Figure 52: Cyclonic activities from 1979 to 2004: Geographical distribution (Bessafi M. and M.C. Wheeler, 2005). 75
Figure 53: Cyclonic activities from 1979 to 2004: Number of cyclogenesis (Bessafi M. and M.C. Wheeler, 2005). 75
Figure 54: Storms and tropical cyclones hitting Madagascar from 1951 to 2003. 76
Figure 55: Trend of the Malagasy tropical cyclone. 77
Figure 56: Mean Composite Patterns between two successive 25 years climatology time period: a) Sea Surface Temperature, b) Outgoing Longwave Radiation, c) Mid-level Omega. 78
Figure 57: Storms and tropical cyclones hitting Madagascar during the summer season. 79
Figure 58: January Mean Composite Patterns for 1951-2003 climatology time period: a) Low-level wind vector, b) Outgoing Longwave Radiation, c) Mid-level specific humidity. 80
Figure 59: January Mean Composite Patterns for 1951-2003 climatology time period: a) Low-level wind vector, b) Outgoing Longwave Radiation, c) Mid-level Omega. 81
Figure 60: February Mean Composite Patterns for 1951-2003 climatology time period: a) Low-level wind vector, b) Sea Surface Temperature, c) Mid-level Omega. 82
Figure 61: Malagasy standardized regional rainfall combined with the tropical cyclone indices in the period 1951 to 2000..... 84
Figure 62: Mean Composite Patterns for 1951-2003 climatology time period considering tropical cyclone years coinciding to wet and dry events: a) Sea Surface Temperature, b) Outgoing Longwave Radiation, c) Upper-level divergence..... 85
Figure 63: Location of 59 coordinates and their subdivisions 90
Figure 64: Probability density function. 93
Figure 65: A plot of January SPI values is shown for 9 different regions in Madagascar. 96
Figure 66: Plot of the seasonal SPI (Nov-Apr) and the12-year SPI (Jan-Dec) of the region 2.. 97

Figure 67: Plot of the seasonal SPI (Nov-Apr) and the 12-year SPI(Jan-Dec) of the region 3.. 98
Figure 68: Example of mean excesses plots against threshold 106
Figure 69: Hill estimate plots of the tail index against different threshold..... 107
Figure 70: QQ-plot for data against exponential distribution without excluding any point. ... 109
Figure 71: Estimates of shape parameter, ξ, at different number of exceedances for the nine regions. 113
Figure 72: Regional rainfall data estimates of quantile 99.9 as a function of exceedances. Dotted lines are upper and lower 95 percent confidence intervals..... 114
Figure 73: Point estimate at the tail 0.999th quantile estimate and 95 percent confidence interval of the region 1 rainfall data. 115
Figure 74: Return level plot for monthly rainfall time series for each region. 117
Figure 75: Southern Madagascar averaged rainfall time series from six stations during the rainy season depicting the extreme events (dry and wet years). 122
Figure 76: Regionalization of Madagascar with respect to the topography and its precipitation.124
Figure 77: Vector winds (m/s) at 850Pa for drought years in the rainy season of southern region..... 125
Figure 78: Surface zonal momentum flux averaged over (0-40^{o}S; 30^{o}E-70^{o}E)..... 126
Figure 79: Low level specific humidity for dry minus wet episodes (g/kg). 126
Figure 80: Upper level divergence flow for dry minus wet episodes averaged over (0-40^{o}S; 30^{o}E-70^{o}E)..... 127
Figure 81: Composite OLR pattern illustrating positive values for dry minus wet episodes. . 127
Figure 82: Mid level troposphere Geopotential Height (m) illustrating descending motion. .. 128
Figure 83: Mid level tropospheric composite Omega (Pa/s) showing the existence of downward motion responsible for the dry condition in the key area i.e. the southern Madagascar..... 128
Figure 84: Circulation constructed based on the low and upper-level vector winds indicating the dynamical mechanisms for dry condition over south Madagascar. 129
Figure 85: Southern Precipitation index plotted with the optimal combined variables u_850, u_200 and OLR 131
Figure 86: Southern Precipitation index plotted with the optimal combined variables geop, OLR and u_850. 131
Figure 87: Southern Precipitation index plotted with the optimal combined variables spec_850, Omega and OLR. 131
Figure 88: Storm track every 4 hours over the southern Indian Ocean from 11 to 19 January 1970. 132
Figure 89: Storm track every 4 hours over the southern Indian Ocean from 9 February until 2 March 1970 132
Figure 90: Interannual variations sequence plots of the observed and predicted rainfall based on the best predictors at 3-month leads. 140
Figure 91: Interannual variations sequence plots of the observed and predicted rainfall based on the best predictors at 6-month leads. 140
Figure 92: Global Outgoing Longwave Radiation environment three months before the austral summer season among with the strategic equatorial key areas. 141
Figure 93: Global Sea surface temperature environment six months before the austral summer season and description of the key area located in the north pacific ocean. 142
Figure 94: Global Sea surface temperature environment three months before the austral summer season and north pacific key area. 142
Figure 95: Predicted rainfall at 3-month lead tendency over 50 climatology years of the southern region.. 144

Figure 96: Predicted rainfall at 6-month lead tendency over 50 climatology years of the southern region.. 144
Figure 97: Southern rainfall scatter plots combining the observed and the predicted datasets.145
Figure 98: Regional composite low level wind vector related to the southern extreme events146
Figure 99: Regional composite OLR derived from to the southern extreme events. 146
Figure 100: Regional composite surface precipitable water linked to the southern extreme events. 147

List of Tables

Table 1: List and information about the final stations 23
Table 2: List of the PCs composite years 59
Table 3: Correlation table between regional rainfall and tropical cyclone (TC) indices 83
Table 4: Selected threshold per station 111
Table 5: Estimated value at the tail 0.999th quantile estimate at the lower and upper confidence band of each defined region. 115
Table 6: Cross-correlation table of the atmospherics variable time series 130
Table 7: Three best combinations of the atmospheric variables based on their correlation. . 130
Table 8: Candidate predictors: representation and domains 138
Table 9: Partial correlation between the candidate predictors and the target variable. 139

General Abstract

Actually, the water resource becomes increasingly limited and difficult to exploit. Their quantity on the Malagasy territory is unevenly spread; it is relatively abundant in the East coast while the area of South-east presents a periodic situation vulnerable to the dryness. The water resource is especially conditioned by precipitations in the form of rain having a great effect in society's life.

Prior to different tasks linked to the Malagasy rainfall, better understanding of the meteorological and orographical influences are very useful as Madagascar is situated in the southwest zone of the Indian Ocean closed to the African continent with a channel sea on the West (Channel of Mozambica) and the Indian Ocean on the East, located between 12° and 25° 30' of southern latitude, crossed by the austral Capricorn tropic. It is an Island whose transversal profile of its orography is marked by a strong asymmetry of slopes: in the East, the altitude rises quickly and reaches the central areas through a sharp cliff. Its Eastern coastal plains are very narrow. However, in the West the relief declines progressively attaining low stretched areas.

In the synoptic scale, tropical weather is prevailing in this island with dry season during the austral winter (May to October) and wet season during the austral summer (November to April). Strong trade winds and extra tropical perturbations are the most dominant meteorological patterns prevailing in the island.

Despite the establishment of the rainfall climatology over Madagascar gaps are still identified in that previous analysis for instance the spatial and temporal variation rainfall with tremendous spatial gradient of rainfall in all directions. It is therefore vital to optimally compute space-time modes of variability of the country by the mean of the Principal Component Analysis (PCA) as this type of research is not yet attempted for Madagascar despite its popularity. Most importantly, salient factors that determine these modes are

investigated to better understand the rainfall mechanisms in the country using the worldwide PCA tools.

Therefore, tropical cyclone having mutual relationship with the leading mode component opens an interesting research field on the role of tropical cyclone in the modification of Madagascar climate and its contribution in different regions during the rainy season.

Furthermore, extreme precipitation events in Madagascar can be related to a variety of catastrophic events including drought, famine, flooding, and the spread of disease. It is important to attempt to anticipate when these extreme events are likely to (Doncques, 1975) occur so that disaster relief efforts can be implemented which could reduce the potential impacts of these extreme events. In order to predict and prepare areas that may be susceptible to food shortages as a result of rainfall anomalies, SPI (Standardized Precipitation Index) and EV (Extreme Value) Analysis applied to the precipitation records are adopted. Specifically, the aim is not only to study the quantile of Madagascar rainfall record but also its tails and risk measures using the Extreme Value theory. Another important issue of this analysis is the return level of the excess of the precipitation record in order to extract the main temporal pattern of severe rain which occurred in Madagascar.

As a crucial natural resource for Madagascar, rainwater is unevenly distributed. Some regions are extremely ‘fragilized’ by the cyclone passage that provokes important floods. Other areas are recurrently hit by drought especially the southern part of the country, but in the other regions it seems periodic. In fact, the extreme South of the island is a semi-arid area where the annual average precipitation is less than 600 mm with 9 to 11 months water deficiency. So, whatever classification adopted and criteria employed, the South remains as the driest region (Doncques, 1975). This study is devoted to understanding the dynamics of dry events in the atmosphere over the southern part of Madagascar. The study

reveals that Southern Madagascar rainfall during the austral summer season depends on quantitative dynamical atmospheric variables. It is with this simple conceptual framework that we manage to predict the seasonal mean rainfall during its active phase on the relative contribution of these externally forced components. Moreover, it is important to develop an early warning system for rainfall variability based on a sound scientific understanding of its causes. This step of analysis considers which components of the ocean-atmosphere system contribute to its water resource then it compares the predicted result by model with the observed datasets of southern rainfall. Finally, it is aimed to give contribution to the predictability of Malagasy rainfall through applied climatology.

Part I: Malagasy rainfall climatology study

Summary

Climatologic study in terms of precipitation over a longer period of time provides a better understanding and a mean to check how much the climate fluctuates from one decade or century to the next. For the case of Madagascar, various techniques have been applied to the rainfall records from the Meteorology Office of Antananarivo after making some restitution of the gaps in order to have the climatology. Prior to the meteorological field and the orography feature, Malagasy rainfall climatology was characterized by the seasonal cycle of monsoon which embodies the ITCZ (Inter Tropical Convergence Zone). On the other hand, strong trade winds originated from the extra-tropical anti-cyclonical circulation located in the south-west of the Indian Ocean directed to the sharp relief along the eastern coast appears to have a great influence in the rainfall climatology of this island during the winter season.

1. Introduction

1.1. Meteorological pattern

In order to have a better understanding of the rainfall task, some characteristics about Madagascar's geography are introduced. The main meteorological patterns prevailing over this big island during the year are associated with its orographic feature. Madagascar is an island mostly situated in the tropical latitude except for its southern part which is in the subtropical region. It is located in the southwest zone of the Indian Ocean to the African continent with Channel of Mozambica on the west and the Indian Ocean on the East.

In the synoptic scale, tropical weather is prevailing in this island with dry season during the austral winter (May to October) and wet season during the austral summer

(November to April). During the austral winter, strong trade winds and extra-tropical perturbations are the most dominant meteorological patterns prevailing in the island according to the mean flow of the wind detected at 1 000 hPa level of the atmospheric layer for the 1952-2002 periods (Fig. 1). In fact, wind field reanalysis data from the European Centre for Medium-Range Weather Forecasts (ECMWF) are used here.

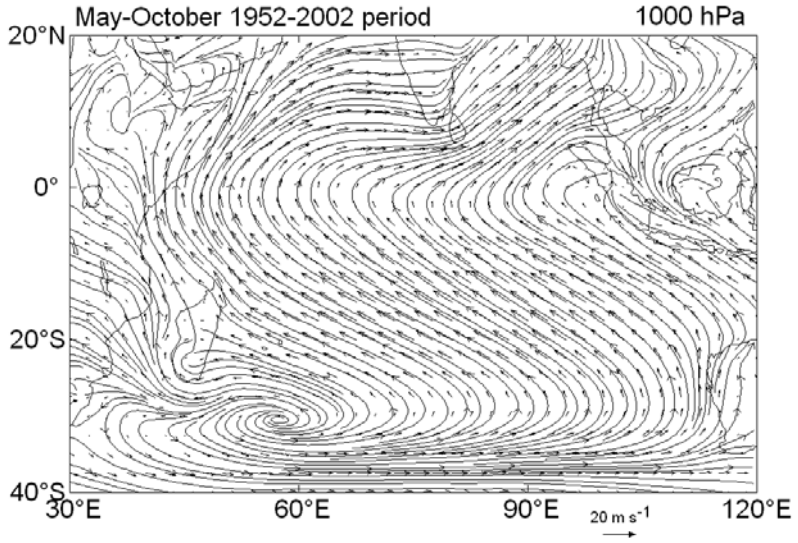

Figure 1: Climatological mean 1 000 hPa wind pattern over the south Indian Ocean during 1952-2002 austral winter

Trade winds are well-known as south-east flow associated with the counterclockwise circulation of the Mascareign's anticyclone which is located in the westernmost geographical position (55°E – 35°S) during the austral winter. During this period of the year, cross equatorial trade winds are deflected along the Somalia coast to northwest winds (northern summer monsoon) over Arabian Sea and Indian Continent. There are only trade wind deflected flows toward northwest: no convergence appears in Fig. 1 at 1000 hPa. Over southwest Indian Ocean wind patterns are split by Madagascar Island which in turn deflects the trade winds to a most northerly wind component in the northern part of the island and a slightly zonal component in the south. Moreover, Mozambica Channel experiences southeastward flow of the split trade winds with a cyclonic component in the south region.

In counterpart during the wet season deep convection and rainfall concerns globally the island along the southernmost location of ITCZ associated with cross equatorial monsoon flux in the northwest, the trade wind on the East, depression in the channel of Mozambica. In fact, the mean motion of the wind located at 1 000 hPa during the period 1952-2002 from November to April illustrates depression which has an effect on the zonal circulation. More precisely, during the austral summer season, the ITCZ is in its southernmost geographical location (0-10°S) and Mascareign's anticyclone in its easternmost geographical location (80°E) as shown in Fig. 2. The flow pattern is slightly the same over the southwest Indian Ocean with a splitting flow over Madagascar. Nevertheless, there is a reverse wind over Arabian Sea with a strong northeast component prevailing the northern winter monsoon which concern Somalia, Tanzania and Mozambica coasts.

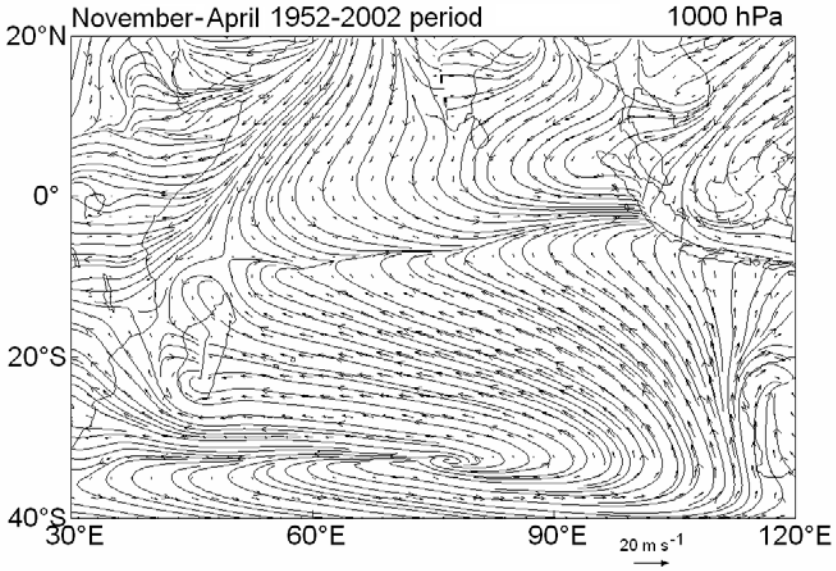

Figure 2: Climatological mean 1000-hPa wind pattern over the south Indian Ocean during 1952-2002 austral summer.

In addition to this climatological analysis, Mozambica channel flow pattern is different and more complex than shown in the previous figure. This would be partly explained by the

complex combination of deflected flow induced by Madagascar Island, the cross equatorial flow of the northern winter monsoon, the thermal sea condition during this period of the year.

As pointed out previously, trade winds are the main flow prevailing over south Indian Ocean and would be an important large scale meteorological factor for the rainfall budget over Madagascar. Nevertheless, this large scale southeast mean flow has an annual cycle as shown in Fig.3 with a strengthen wind speed during austral winter with a maximum of 10 m s^{-1} on July-August and a lowest intensity level of 4 m s^{-1} on January-February.

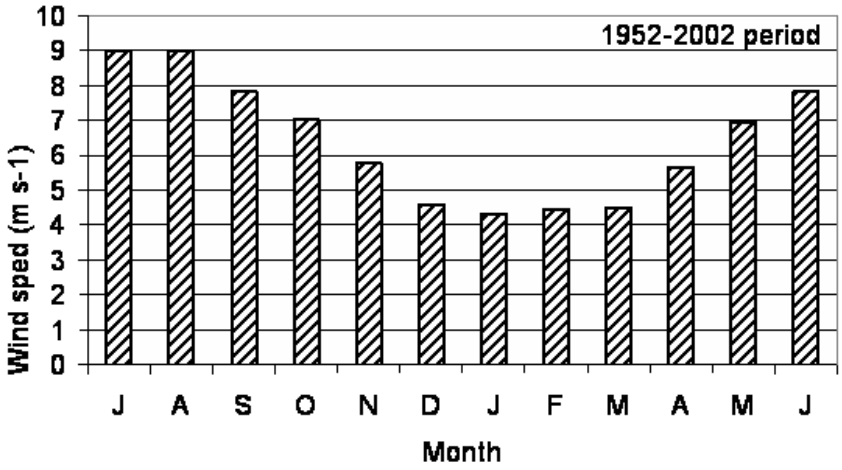

Figure 3 : Climatological monthly mean of wind speed over the southwest Indian Ocean (10^{o}S-25^{o}S, 55^{o}E-65^{o}E).

As mentioned, trade wind would be an important dynamical process in the Madagascar's rainfall budget during the year. The rate of water content brought by the southeast flow is shown on Fig. 4 which highlights some interesting points. First, the specific humidity vertical flux is positively correlated to the wind speed while the specific humidity is negatively correlated to the wind speed. During the austral summer the mean flow is less intense but the atmosphere is wetter. In terms of conversion of this water content in the air into rainfall process over Madagascar is partly ruled by the large scale thermodynamical

instability of the tropical atmosphere. Fig. 5a displays the monthly mean of humidity obtained by 214 radiosonde measurements over the southwest Indian Ocean (Reunion Island).

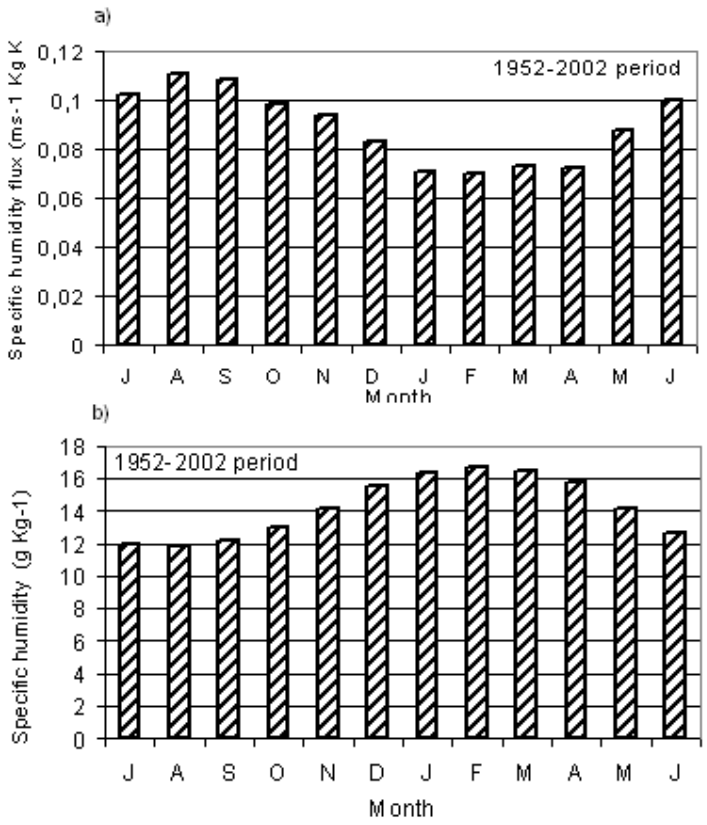

Figure 4 : Climatological monthly mean of a) specific humidity vertical flux and b) specific humidity over the southwest Indian Ocean (10^{o}S-25^{o}S, 55^{o}E-65^{o}E).

On average the whole free troposphere is wet during the austral summer and conversely high humidity is capped in the lower layer (0-3 km) by the trade wind inversion which inhibits the deep vertical motion. The atmosphere is more stable during austral winter and thus instability cannot develop deeply as shown in Fig. 5b.

Thus austral summer would be a favorable period for rainfall activity over Madagascar. Overall, the combined trade wind and monsoon during November-May period increase the instability of the wet atmosphere over the convergence area and would produce large scale precipitation.

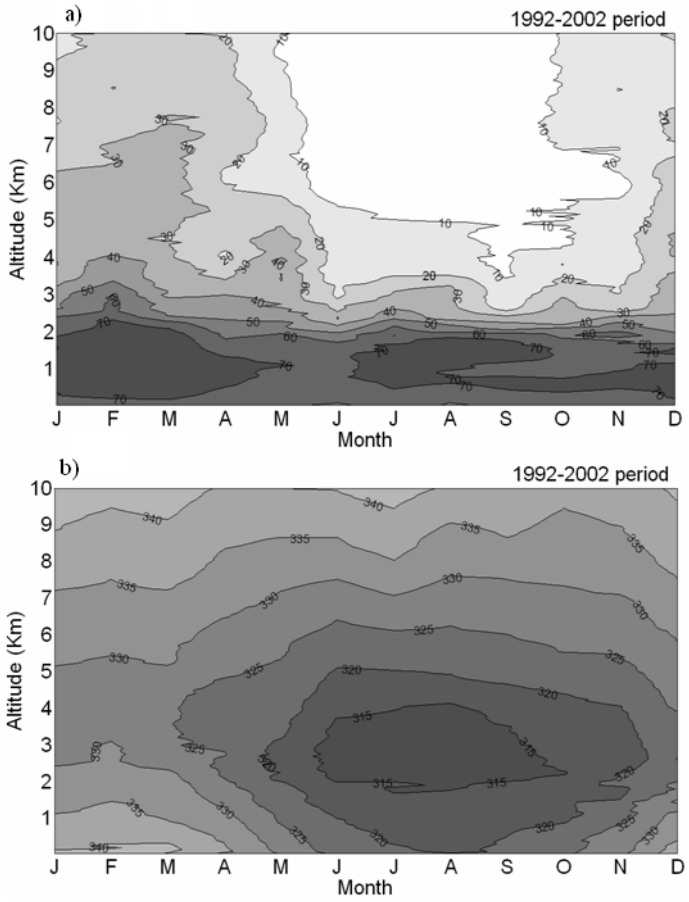

Figure 5 : Time-altitude climatological monthly mean of vertical a) humidity and b) pseudoequivalent potential temperature (KJ Kg^{-1}) over Reunion Island ($21^{o}S$-$55^{o}E$).

During austral summer period, deep convection is very active over ITCZ and is in its southernmost latitude location over Madagascar in comparison to the remaining area of the south Indian Ocean. As shown in Fig. 5b, the troposphere is more convectively unstable during the austral summer than the austral winter the lower troposphere is capped by a strong wind inversion around 2.5 km induced by the trade winds. However, La Reunion Island holds several world rainfall records during the period within 12 hours and 15 days which is the most remarkable meteorological phenomenon. It is also true that the essential fact of the rainfall over La Reunion is its spatio-temporal variation but the thing is the global dynamics and forces present (St Helena anti-cyclonic circulation, Trade winds, ITCZ) over both countries during the whole year are similar.

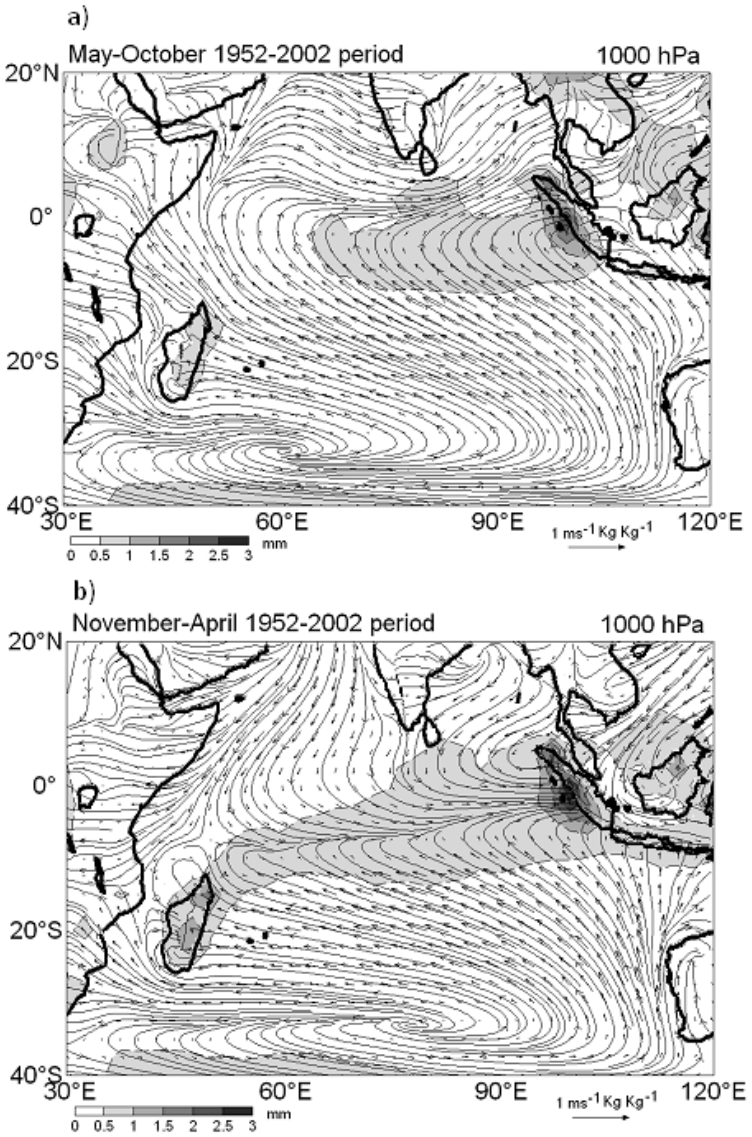

Figure 6: Climatological monthly mean of specific humidity flux (ms^{-1} Kg Kg) and large scale precipitation (mm) during a) austral winter and b) austral summer over Indian Ocean during 1952-2002 period.

During austral summer, deep convection can take place easily in combination with large scale horizontal transport and drive precipitation budget. This is shown in Fig. 6 where the large-scale precipitation pattern in combination with the specific humidity flux is noticed. The former delineates the geographical location of the ITCZ and the latter also shows this convergence zone and its contribution to the rainfall rate over Madagascar.

Extratropical perturbation regularly affects the southern region of Madagascar and the Mozambica channel during the year. This seasonal intrusion would contribute to weather and rainfall activity in this area as shown Fig.7. In addition to the trade wind, North of Madagascar is partly under the influence of monsoon regime during the year. Fig.8 confirms that during the austral summer there is a direct impact of the monsoon and thus would contribute to the rainfall activity of northern Madagascar.

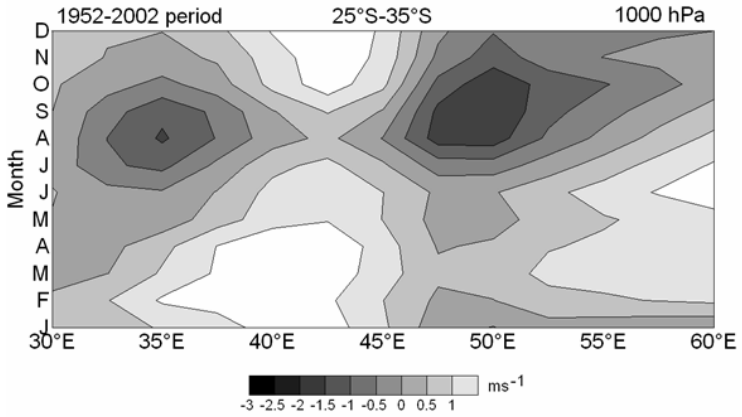

Figure 7: Longitude-time climatological mean of 1000hPa wind speed during the period from 1952 to 2002 for 25°S-35°S latitude band geographical area.

In resume, Madagascar is subjected to regionalized weather in the lower atmosphere especially in the troposphere as result of large-scale meteorological feature during the year.

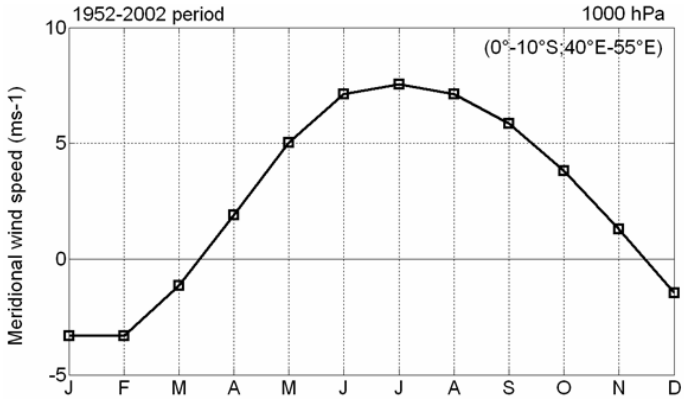

Figure 8: Monthly mean of 1000-hPa meridional wind speed during the period 1952-2002 of the geographical area (0^{o}S-10^{o}S; 40^{o}E-55^{o}E).

1.2. Orographic influence

In addition to the overview of the large-scale meteorological pattern prevailing over the south Indian Ocean, orography forcing would play an important role in the regional weather over Madagascar. This island cross profile is marked by a high asymmetry between the two sides as shown in Fig.9.

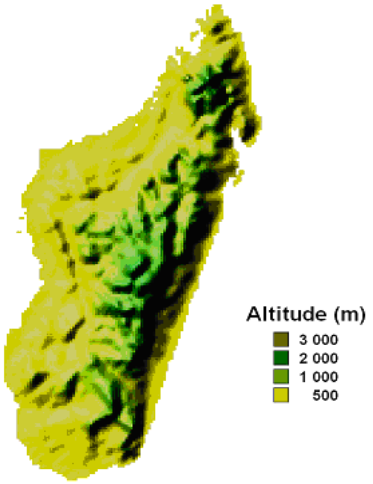

Figure 9: Topographic map of Madagascar

In the East, the height rises rapidly and reaches the central highland regions by a sharp sheer cliff. This highland region is delineated by a chain of mountains crossing along the east part of the island with altitudes up to 1600 m of maximum in the northern region.

Significant orographic effect is observed over Madagascar during both winter and summer season. This orographic influence constraints the trade wind to lift up, Fig.10 displays 700-hPa vertical velocity map over the Indian Ocean and most of the time induce orographic rainfall. Moreover, their eastern coastal plains are very tight. However in the western part, the relief falls gradually towards the lower regions more stretched out. Local dynamical and thermodynamical forcing like orographic processes is superimposed on the large-scale processes and contribute to the rainfall activity over Madagascar. However the data is too coarse to reflect orographic rain distribution.

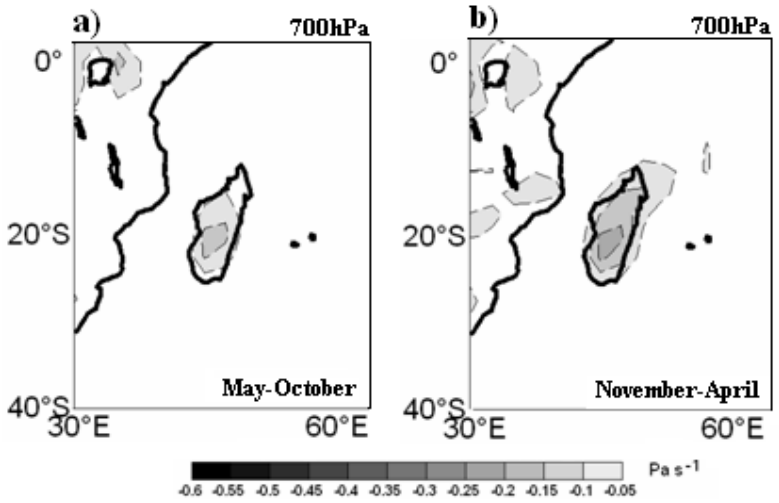

Figure 10: Climatological monthly mean from 1952 to 2002 of the vertical wind during the a) austral winter and b) the austral summer over Indian Ocean.

The meteorological and orographic influences of Madagascar could be found also in different literatures such as the geographical contribution to Madagascar climate study (Doncques, 1975), the contribution to the simulation of the flow over Madagascar's orography using a three-dimensional, mesoscale model (Ramiaranjanahary, Raholijao, Ratiarison, & Rabemanotrona, 2004). Hence, it must be very important to establish a recent monthly rainfall climatology which is the main goal of this study knowing that the period used for the last update was recorded from 1960 to 1990 registered from 111 stations documented from Biogeography of Madagascar (Jeanne, et al., 2002). However, this research will take account of the climatological period from 1951 to 2003 and will interpolate the best rainfall datasets over the 111 districts of Madagascar which was not still analysed before despite its utility in different sectors of the society. As outlines, this subject would be highlighted by analyzing the data and methodology followed by the results including the rainfall climatology of Madagascar.

2. Data and methodology

2.1. Data analysis

The study focuses on monthly cumulative precipitation over Madagascar using the data obtained from Malagasy Meteorology Administration at 56 stations. The stations are geographically well distributed; however, the southern reference rainfall record station is fewer than the other regions (Fig.11).

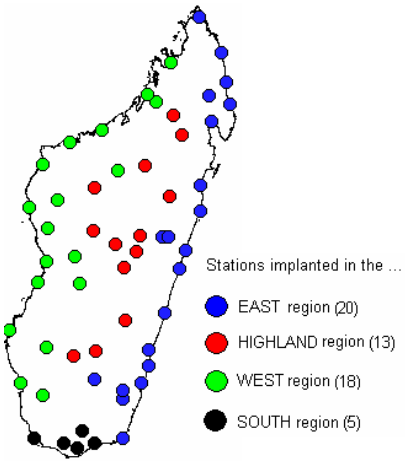

Figure 11: Locations of the rainfall stations

Simple plots of the number of the rainfall station and the percentage of the missing data versus time are dressed up in order to draw comments regarding the data aspect we have.

Thus the network size during the period 1926-2003 evolved from time to time with some major changes as indicated in Fig.12. Between 1926 and 1950, the network size increased steadily. An abrupt change occurred in 1951 when the network size was doubled. The network size reached its maximum in 1971; and since then slow decrease is observed with an abrupt decrease in 1981 following by a very small decline stabilizing at around 20 stations.

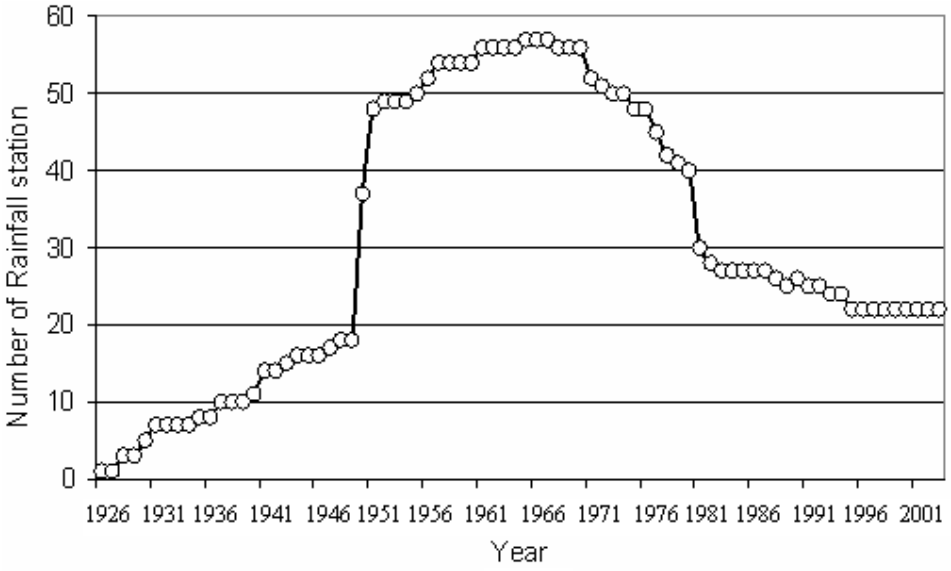

Figure 12: Evolution of the number of the stations from 1926 to 2003

In addition to that, the variations define graphically interesting periods. Besides, since each station is different in length, stations having long term period were chosen for analysis.

In other words, the network choice compromises between the homogeneity and the availability of the spatial distribution.

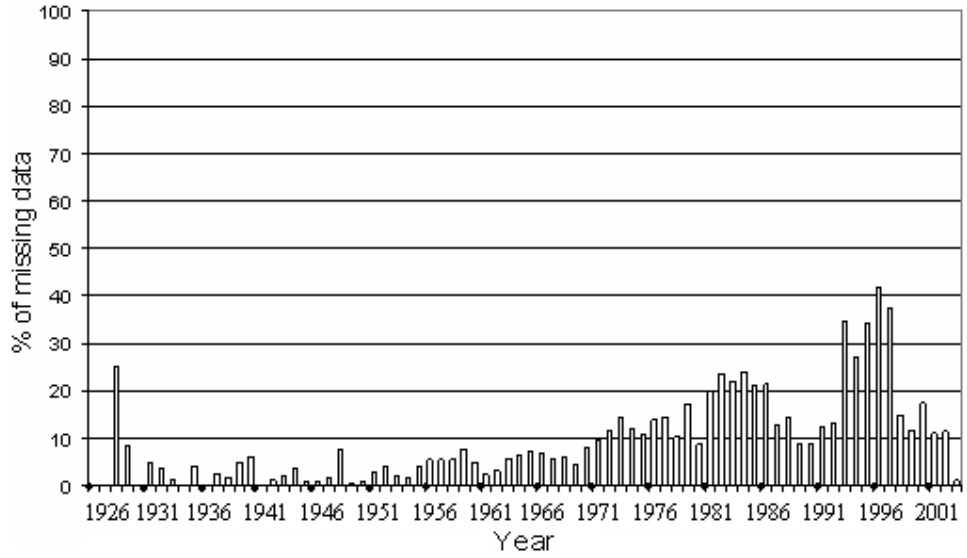

Figure 13: Evolution in time of the missing data of the cumulative rainfall between 56 stations

The temporal limit of the data is obtained by examining the figures which show the evolution of the number of the stations from 1926 to 2003 and the evolution in time of the percentage of missing data for the monthly cumulative rainfall (Fig. 13). Moreover, we have to relate these two figures (12&13) in order to extract the period with a high number of station and a relative low percentage of missing values.

Table 1: List and information about the final stations

Region	Station	Available period	Missing value
EAST (8)	ANTSIRANANA	1950-2003	9,86%
	VOHEMAR	1953-2003	7,14%
	SAMBAVA	1950-2003	7,43%
	TOAMASINA	1951-2003	18,29%
	MAHANORO	1950-2003	39,71%
	MANANJARY	1950-2003	10,00%
	FARAFANGANA	1950-2003	14,29%
	TOLAGNARO	1950-2003	1,71%
HIGHLAND (4)	AMBOHITSILAOZANA	1950-2003	27,00%
	ANTANANARIVO	1943-2003	7,14%
	FIANARANTSOA	1950-2003	4,29%
	RANOHIRA	1950-2003	8,57%
WEST (6)	ANTSOHIHY	1950-2003	14,00%
	MAHAJANGA	1950-2003	1,43%
	BESALAMPY	1950-2003	1,71%
	MAEVATANANA	1951-2003	2,71%
	MORONDAVA	1950-2003	2,85%
	MOROMBE	1950-2003	4,43%

As a result based on the criteria set which is availability of long term period data from 1950/51 to 2003, containing a few quantity of missing value with the exception of Mahanoro (39-71%) (Table 1), the number of stations reduces to 18. Thus, Fig. 14 illustrates the final network with respect to the criteria requested.

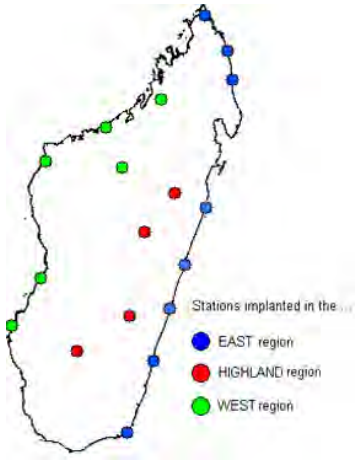

Figure 14: Final network which responds to the criteria requested

2.2. Methods

a) Descriptive statistics

In this study, descriptive statistics methods relevant to the atmospheric sciences which involve dense sampling both in time and space are used to organize and summarize the data.

The objective of this study is to associate correlated neighboring stations in order to determine the rainfall sub-regions and also to characterize the corresponding precipitation regimes.

b) Gamma distribution

In addition to the yearly cumulative precipitation over different regions of Madagascar, it is interesting to focus on shorter time scale (e.g. month) and perform regional rainfall analysis. Probability distribution is more appropriate to highlight representative rainfall activity of one typical year. Probably the simplest and the most intuitive means of comparing a fitted theoretical distribution to the underlying data is the superposition of the distribution and the histogram of the data however, gross departures from the data can be

readily seen in this way. Furthermore, there are a variety of continuous distributions that are bounded on the left by zero and positively skewed. One choice used for representing rainfall data is the gamma distribution defined by the Probability Density Function (or PDF) law: $f(x) = \left[(x/\beta)^{\alpha-1} / \beta^{\alpha}\Gamma(\alpha) \right] e^{-x/\beta}$ with $x, \alpha, \beta > 0$, where α is the distribution shape parameter while β the scale parameter. The quantity $\Gamma(\alpha)$ is a value of the standard mathematical function known as the gamma function, defined by the definite integral $\Gamma(\alpha) = \int_0^{\infty} t^{\alpha-1} e^{-t} dt$ (Wilks, 1995).

c) Inverse-Distance-Interpolation in Geographic Information System

Different methods could be used to fill in the missing values but the choice depends on how long and how far is the gap. The very simple method is expressed by this following relation: $P_m = \left(P_{m-1} + P_{m+1} \right) / 2$. In other words, the only one missing value in month *m* can attribute the mean between the rainfall records of the preceded month *(m-1)* and the rainfall record of the next month *(m+1)* (Duchiron, 2002).

However, another technical of missing value estimation is the spatial method 'Inverse-Distance-Interpolation' (Lynch & Schluze, 1995). Gridded datasets could be created by using Geographic Information System technology. Likewise, the most common method used for interpolation onto a regular grid from random spaced points is based on the computation of a weighted average of a representative sample points which would be written as follow $z_P = \sum_{i=1}^{n} z_i w_i / \sum_{i-1}^{n} w_i$ where z_p is the interpolated value, z_i is the value of precipitation at location (x_i, y_i), w_i is the weighting function and $n = n_b$ is the number of sample points. The weighting function w_i is given by $w_i = 1/d_i^2$ where d_i is the distance between z_p and z_i. In this method weights are calculated using a search radius and the weighting function for

$d_i / R < 1$ and $w_i = 0$ for $d_i / R \geq 1$ (Yoeli, 1975). Indeed, spatial aspect of the rainfall climatology over Madagascar can be tailored from this method. However, the choice of *R* depends on the density of the data points and should be chosen so that the sampling circle includes at least five sample points.

3. Results and discussions

3.1. Seasonal cumulative precipitation analysis from 1950 to 2003

The most significant feature of the precipitation in Africa is its interannual variability, since tropical temperature has a fairly low variance and wind speed is low when compared with the mid and high latitudes. Because most of the rain (about 85%) falls during the summer in Madagascar, this part of study will consider the summer precipitation as significant. Furthermore, it has been found that the regional mean state of the summer rainfall record should be between 900mm and 1800mm or more for the East region. Moving to the Highland region, summer precipitation is generally between 700 and 1400mm. And finally, according to the stations implanted in the West region, precipitation recorded during the summer season is between 250mm and 1400mm.

Therefore, the first group of station implanted in the East describes the Northeast region (Fig. 15). Every station has their monthly cumulated amount calculated from November to April. There is some consistency and homogeneity between the records. On average there is a slight decrease of the mean and variability of the precipitation towards the north. Moreover, the Northeast region experiences more than 1 m per year of cumulative rainfall.

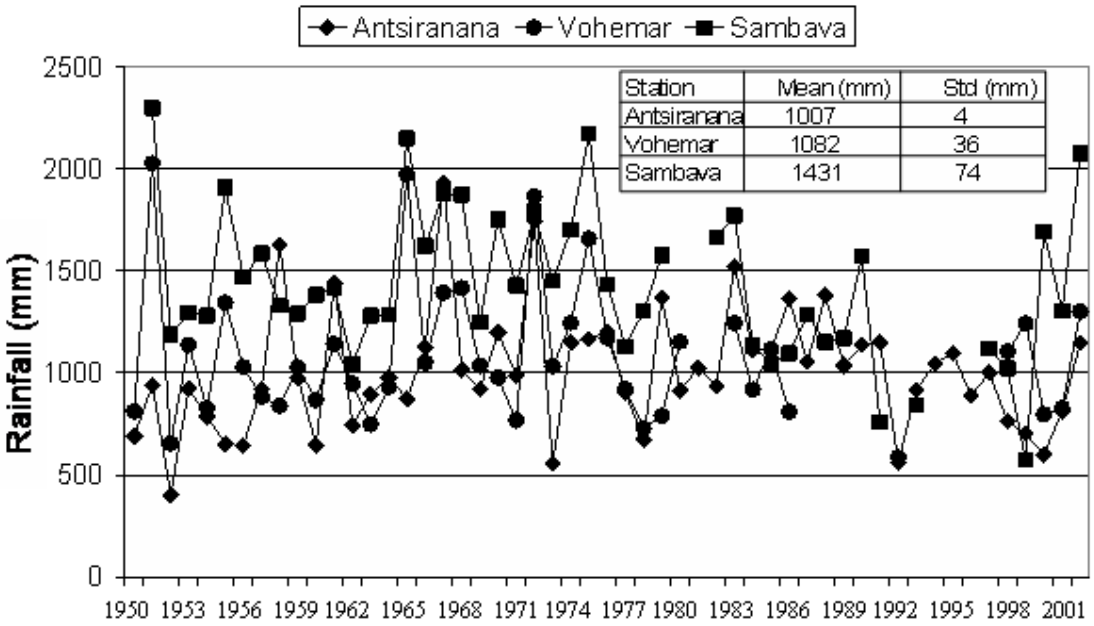

Figure 15: Average summer rainfall season from the Northeast region

Next, we will consider the East region, where the stations are localized in the coastal plains. As shown in Fig. 16, the mean and variability of the yearly rainfall rate in this region is approximately one and a half to two times greater than its northern counterpart. Along the eastern coast, rainfall records are homogeneous with regard to the mean and variability. As illustrated in Fig. 9, orography forcing plays an important role in the rainfall budget over this area which explains the rainfall increase when compared to the Northeast region.

The last eastern sub region is the south in which two stations have been selected. Farafangana station reveals (Fig. 17) an average rainfall activity similar to that of the eastern coast. Conversely, the second station record shows a significant decrease in rainfall rate which is half of Farafangana though both stations are at the same altitude (around 6m). Even though orography has a significant effect on the rainfall rate, the latitudinal location close to extratropical perturbation explains why the region is dry which is a common knowledge to the Malagasy people.

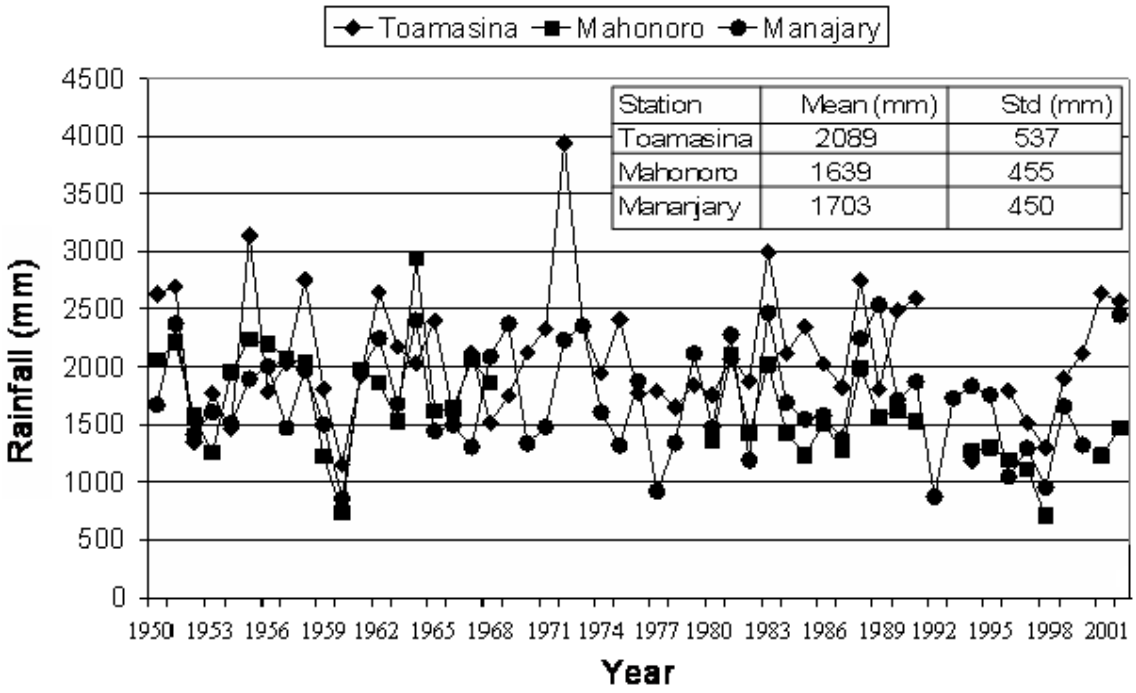

Figure 16: Average summer rainfall season from the eastern coastal region

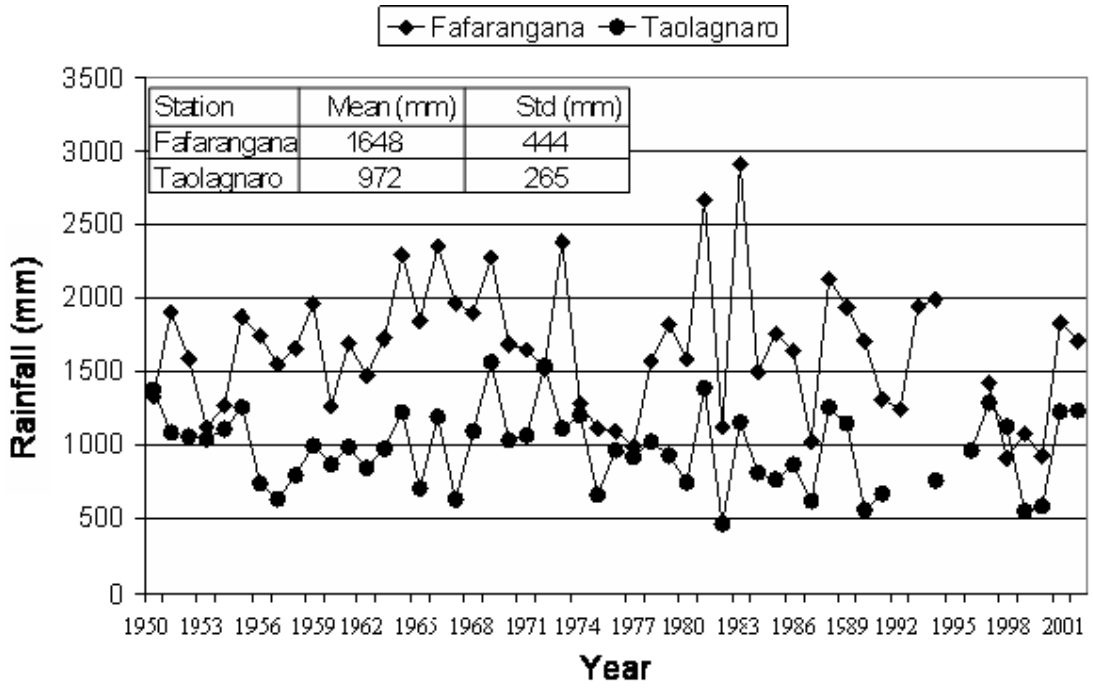

Figure 17: Average summer rainfall season from the southeastern region.

Following the South region, the western part is much dryer than its eastern counterpart as displayed in Fig. 18. The two stations are located around 20°S-22°S latitude so that the

extratropical effects are less than those encountered for other most southern rainfall stations (e.g.: Taolagnaro). Moreover, though Fafarangana is located in the same latitude range it receives most rainfall, e.g. more than twice than in the southwest coast. Orographic effect could explain this since the upward forcing by the eastern highland induces orographic rainfall and consequently constitutes a drying process like the well-known meteorological phenomenon, Foehn effect. The consistency and homogeneity of these two rainfall stations are distinct though the variability of the records from those two stations is high when compared to the remaining ones.

Fig. 19 depicts that the rainfall rate over the highland and the homogeneity in the records between the stations are quite good. This reveals a significant orographic rainfall activity over the whole highland.

Though the variability is low in comparison to the average level, this activity is rather uniform during the year inside the seasonal cycle and influence the rainfall budget of the west coast. Fig. 20 displays the rainfall rate observed at four stations which covers the middle and northwest coast of Madagascar.

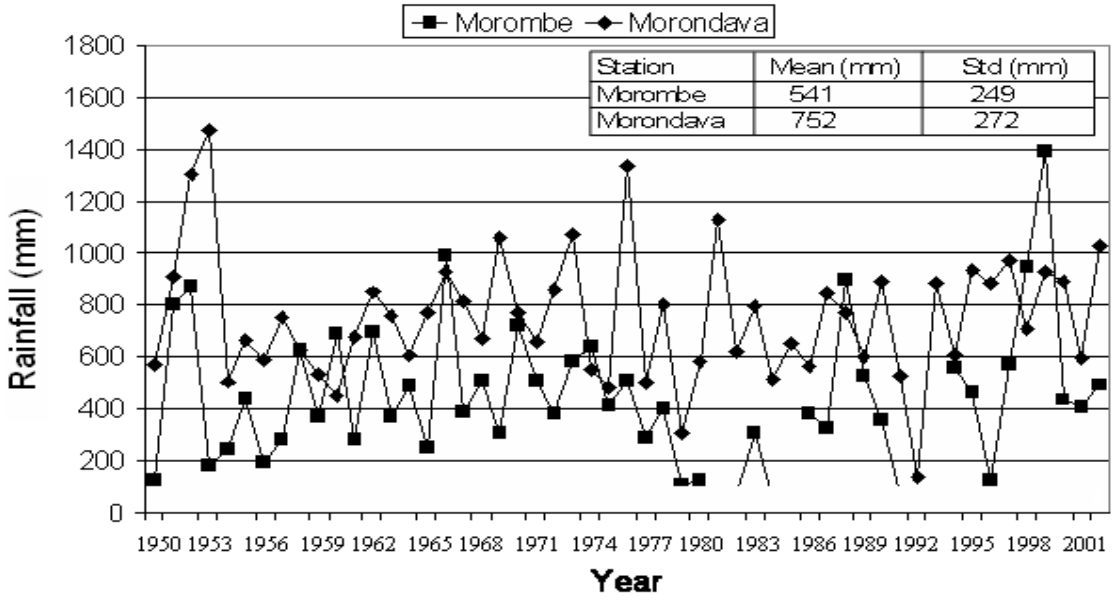

Figure 18: Average summer rainfall season from the south western region.

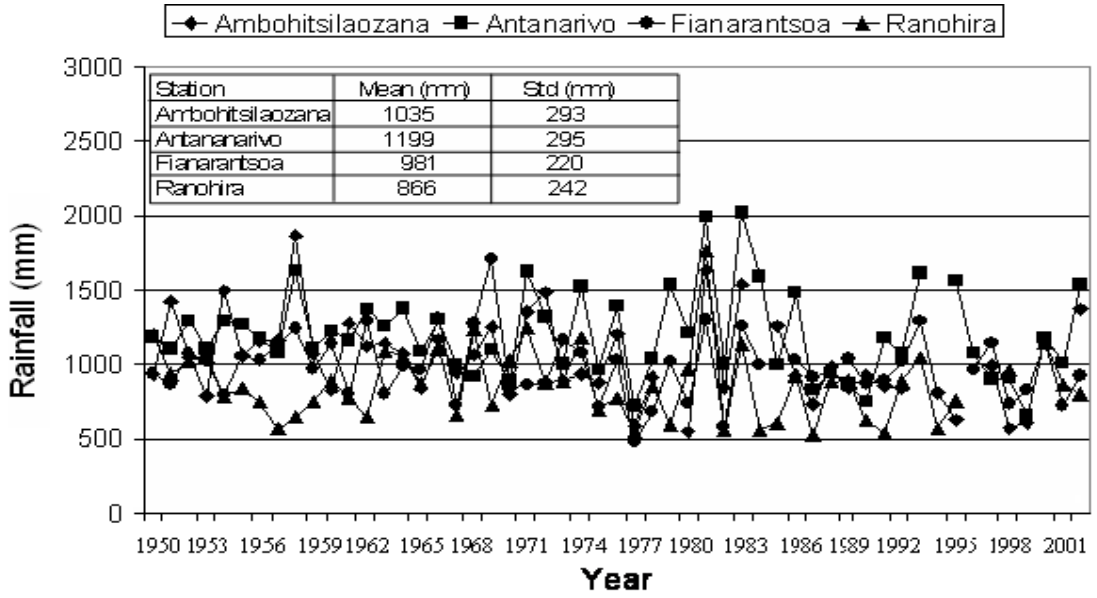

Figure 19: Average summer rainfall season from the highland region.

In fact, this area is under the influence of the monsoon regime prevailing during the austral winter and summer season. The rate is comparable to that observed over the northeastern coast. However, monsoon flow seems to drive the rainfall area in addition to the downstream trade wind which is mostly deflected along the northeast coast.

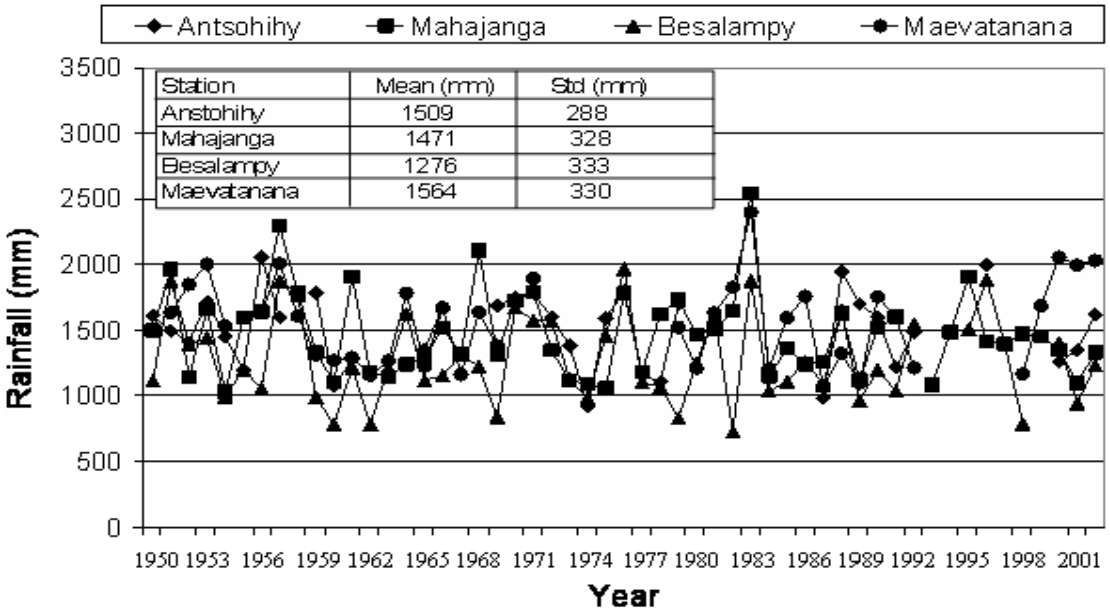

Figure 20: Average summer rainfall season from the northwest coastal region.

Thus, December to March season coincides with the northeast monsoon season when the ITCZ brushes the northwestern region of Madagascar, primarily responsible for the heavy rainfall in this area, southeasterly flow contributes to the rainfall rate activity along the eastern coast adding to the rainfall budget of the area where the orographic effect is significant especially along the middle east coast. The highland is also under the influence of the trade wind and orographic effects which induce significant influence on the rainfall budget in this area. This highland contributes to the drying process for the south and Middle Western region where extratropical perturbation would participate in the budget in the south.

3.2. Monthly analysis of the regionalized rainfall data

The gamma distribution represents these data much more closely, and provides a plausible summary of the month to month variations in the data than the Gaussian distribution. Moreover, the following graphs feature the rainfall density event towards the south and the west which justify the preceding results. The portraits emphasize regional monthly probability during the period 1950-2003 of the observed precipitations classified in different intervals according to their quantities.

Fig. 21 shows the probability density of rainfall distribution over the northeastern coast. Rainfall distribution is well fitted by the gamma distribution and suggests some consistency of the data. The figures evidence the seasonal cycle of the rainfall activity in this area with a significant activity during summer period.

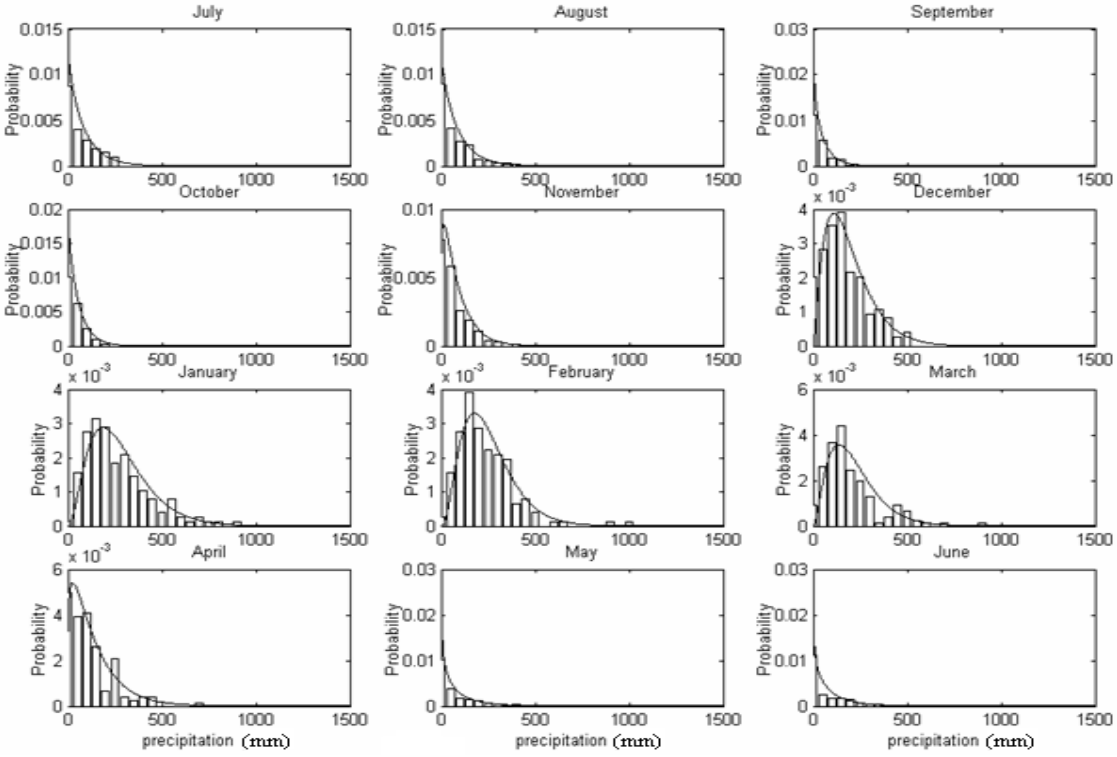

Figure 21: Density of the probability rainfall distribution of the northeastern coast of Madagascar in the period 1950-2002.

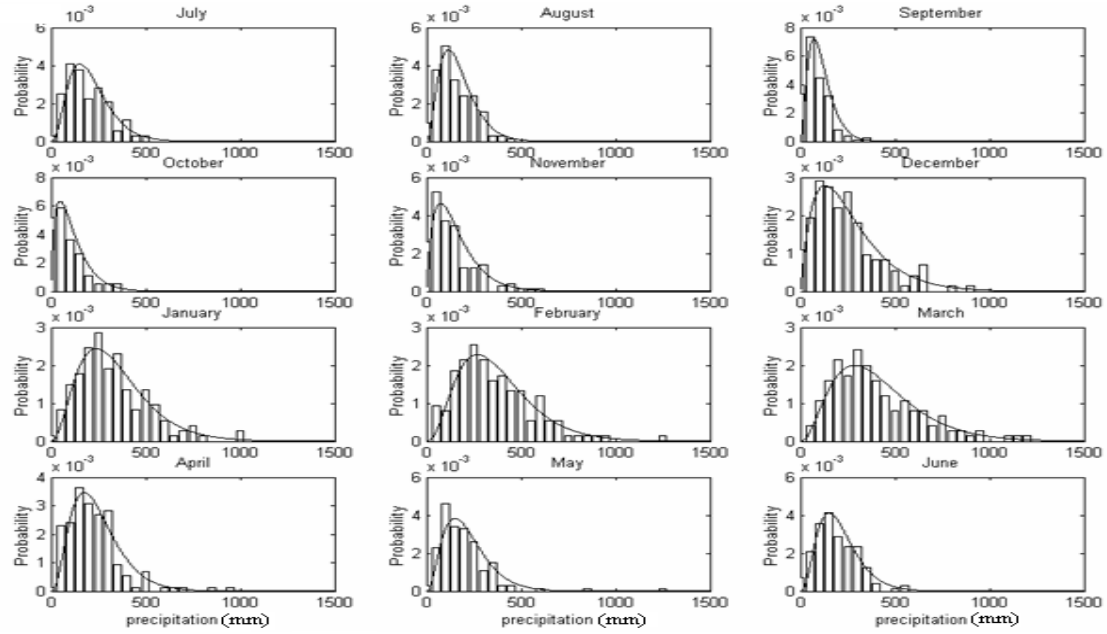

Figure 22: Density of the probability rainfall distribution of the Middle Eastern coast of Madagascar in the period 1950-2002.

Rainfall distribution is still observed during austral winter which confirms as mentioned earlier the influence of equatorial perturbations (monsoon) and trade winds pattern. Middle and southeast coast are subjected to a constant rainfall activity along the year as shown in Figs. 22 and 23 where the rainfall distribution is noticeable from July to June following the southern hemisphere season. Precipitation distribution is consistent to the empirical distribution and the rainfall activity over the middle and southeastern coast of Madagascar. Nevertheless, southern part is subject to more event of small rainfall rate than its counterpart since its rainfall level is less than the Middle Eastern coast.

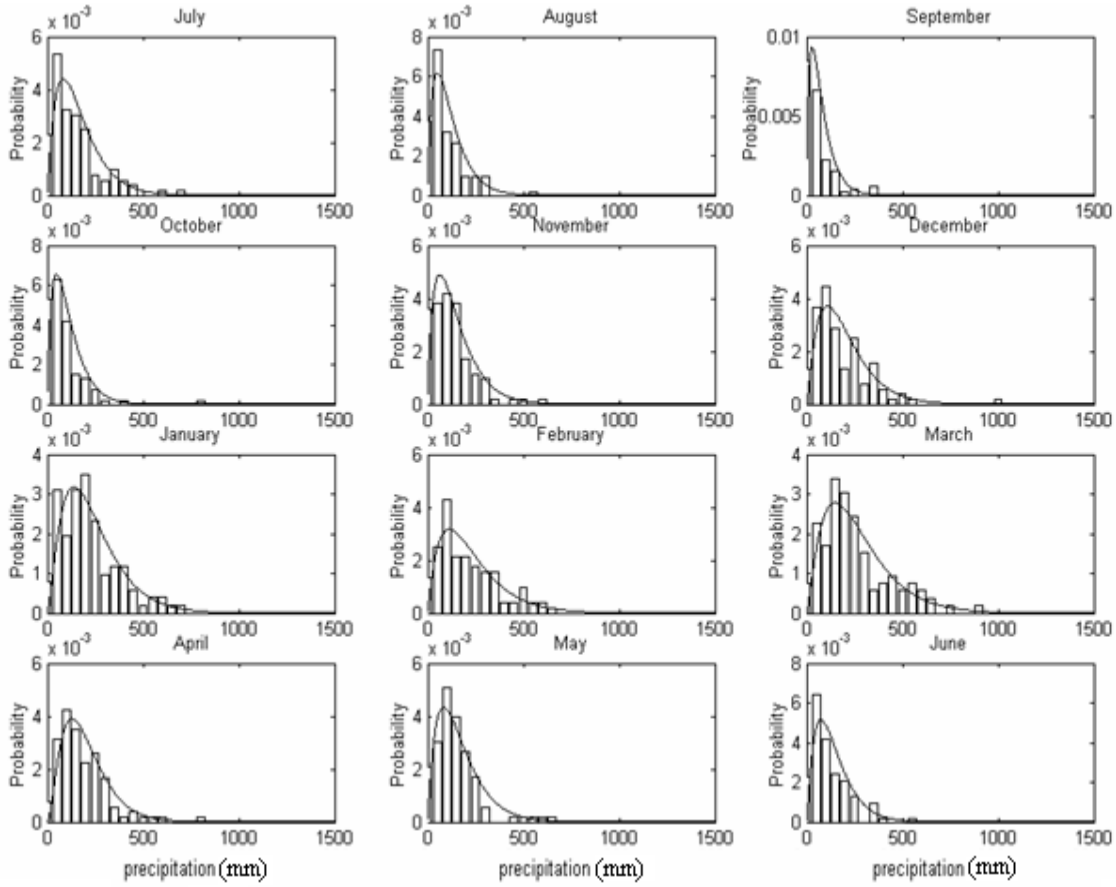

Figure 23: Density of the probability rainfall distribution of the south eastern coast of Madagascar in the period 1950-2002.

In contrast, the highland has a more pronounced seasonal feature with two distinct seasons, one during summer with rainfall activity and another winter season with no activity

as shown in Figs. 24 and 25. Trade winds are strengthened during austral winter but conversely the water content in the air is lower than during the summer. It is assumed that the orographic effects act directly over the eastern coast and all of the water content in the atmosphere is converted into rainfall along the coast. During the austral winter, the ITCZ is in its northernmost geographical location during austral winter and the trade wind inversion is capped in the lower troposphere. It means that the vertical convection is inhibited limiting the conversion of water content with convection.

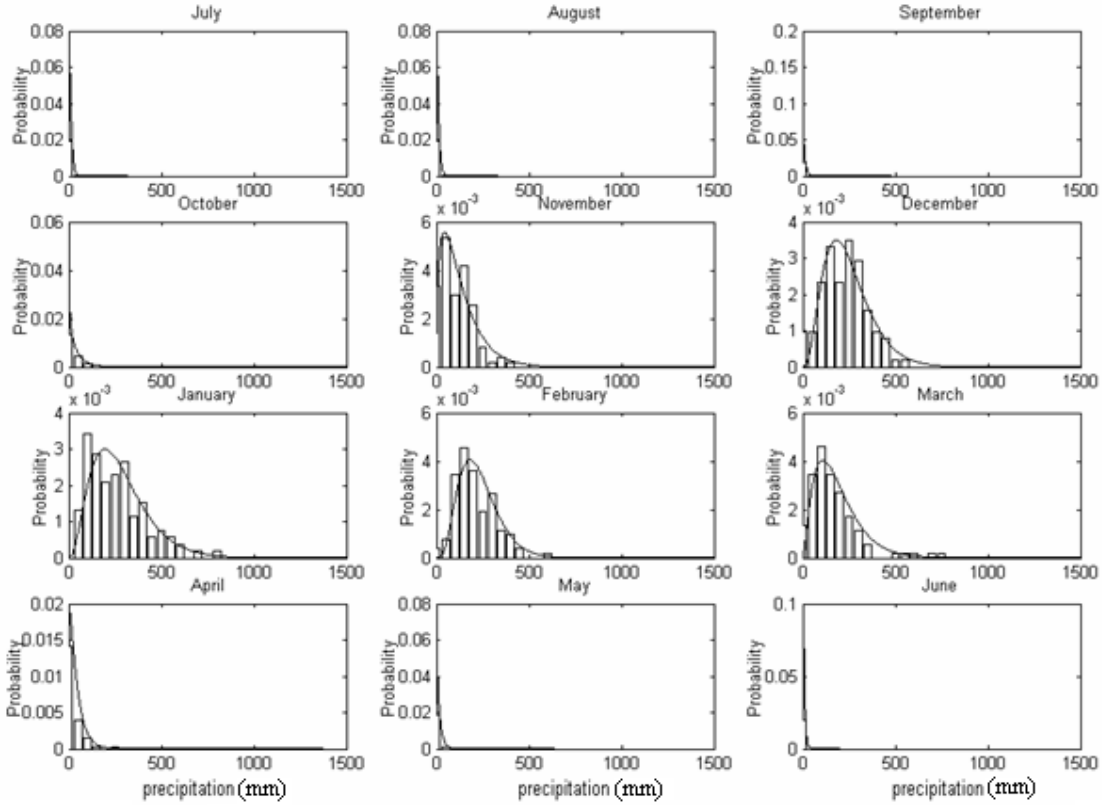

Figure 24: Density of the probability rainfall distribution of the northern highland of Madagascar in the period 1950-2002.

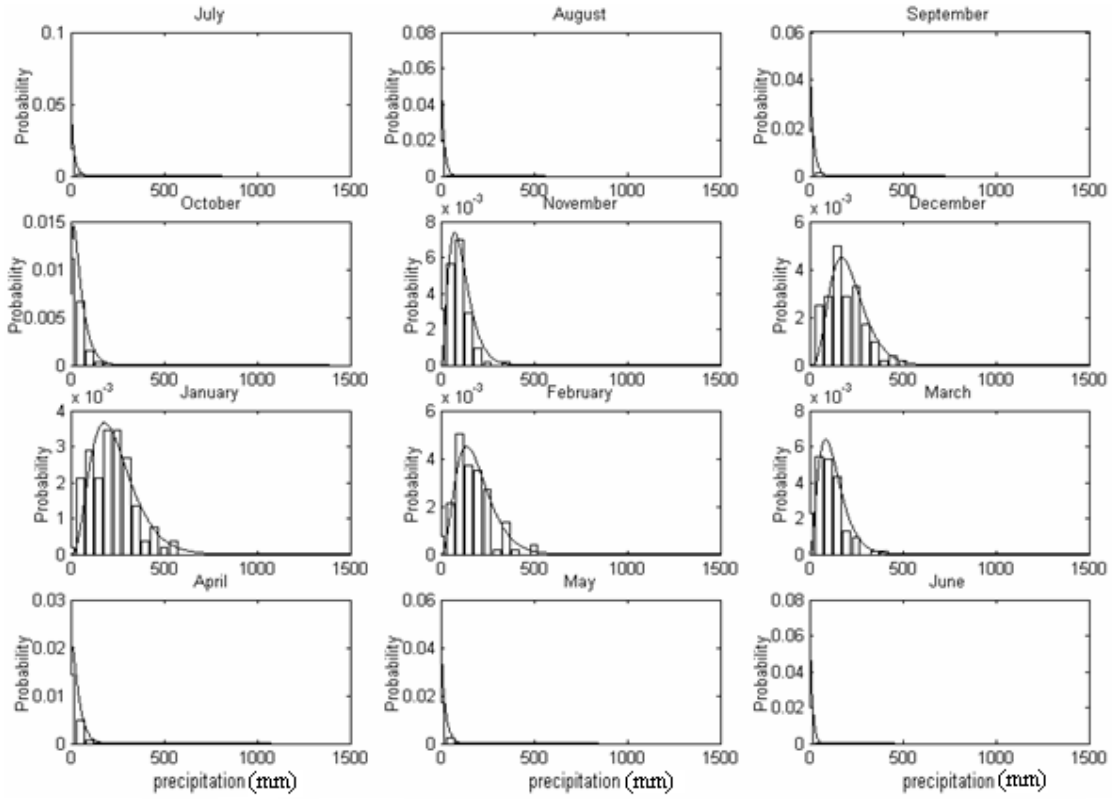

Figure 25: Density of the probability rainfall distribution of the southern highland of Madagascar in the period 1950-2002.

Western coast reveals a distinguishable behavior of rainfall activity during the year. As shown in Fig. 26 water budget is very low for the southwest region of Madagascar. During summer rainfall activity exists over the southwest but remains very low in comparison to other regions of Madagascar. This area is under the extratropical perturbation influence especially during winter season related to the break of the monsoon period.

Technically, Malagasy rainfall is well fitted to the empirical gamma distribution function. Obviously, the connection of rainfall activity over Madagascar is linked to the seasonal cycle of the large scale circulation mixed with the local effect.

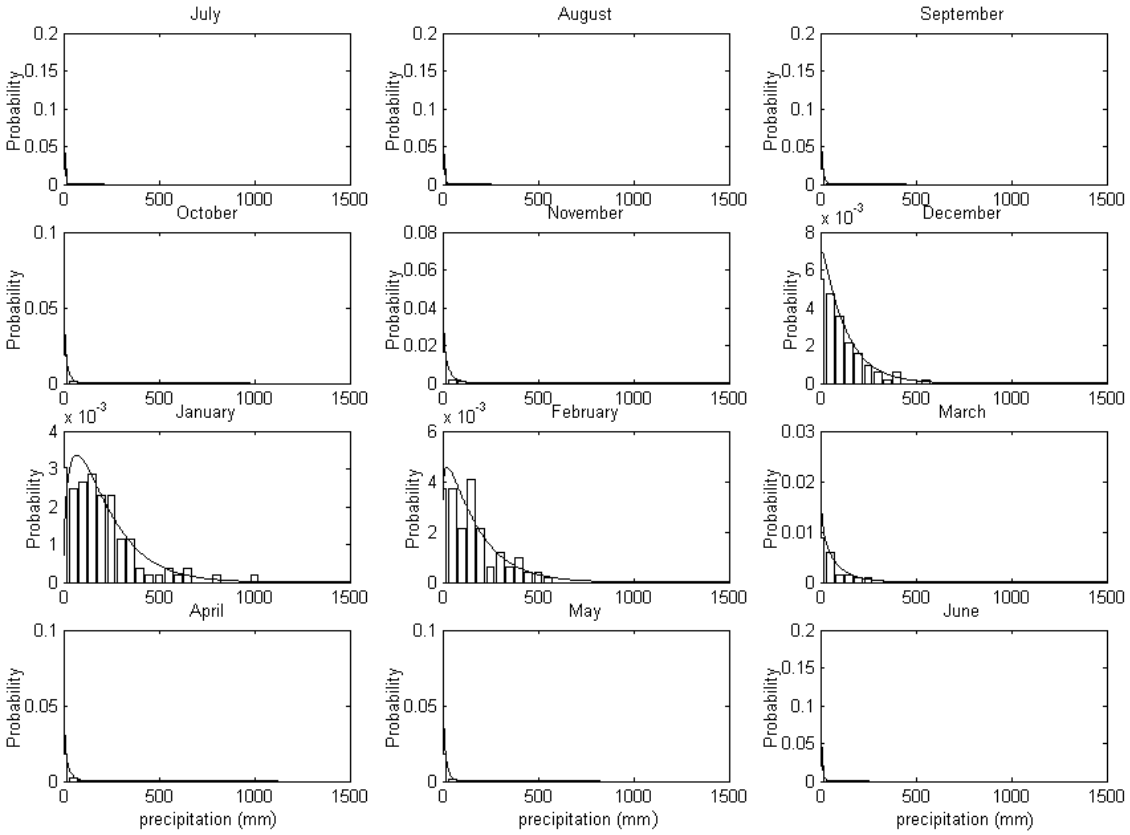

Figure 26: Density of the probability rainfall distribution of the southwestern coast of Madagascar in the period 1950-2002.

3.3. Spatial representation of the Malagasy rainfall over 50 years

The largest meteorological feature associated with Madagascar is the Inter Tropical Convergence Zone (ITCZ). This band is associated with the convergence of northeasterly and southeasterly trade wind, and migrates approximately with the path of the overhead position of the sun. Conditions associated with the ITCZ include consistent precipitation due to uplift from convergence. Therefore, the location of the ITCZ is a determining factor yielding maximum rainfall over the island. One way to understand the seasonal movement of the ITCZ is by showing the monthly mean of the rainfall (Fig.27).

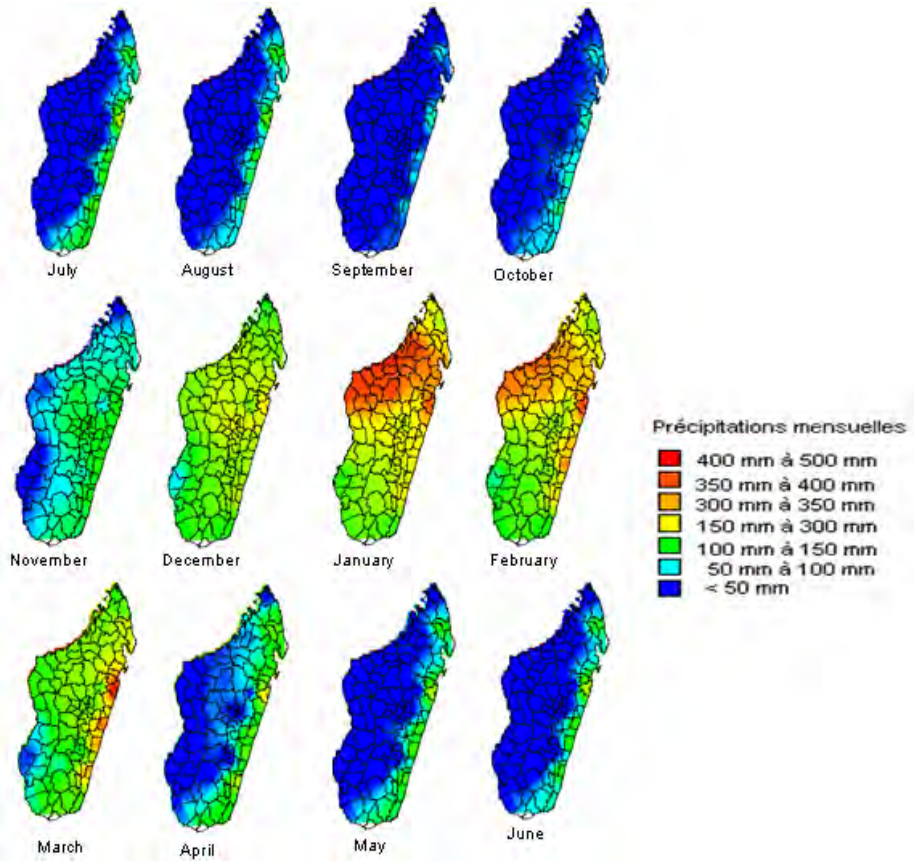

Figure 27: Climatological monthly mean precipitation for the period 1951-2003

The graphs are based on 53 years of data with 96 dpi (dots per inch) resolutions. The condition responsible for the rainfall before the ITCZ return is the moist air brought by the southerly trade winds persisting in the South-East hurting the assembly line along the eastern coast. Consequently, the essential moisture is left in the East and a very little quantity reached the highland.

4. Conclusion

Climatologic study of the monthly precipitation during the period 1950/1951-2003 of Madagascar reveals that its variability in term of precipitation is related to the movement of the ITCZ. Though the time series are long enough for our analysis the inhomogeneity

occasionally pose difficulties. Therefore, the gaps are filled with estimated values using interpolation or extrapolation. And so the final time series compromise between the homogeneity and the availability of the spatial distribution.

It is still proved from this study that Malagasy annual rainfall variability is strongly influenced by the zonal circulation passage such as the ITCZ during the hot season. In winter, this mechanism is followed by the wind elevation from the extra tropical perturbation hitting the mountain chain along the oriental coast that brings a huge quantity of precipitation in this region and makes orography as dominant feature to the rainfall regionalization. However, there are several known circulation models and mechanisms occurring in different atmospheric layer levels which are responsible for this variability.

Part II: Connectivity of Madagascar rainfall modes of variability

Summary

Principal component analysis is a mainstay of a modern data analysis, frequently used by climate and water resource researchers to analyse high dimensional datasets such as rainfall time series. This study aims to dispel what is hidden in this kind of black box poorly understood by making connection with other climate variables such as the tropical cyclone (TC) indices, El-Nino Southern Oscillation (ENSO), Quasi-biennal Oscillation (QBO). Atmospheric variables from the National Centers for Environmental Prediction (NCEP) reanalysis datasets are used to highlight the dynamics of the variables system. Furthermore, from the first principal component, this study clarifies the role of the tropical cyclones in modulating Madagascar rainfall during the austral summer season.

Chapter 1: Principal Component Analysis applied to Madagascar rainfall and its link with climate phenomena over the period 1951-2000

1.1. Introduction

The dominant component extraction technique currently in use is known as principal component analysis (PCA), or the closely related empirical orthogonal function analysis (EOF) (Wilks, 1995). This technique focuses on second-order statistics by reducing the correlation of the extracted components while maximizing the variance (in a least squares sense) of successive principal components. There are many examples in the literature where this technique has been applied to climate datasets, and this has assisted in the identification of a wide range of climate phenomena, such as the Interdecadal Pacific Oscillation (IPO) (Zhang et al, 1997), the Indian Ocean Dipole (IOD) (Saji et al, 1999), and the Artic Oscillation (AO) (Thompson and Wallace, 1998).

On component extraction several techniques have been used in climate studies to compress the dimension of large datasets and contribute in the identification and interpretation of significant 'modes' of climate variability. These types of analysis are usually performed simultaneously, so that large climate datasets can be represented by a small set of 'components' with each component assigned a physical interpretation relating to the present mechanisms such as the dynamics of the underlying system (Zwiers, F.W., & Von Storch, 2004) or simply the phenomenon that governs those datasets.

Despite the establishment of the rainfall climatology over Madagascar gaps are still identified in the previous analysis for instance the spatial and temporal variation of rainfall with tremendous spatial gradient of rainfall in all directions. It is therefore vital to optimally compute space-time modes of variability of the country. This is perhaps the first attempt made for Madagascar despite the popularity of the PCA. Most important, salient factor that determines these modes is investigated in order to understand the rainfall mechanism of the area of study.

Thus, we will start this analysis with the data used followed by the review of the PCA theory and then describe different phenomena susceptible having link with the PCA results. This method will be applied to the rainfall datasets so in due time, the illustrating output will be further discussed. This chapter will end with the mean composite analysis of some atmospheric variables related to the events having the highest and the lowest principal components amplitude.

1.2. Data used

Diagnostic analyses are mainly based on principal component analyses for rainfall and correlation between different climate indices data such as QBO, TC, ENSO, SOI anomalies. Here, the datasets used will be described.

a) Rainfall

Most of the Madagascar's rainfall occurs during the summer season, generally from November to April. Monthly rainfall datasets for the period 1951 to 2000 over the whole key area is used in this study. The gridded rainfall datasets of spatial resolution 0.5^{o} are extracted from the New Monthly Precipitation Climatology for the Global Land Areas which is the result of the research project Variability Analysis of Surface Climate Observations

(VASClimO) (Beck & Rudulf, 2004) within the framework of the DEKLIM (German Climate Research Programme).

b) Data index values

As stated previously, other datasets have been used in the present study, each of them encompassing the austral summer months from 1951 through 2000. The first dataset consists of the usual Tahiti minus Darwin sea-level pressure (SLP) difference used for Southern Oscillation Index (SOI). SOI data with more detailed descriptions can be retrieved from the National Oceanic and Atmospheric Administration (NOAA) Climate Prediction Center (CPC).

The Quasi-Biennial Oscillation (QBO) datasets computed at Physical Sciences Division can be also obtained from the NOAA Climate Prediction Center. QBO index from the National Centers for Environmental Prediction - National Center for Atmospheric Research (NCEP/NCAR) reanalysis data are zonally averaged winds at 30 mb taken from over the equator.

The next datasets are EL-Nino Southern Oscillation (ENSO) which were tracked by using Sea Surface Temperature (SST) measurement captured from satellite data having spatial coverage over the equatorial Pacific Ocean (3^oS - 3^oN, 180^o -140^oW ; 10^oS - 0^o, 90^o - 100^oE). Moreover, ENSO in the equatorial pacific exerts a strong influence on the global climate (Wallace, Rasmusson, Mitchell, Kousky, Sarachik, & Von Storch, 1998); (Trenberth, Branstator, Karoly, Kumar, Lau, & Ropelewski, 1998); (Slingo & Annamalai, 2000), therefore, this combination is merely aimed to exhibit the most significant events and its characteristics.

Among the datasets used is the Tropical Cyclone index collected and archived by the La Reunion Regional Specialized Meteorological Centre (RSMC) restricted in the Western and central portion of the South Indian Ocean (West of 100^{o}E).

c) Atmospheric dynamic variables

We employ different atmospheric reanalysed data to highlight the features of the atmospheric circulations. This dataset consists of a reanalysis of the global observational network of meteorological variables (wind, temperature, geopotential height, humidity on pressure levels, surface variables and flux variable like precipitation rate) reported on a 2.5^{o}x2.5^{o} grid every 6 h (0000, 0600, 1200, 1800 UTC), on 17 pressure levels from 1000 to 10hPa, which are good resolutions for studying synoptic weather systems.

Furthermore, we also make use of Outgoing Longwave Radiation (OLR) derived from satellite. Launching polar orbital National Oceanic and Atmospheric Administration (NOAA) Television Infrared Observation Satellite (TIROS) satellites has made it possible to establish measures of outgoing longwave radiation (OLR) at the top of the atmosphere and at a resolution of 2.5^{o} latitude-longitude (Gruber, A., and A. F. Krueger, 1984). The OLR unit is W/m^{2}. The NCEP reanalysis system assimilates all archived data from 1948 to the present via a numerical model. The details of NCEP reanalysis can be found in (Kalnay et al., 1996) and (Kistler, R., and Coauthors, 2000).

One the most attractive characteristics of the NCEP reanalysis with respect to climate studies is its consistency.

1.3. Methods

In this section, techniques that open up a new understanding to rainfall mechanisms are discussed.

a) Principal Component Analysis

Referring to (Trendafilov & Joliffe, 2006) the central idea of Principal Component Analysis (PCA) or Empirical Orthogonal Function (EOF) is to reduce the dimensionality of a data set consisting of a large number of interrelated variables, while retaining as much as possible of the variation present in the data set. This is achieved by transforming to a new set of variables, the principal components, which are uncorrelated, and which are ordered so that the few retain most of the variation present in the entire original variable.

In fact by looking at a data set f(s,t) as a collection of time series of length n_t, at each of n_s gridpoints, we assume that there are some hidden component signals or time series which are linearly combined into the multivariate measurements. After taking out a suitable mean from a data set f(s,t), usually the space dependent time-mean ('climatology'), the covariance matrix R can be formed with elements given by:

$$r_{ij} = \sum_t f(s_i,t) f(s_j,t) / n_t \qquad (1)$$

where s_i and s_j are the i^{th} and j^{th} gridpoints (stations) in space. R is a real, square symmetric matrix with dimension n_s. The average of all r_{ii} (the main diagonal) is equal to space time variance. The alternative covariance matrix R^a contains the covariance in space between two times t_i and t_j given as:

$$r^a_{ij} = \sum_s f(s,t_i) f(s,t_j) / n_s \qquad (2)$$

where the superscript *a* stands for alternative. R^a is square, symmetric and consists of real numbers. The average of the main diagonal elements of R^a and R are thus the same. The $r^a{}_{ij}$ describes how (dis)similar two maps at times t_i and t_j are. Therefore, reversing the role of time and space means using R^a instead of R. R is normally used for explanatory purposes while R^a is more implicit, or altogether invisible. For better understanding, it is important to see the process EOF both ways.

In general, the observed f(s,t) are not orthogonal, therefore,

$$\sum f(s_i,t)\ \ f(s_j,t)/n_t \tag{3}$$

and

$$\sum f(s,t_i)\ \ f(s,t_j)/n_s \tag{4}$$

are not zero for $i \neq j$. This means, neither R nor R^a are diagonal. Here, some basic linear algebra can be employed to diagonalize these matrices and transform f(s,t) to become a set of uncorrelated or orthogonal predictors. For a square, symmetric and real matrix, like R or R^a, this can be done easily, an important property of such matrices being that all eigenvalues are positive and the eigenvectors are orthogonal. The classical eigenproblem for matrix Q can be defined as

$$Le_m = \lambda_m e_m \tag{5}$$

where e is the eigenvector and λ is the eigenvalue, and for this discussion L is either R or R^a. Here, the index m indicates a set of eigenvalues and vectors. Often it will be convenient to assume that the norm $|e|$ is 1 for each m. In the same way, we can diagonalize R^a by calculating its eigenvectors. Then, the transformed maps (linear combinations of original maps) become orthogonal, and the transformed time series are a basis.

Following, we have:

$$f(s,t) = \sum \alpha_m(t) e_m(s) = \sum e_m{}^a(t)\beta_m(s) \tag{6}$$

where the α's and β's are eigenvectors. When ordered, that is, $\lambda_m = \lambda_m{}^a$ and except for multiplicative constants $\beta_m(s) = e_m(s)$ and $\alpha_m(t) = e_m{}^a(t)$, so (6) alone suffices for EOF. Note also that $\alpha_m(t)$ and e_m(s) cannot both be normed at the same time while satisfying (6) and the only unique parameter is λ_m. Hence, the eigenvalues can be ordered: $\lambda_1 > \lambda_2 > \lambda_{3.....} > \lambda_M > 0$.

Moreover, we have:

$$\sum_{m=1}^{M} \lambda_m = \sum_{i=1}^{n_s} r_{ii} / n_s \overset{\Delta}{=} Space \;\; Time \;\; Variance. \qquad (7)$$

The λ_m are thus a spectrum, descending by construction, and the sum of the eigenvalues equals the space time variance. Likewise, the space time variance can be written as:

$$\sum_{m=1}^{M} \lambda_m = \sum_{k=1}^{M} r^q{}_{kk} / n_t \qquad (8)$$

The eigenvalues for R and R[a] are the same, therefore, in the context of R, one can also write explained variance of mode, *m* (λ_m)[1], as

$$m(\lambda_m) = \sum \alpha^2{}_m(t) / n_t \qquad (9)$$

as long as $|e|$=1.

b) Interpretation of PCA

The interpretation of PCA in physical terms is rarely straightforward. Adding to the difficulties are the vagaries of the procedure and display. The details of the covariance matrix, the exact domains used for the weighting of non-equal grids varies. Even the display convention is confusing because Eq. (6) consists of a time series with physical units multiplying a spatial field of non-dimensional regression coefficients. The latter are the spatial patterns of the EOF but many authors instead have displayed the correlation between the time series and the original data. While this may look better, these are not the EOF's. Nevertheless, in spite of these problems, if there is an outstanding mode (like ENSO in global SST or longer time mean sea-level pressure) any of the techniques mentioned will find them. Problems only arise with the less than principal modes poorly separated from each other in Explained Variance.

[1] Jargon: mode *m* 'explains' λ_m of Space Time Variance or $\lambda_m / \sum \lambda_m * 100.\%$ Explained Variance (EV).

c) Links mode of Malagasy rainfall

In the statistical lexicon, the word correlation is used to describe a linear statistical relationship between two random variables. The phrase 'linear statistical' indicates that the mean of the random variables is linearly dependent upon the component of the other.

However, correlations manifest themselves in several different ways according to the method acquired. For example, in our approach which is dealing with matrix, finding a matrix of *p*-values for testing the hypothesis of no correlation is more accurate. Each p-value is the probability of getting a correlation as large as the observed value by random chance, when the true correlation is zero. If $P(i, j)$ is small, say less than *0.05*, then the correlation $R(i, j)$ is significant at 95% level of confidence.

The *p*-value is computed by transforming the correlation to create a *t* statistic having *n-2* degrees of freedom, where *n* is the number of rows of the input matrix X . The confidence bounds are based on an asymptotic normal distribution of $0.5 * \log((1+R)/(1-R))$ (10), with an approximate variance equal to $1/(n-3)$. These bounds are accurate for large samples when X has a multivariate normal distribution.

Note that $R(i, j)$ is related to the covariance matrix $C = \text{cov}(X)$ (11)

whose $(i, j)'th$ element is $C(i, j)/\sqrt{C(i,i) * C(j, j)}$.

d) Dynamics of atmospheric variables

This analysis will consider two-dimensional wind vector describing the horizontal instantaneous **wind** magnitude and direction for a given level of pressure. Each component of the wind correspond to the zonal (positive if it is eastward) and meridional (positive if it is northward) wind.

OLR is used as a proxy to delineate deep convection. Low OLR value indicates deep convection and thus a low radiative infrared emission from the low temperature of high cloud-top. Typically OLR value less than 180 W/m² over tropical area indicates deep convection (Barr-Kumarakulasinghe, A., & Lwiza, 1998).

The specific humidity q is related to the mixing ratio by

$$q = \frac{r_v}{1 + r_v}, \tag{12}$$

where r_v is the ratio of the mass of a variable atmospheric constituent to the mass of dry air.

Since pressure is the independent vertical coordinate, the total derivative can be expanded as

$$\frac{d}{dt} = \frac{\partial}{\partial t} + u\frac{\partial}{\partial x} + v\frac{\partial}{\partial y} + \omega\frac{\partial}{\partial p} \ . \tag{13}$$

Here

$$\omega \equiv \frac{dp}{dt} \ , \tag{14}$$

which is usually called "**omega**" vertical motion, is the pressure change following the motion, which plays the same role in the isobaric coordinate system as

$$w \equiv \frac{dz}{dt} \tag{15}$$

plays in height coordinates. In the lack of strong vertical acceleration, the gravity force must be approximately balanced by the vertical component of the pressure gradient force. Thus,

$$\frac{dp}{dz} = -\rho g \tag{16}$$

and this condition of *hydrostatic balance* provide an excellent approximation for the vertical dependence of the pressure field in the real atmosphere.

By scale analysis, the advection terms vanish in Eq. (13) and reduce to $\omega = -\rho g w$ for large-scale motions. It can be inferred from that vertical motion in pressure coordinate is minus vertical motion in Cartesian coordinate system (Holton, J. R., 1976).

Essentially, the continuity equation is given by:

$$\frac{\partial u}{\partial x} + \frac{\partial v}{\partial y} + \frac{\partial \omega}{\partial p} = 0 \tag{17}$$

or equivalently,

$$\nabla \bullet V = -\frac{\partial \omega}{\partial p} \tag{18}$$

.

Therefore, if $\begin{cases} \nabla \bullet V < 0 \Rightarrow \omega < 0 \Rightarrow w > 0 \\ \nabla \bullet V > 0 \Rightarrow \omega > 0 \Rightarrow w < 0 \end{cases}$

Streamfunction: If a particular two-dimensional motion is nondivergent, then

$$\frac{\partial u}{\partial x} + \frac{\partial v}{\partial y} = 0 \tag{19}$$

,

thus the velocity field can be represented in terms of a single scalar function commonly referred to as streamfunction. If we let ψ represent the streamfunction, then

$$u = -\frac{\partial \psi}{\partial y} \text{ and } v = \frac{\partial \psi}{\partial x} \tag{20}$$

.

Velocity Potential: If a particular fluid motion is irrotational, meaning that

$$\nabla \times \vec{V} = 0 \text{ ,} \tag{21}$$

it is then possible to represent the field flow in terms of a single scalar function ϕ as

$\vec{V} = -\nabla\phi$ or, componentwise,

$$u = -\frac{\partial\phi}{\partial x}, \quad v = -\frac{\partial\phi}{\partial y}, \text{ and } \quad w = -\frac{\partial\phi}{\partial z}. \tag{22}$$

The quantity ϕ, referred to as the **velocity potential**, is a function of (*x*, *y*, *z*, *t*) in the most general case. Unlike the streamfunction, which is applicable for nondivergent, two-dimensional flow, the velocity potential may exist even for three-dimensional flow (Baum, 1997).

1.4. Results and discussions

1.4.1. Madagascar rainfall modes

a) Characteristic spatial and time patterns

Analysis of monthly rainfall data during the climatological period 1951-2000 has shown explicit and significant spatial and temporal patterns. Moreover, the first three first modes will suffice to diagnose the rainfall pattern over Madagascar.

The season chosen is NDJFMA (From November to April) which the austral summer, when the variance is in its seasonal peak, and the Explained Variance for the first mode (Fig.28) is 48.9%. The structure in the first dimension, which we can call the EOF1, and which we can think of being the structure in the spatial dimension have a positive amount and suggests a tendency to monsoon activation.

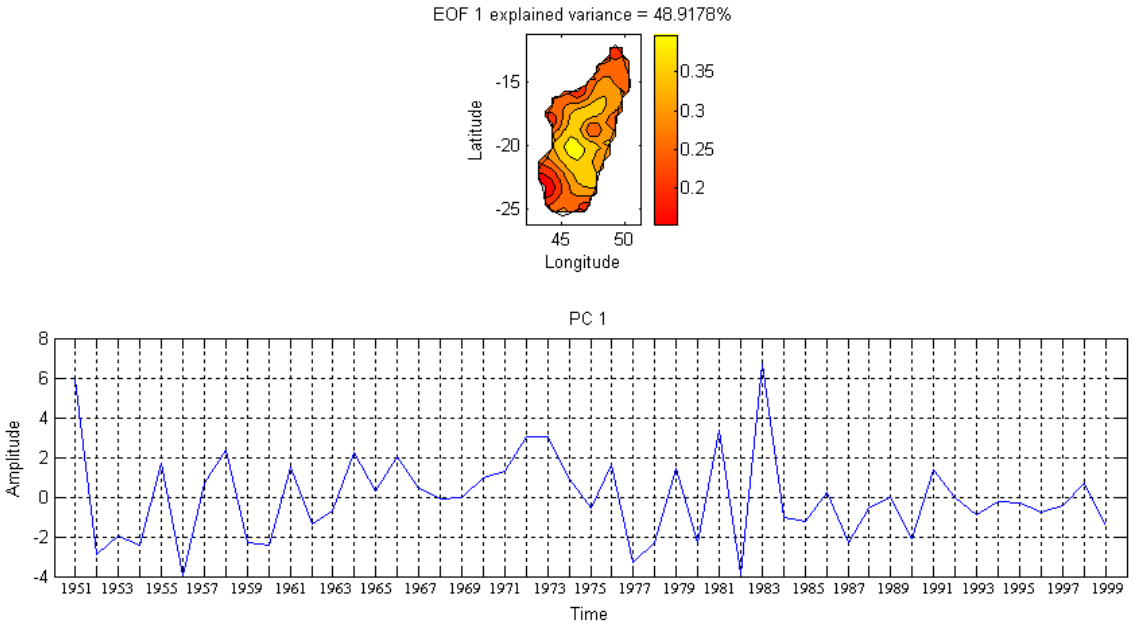

Figure 28: The spatial and temporal pattern of the first mode.

In fact, Madagascar rainy season starting from November up to April having its continental environment is surrounded by a couple of high pressure centre. St Helena anticyclonic circulation is prevailing in the South Atlantic yielding a strong permanent subsidence along the western shores and the southwestern Indian Ocean anticyclonic circulation which is stronger during the austral summer but becomes stable in winter. Hence, two features are usually distinguished according to the main features of the atmospheric circulation: early summer season with more influence from the extra-tropical atmospheric circulation and late summer season when the circulation is more tropical in nature (D'Abreton and Lindesay, 1993).

The complementary set of structure in time sampling dimension we can call the first Principal Component (PC1) represents positive and negative amplitudes unevenly distributed. The amplitudes from 1964 to 1974 tend to be successively positives. However, no significant trend could be discerned in the data but anyhow, the times series versus amplitude below

indicates all famous wet and dry events years (1951, 1956, 1982, and 1983) as large excursions.

Generally, PC's are related one-to-one to the EOF's. Both sets of structures are orthogonal in their own dimension.

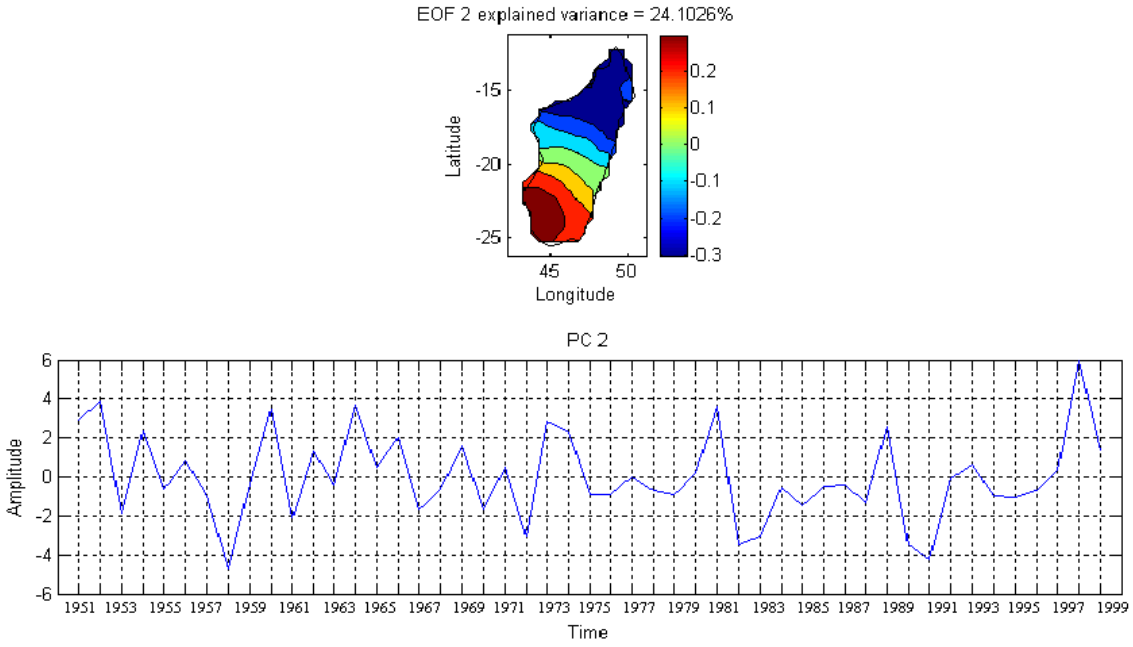

Figure 29: The spatial and temporal pattern of the second mode.

The second mode (Fig. 29) indicates a pattern of North-South polarity explaining 24.1% of the variance. The above figure exhibits that the maximum intensity zone of precipitation is moving in a meridional sense as the trade winds-monsoon convergence. Abundant and frequent stormy rainfall is behind the intertropical convergence i.e incorporated in the monsoon flow. However, moderate precipitation is associated with the trade winds. Statistical decrease of the rainfall during the hot season along the West coast from the North toward the South does not have to be attributed to the demeaning of the equatorial monsoon to the South but mostly due to the fact that this monsoon reaches less rarely this region. According to Riehl (1954), the diminution observed from North to South Madagascar is a problem of frequency rather than of intensity.

The second mode appears to be a signature of the meridional circulation, which is the ITCZ. This mode had its strongest negative and positive projection, respectively, in 1958 and 1998. It is proved here that 1958 was pronounced to be an extreme dry event for some region of Madagascar. Besides, 1998 was observed to be cold event according to the global SST analysis. Note that cold event is not just the opposite of warm event or extraneous to the warm ENSO. Webster et al. (1999) investigated to what extent the climate in the Indian Ocean was a response to El-Nino during 1997-1998, and concluded that the anomalous conditions were primarily the result of a previously undescribed Indian Ocean dipole mode. Somehow, McPhaden (1999) remarked that El Nino event in 1997/1998 has ever been recorded.

The third mode (Fig. 30) is still showing inter annual variability as the annual rainfall manifests in itself. Positive and negative amplitudes were evenly distributed over the last 50 years. Moreover the summer in 1957 is identified as extreme dry event reaching amplitude less than -5 shown in PC3 plot. At this point, the mode explains only 9.5%. However, the corresponding pattern which is orthogonal to the previous mode is very effective to tell us the evidence of East-West polarity that needs more investigation as it is schematically presented in the EOF3.

In fact, monsoon flow reaching Madagascar emphasized by the second mode is actually characterized by strong instability due to different causes such as basic heating and humidification from the Indian seashore associated with the latitude effect of North-South flow (Doncques, 1975).

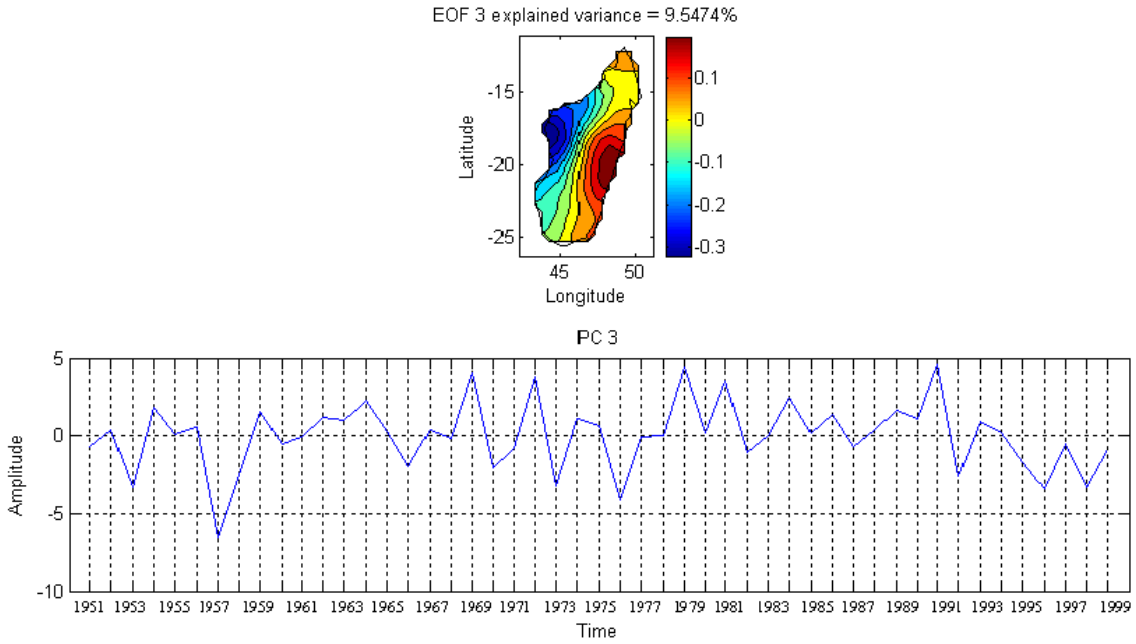

Figure 30: The spatial and temporal pattern of the third mode.

The monsoon instability attaining the big island is also due to the vertical component influence of the Coriolis force which is maximal in the equator. Johnson and Mörth (1960) noticed significant contrast between easterlies and westerlies of the eastern Africa. Furthermore, the zonal flow sense of displacement plays a fundamental role meaning that West-East corresponds to ascendants motions.

Moreover, in westerlies (which is the case of Madagascar monsoon's flow), the humidity tends to be expanded over the air mass thickness so that local or general effects such as thermo-convective instability, horizontal convergence, orography,…are much faster and intense than in the East current flow sector.

However, further investigation is needed to uncover if other physical factors are involved in these principal modes of monthly rainfall variability over Madagascar.

b) Indices and correlations

The equatorial quasi-biennial oscillation (QBO), a quasi-periodic (varying between periods of 24 to 36 months) descent of alternating easterly and westerly zonal winds is a well known phenomenon (Reed et al., 1961). QBO which was originally thought to be associated with the African rainfall time series which has been shown to be coherent with ENSO ((Ropelewski and Halpert, 1987); (Ogallo et al., 1988); (Nicholson, and Kim, 1997)) traces. Hence, its 'influence' on Madagascar summer rainfall over the last 50 years using the first EOF's as a filter is evidently assessed.

Fig. 31 shows the variances of QBO indices plotted with the first PC rainfall. It is mostly observed that the two variables do not increase or decrease together which is fundamentally proved by their cross correlation value -0.33. Note that this negative correlation is significantly above the 99% level of significance.

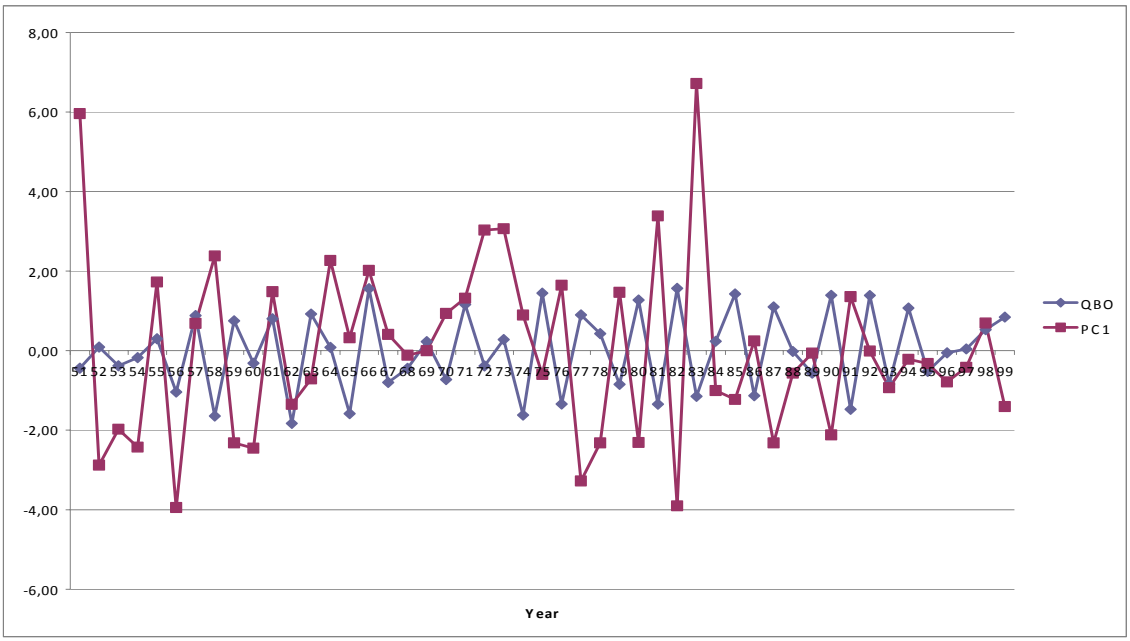

Figure 31: The time evolution of the first principal component plotted with the QBO index.

This result would be explained by considering the Atlantic hurricane frequency by Gray et al. (1992) happening in boreal hemisphere. Similarly, it can be interpreted that in the austral hemisphere precisely during the summer season, years of westward QBO phases in the

uppermost troposphere typically have more named storms, hurricane and more intense hurricanes than years of eastward QBO phase.

The proposed mechanism is that cyclogenesis is suppressed by high vertical shear du/dz at tropical tropopause around 10N. Shear over Atlantic during hurricane season is larger when QBO is in eastward phase. In other words, QBO in westward phase is one favorable condition to cyclogenesis that prevails during the wet season because General Climate Model experiments with assimilated QBO and prescribed SST concluded in 'the role of the stratosphere in tropospheric climate' (Giorgetta, 2003) that QBO can modify the tropical deep convection apart from its direct link to the troposphere. It means that QBO has an influence on the tropical cyclone enhancing eventually heavy rainfall.

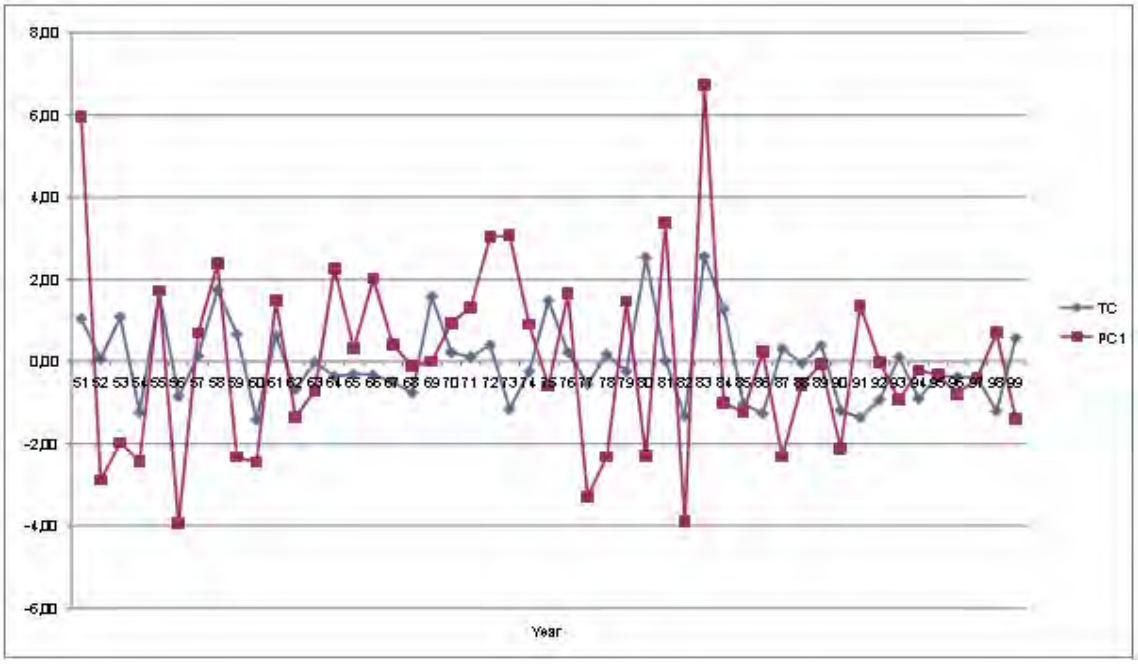

Figure 32: The time evolution of the first component plotted with the TC index.

Therefore, based on the correlation between the first mode of the PC1 rainfall and the Tropical Cyclone indices (Fig. 32), positive correlation coefficient r=0.30 of high statistical significance level 95% is obtained. From this experiment, we can still affirm that TC is among

the main factors influencing Madagascar rainfall. This relationship would be further analyzed in the second chapter of this part of study.

Objective study of the relationship between the second temporal rainfall pattern mode and the Southern Oscillation phenomena was also conducted in order to depict the coherency through time explaining the physical link attributed to the rainfall in the key area.

The evolution of the teleconnection between rainfall PC2 and ENSO is evaluated since there is no significant correlation with other PCs. Therefore, the period 1951-2000 is characterized by negative correlation which is significant at 99% level. The relationship between the two datasets can be revealed by identifying individually the highest variations in the pattern (Fig. 33).

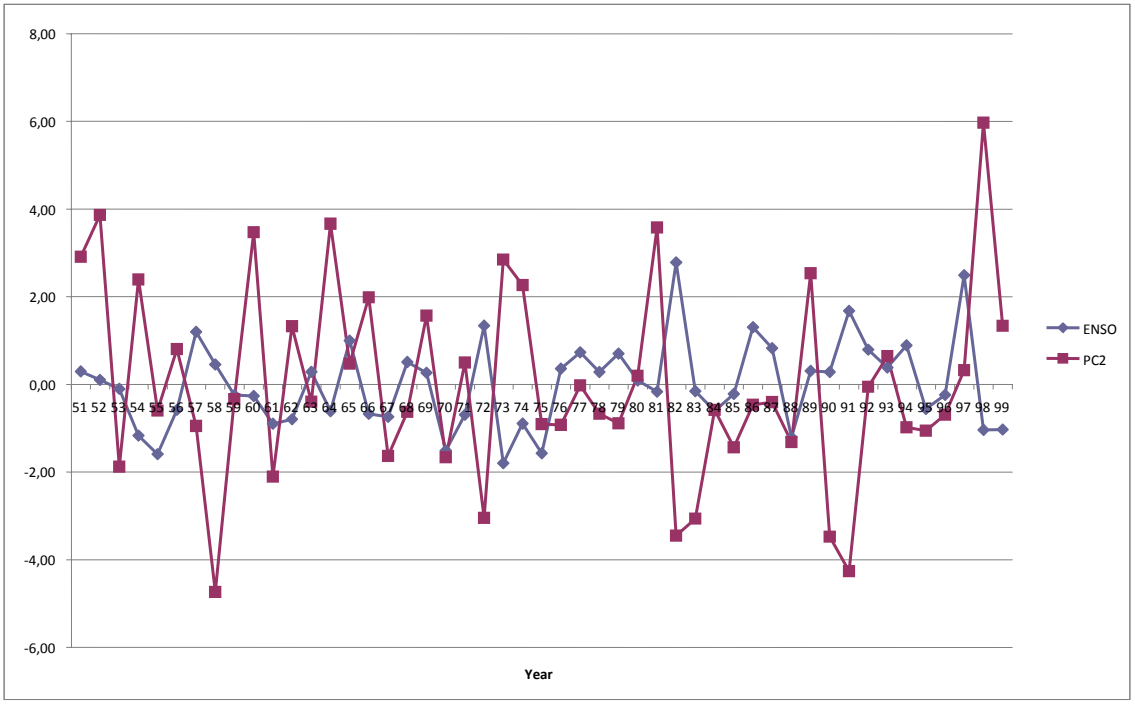

Figure 33: The time evolution of the second component plotted with the ENSO index.

Hence, the Pacific warm event in terms of ENSO in 1998 has a great impact on the rainfall almost over the island associated to the wet conditions (Webster et al., 1999). Similar to 1958, year 1991 is also known as dry period; in fact we can deduce from Fig. 33 that

positive ENSO anomaly is strengthening this severe drought. One considered that the lack of rainfall response to some El Nino Southern Oscillation events (1986, 1987, and 1997) could be explained with an Indian / Pacific disconnection. The disconnection could be at least partly associated with the east phase of the quasi biennial oscillation. The correlation between SOI and summer rainfall is at its maximum when the QBO is in its west phase (Mason S.J., Lindesay J.A., 1993) following the hypothesis suggested by (Gray, W. M., J. D. Sheaffer, and J. A. Knaff, 1992).

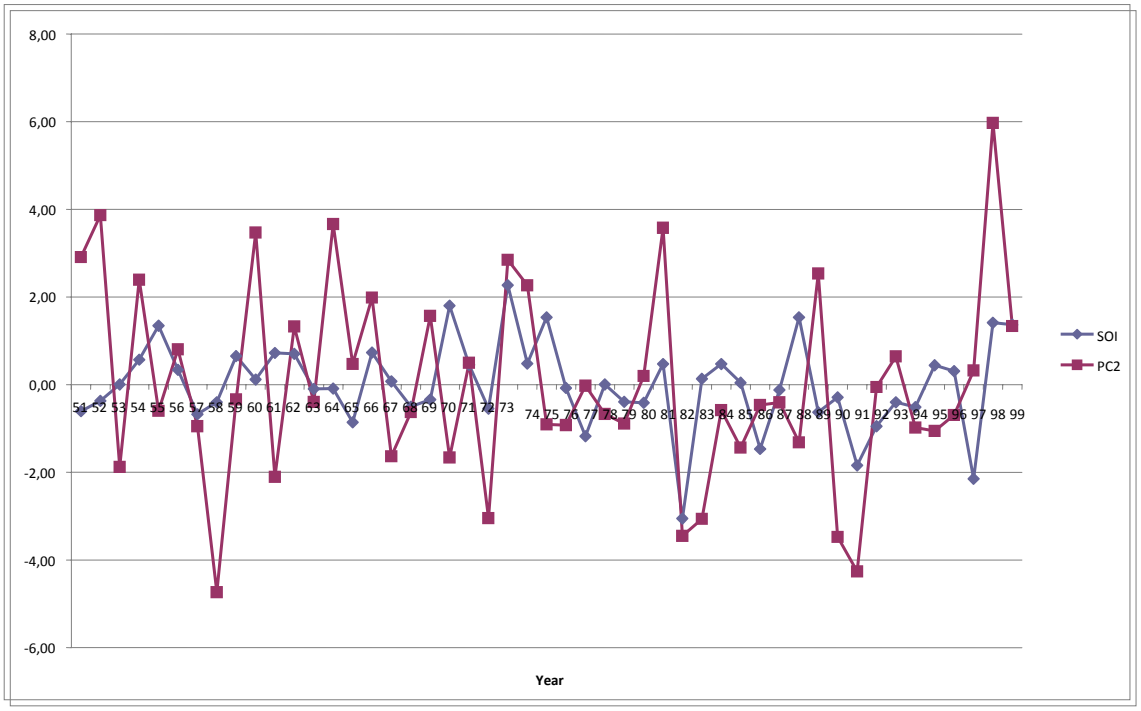

Figure 34: The time evolution of the first component plotted with the SOI index

Hence, further investigation is conducted to the Malagasy rainfall responding to the SOI. During 1951-2000, the correlation between November-April SOI and rainfall PC2 is significant at the 95% level (r= -0.3) (Fig. 34). This demonstrates the statistical links between SOI and Malagasy rainfall. However, the relationship is weak and the SOI explains less than 10% of inter annual rainfall variability. Despite the weak robustness of the link, it also reveals that SOI is relatively the opposite phase of ENSO that could be interpreted as high variability

of SOI which is supported by the 'ENSO decay' or inversely. The difference Darwin minus Tahiti sea-level pressure describes meaningful feature although it has not impacted on the whole summer season over Madagascar. Moreover, the ENSO is more tropical phenomenon and its impact concerns mainly late summer rainfall (Lindesay, 1988).

Unfortunately, the third temporal pattern does not have significant relationship with any physical parameters stated above. Based on the spatial pattern, we can figure out that local effect such as the orography influence is supposed to be the most appropriate explanation given to the third mode of Madagascar rainfall pattern.

1.5.1. Atmospheric circulations for Malagasy rainfall modes

Highly positive amplitude does not always display the wettest event nor the highly negative amplitude either existence of extreme event. This observation demands more explanation.

Composite analysis of the dynamic atmospheric variables is suggested in order to comprehend the fundamental dynamical process of mode of rainfall variability based on the extreme amplitudes of PCs. The following years are selected to form atmospheric composite for PC's.

Table 2: List of the PCs composite years

PC1		PC2		PC3	
1951	1977	1952	1958	1964	1957
1958	1978	1960	1972	1969	1973
1972	1980	1964	1982	1972	1976
1973	1982	1973	1983	1979	1992
1981	1987	1981	1990	1981	1996
1983	1990	1998	1991	1991	1998
Wet	Dry	Wet	Dry	Wet	Dry

The composite analysis applied in the following study is based on the difference between the highest PCs amplitude or 'wet events' minus the lowest amplitude or 'dry events'. The composite years corresponding to these events are lined up in the Table 2.

a) Leading mode extreme dynamics

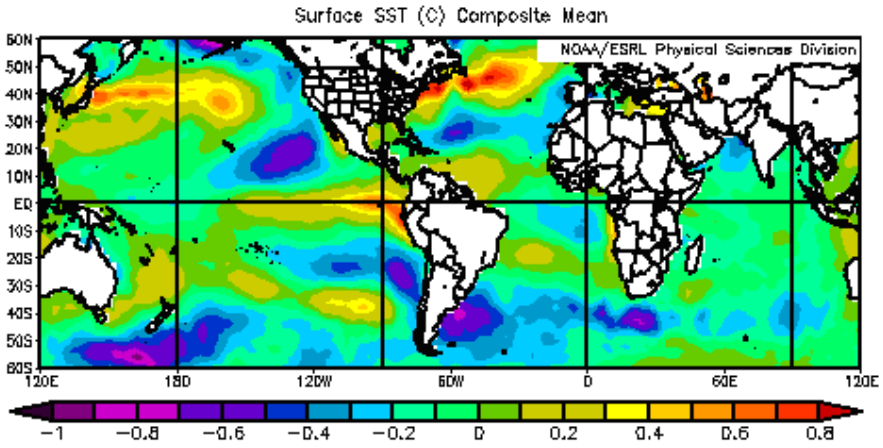

Figure 35: Global tropical SST composite pattern (^{o}C) of the first mode.

The composite SST pattern of the leading mode exhibits anomaly values $\sim \pm 0.2^{o}$C in the Indian Ocean. In the Atlantic Ocean and Pacific Ocean, the SST patterns assume N-S contrasts and the anomaly values are within $\sim \pm 0.9^{o}$C (Fig. 35). Weak El-Nino signal is noticeable in some regions of the equatorial pacific except near to the Peru coast having a warm SST anomaly. The Atlantic SST shows a latitudinal variation with southern regions having a cold pool while the reveal of warm water over the Indian Ocean and the temperature uniform within normal amplitude. Alternating signs of SST in concave fashion is displayed from SE to NW. Moreover, it was investigated from the study on the 'tropical monsoons around Africa: Stability of ENSO associations and links with continental climate' by Jury et al. (2002) that the nature of the ocean-atmosphere coupling is assessed with a focus on the circulation over equatorial Atlantic and air-sea interactions of the Indian Ocean. Varying contributions are evaluated for the surface heat fluxes, radiative transfer balance and wind-forced ocean uplift in the development of warm and cold events.

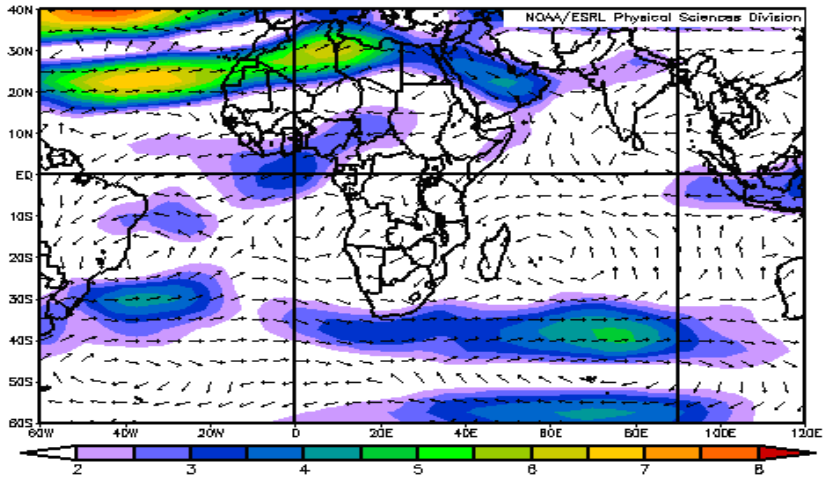

Figure 36: Regional composite wind circulation at 200mb related to the first mode.

Enhanced anti-cyclonic wind circulation is detected over Madagascar at 200mb from the Indian Ocean (Fig. 36). In counterpart, cyclonic circulation is developed in the lower level with warm SST; they drive a strong convection that leads to a potential rainfall activity. This is because an adequate source of energy and vertical wind shear are among the necessary environmental factors evolving convective instability which are important to form a tropical cyclone. Moreover, the pattern explaining the hypothesis how convective activity is taking place regarding the wind flow mechanism at both levels is given by Fig. 37. Low-level convergent and upper-level divergent flows produce strong ascent following the continuity equation

$$\frac{\partial(\rho u)}{\partial x}+\frac{\partial(\rho v)}{\partial y}=-\frac{\partial(\rho \omega)}{\partial p}. \qquad (24)$$

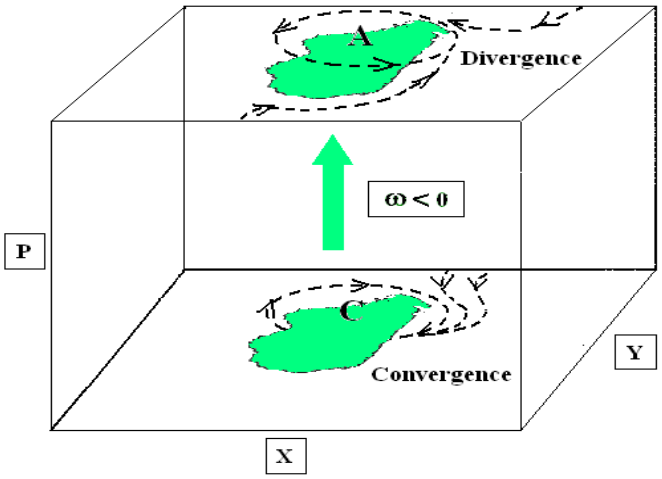

Figure 37: Tropical and extra-tropical flows are co-operating to generate low-level convergent and upper-level divergent flows to produce strong ascent with respect to the continuity equation.

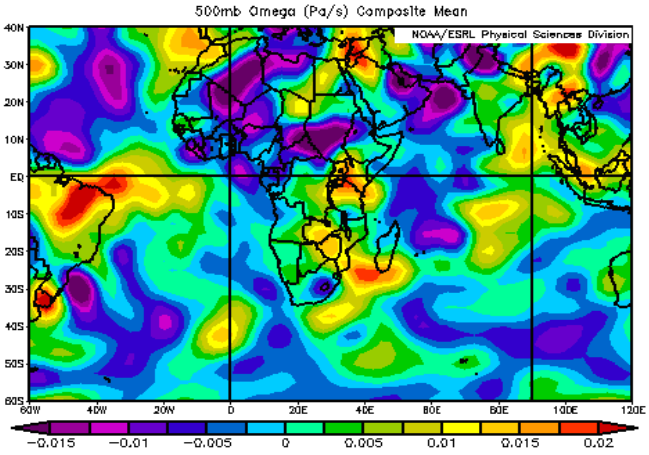

Figure 38: Regional composite omega pattern in the mid troposphere (500 hPa).

With respect to the anomaly width and length (>10^{o}) displayed in different composite patterns (the geographical locations of the anomalies are found in the appendix), teleconnection is detected from PC1 and the upper-level zonal wind in the North Atlantic Ocean because the two variables are negatively correlated at 95% of significance level.

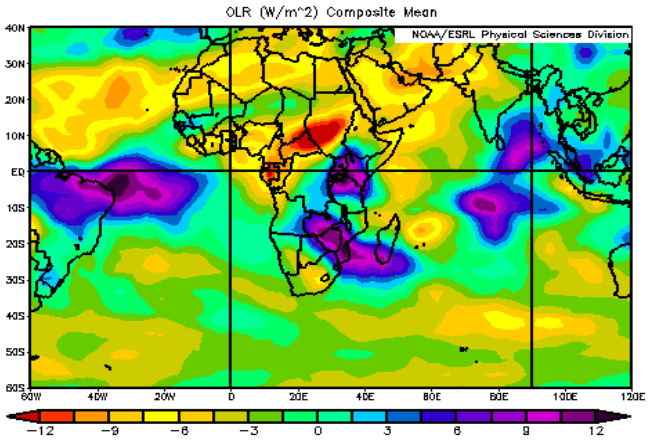

Figure 39: Regional Composite OLR pattern related to the first mode illustrating convective activity for negative values.

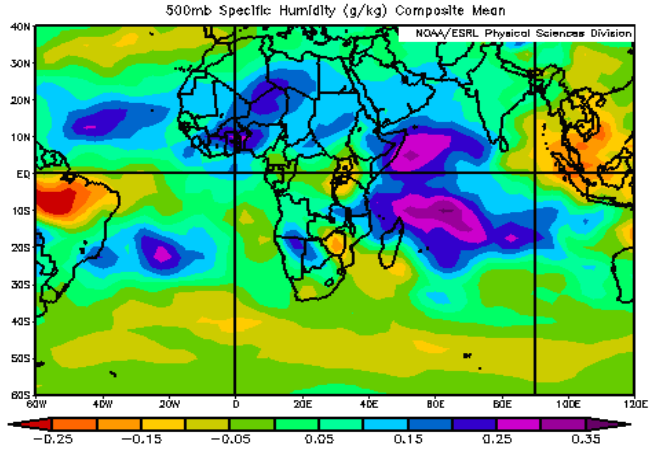

Figure 40: Regional composite specific humidity pattern in the mid (500 hPa) level linked to the leading mode.

An exclusive response to these simulated results is that Omega at 500mb (Fig. 38) highly correlated with the negative OLR anomaly in the north (Fig. 39) with r^2=0.85. Moreover, OLR pattern is also associated with convective activity condition driving moisture penetration from the North though in decrease while moving toward the South likely generating few amount of rainfall in that area (Fig. 40).

After running the Pearson's correlation to extracted time series of all key area variables, it is found that mid-level omega anomaly located at (30-42^{o}E, 38-28^{o}N) above the African Continent (Fig. 38) and PC1 (Fig. 28a) are positively correlated (r^2=0.416) (see the Appendix- 2)) which is significant at 99% significance level.

Similarly, the upper-level velocity potential composite mainly displays Pacific Ocean-Indian Ocean dipole generating weak dipoles detected in the Atlantic Ocean. The convective part affects massively southern America, southern Africa and Madagascar (Fig. 41) in irrotational fluid motion.

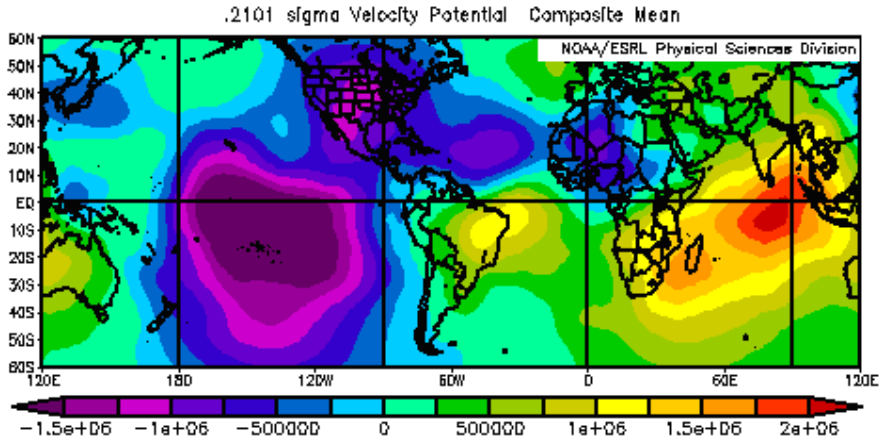

Figure 41: Leading mode composite upper velocity potential pattern significantly defining contrast between the Indian Ocean and the Pacific Ocean.

Thus, these underlying physical mechanisms could generally reveal the rainfall anomalies based on the first component analysis during the summer season.

b) Second extreme mode dynamics

Adopting the same process, composite analysis based on PC2 reinforces that there is strong contrast between north and south. A great number of studies can be made by analyzing the underlying physical patterns issued from the composite results. Unlike the Fig. 35, N-S contrast of SST magnitude ranging between $\pm 0.5^{o}C$ in the Indian Ocean is exhibited from Fig. 42. Less warmer than observed in the leading mode composite, a cool SST anomaly still works together with the anticyclonic flow circulation in the upper level (Fig. 43). It is like a combination of convective process which is driven by the

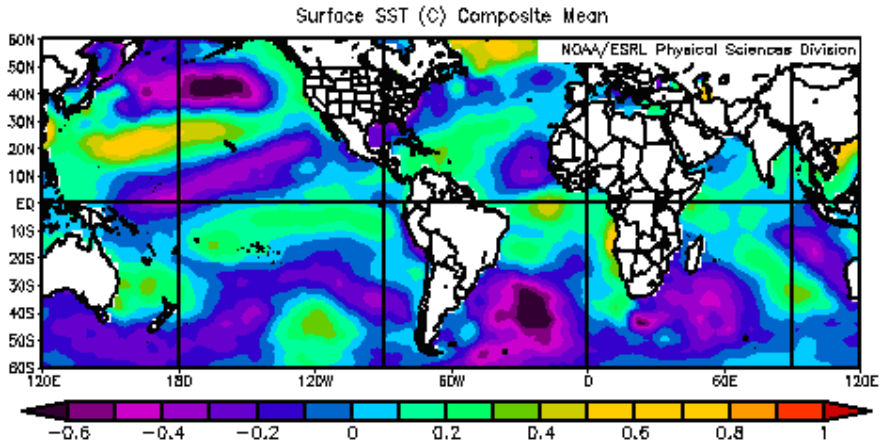

Figure 42: Global tropical SST composite pattern (^{o}C) of the second mode.

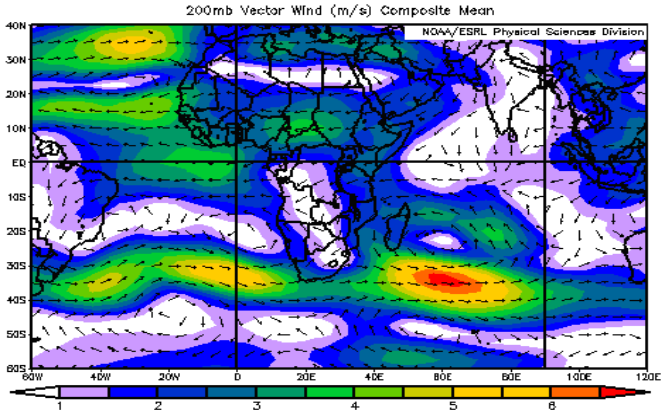

Figure 43: Regional composite wind circulation in the upper level.

lower atmospheric condition and also by the upper level condition. Favorable condition in the lower level can be obtained without convection in the upper level because of the strong wind shear for instance. Moisture is generated mostly in the north at mid-level according to the composite specific humidity showing a wave like pattern (Fig. 44). Moreover, African meridional wind and PC2 of Madagascar rainfall are linearly associated reaching 99% level of significance. Similarly, negative omega anomaly spreading largely from the northern Madagascar located in the western Indian Ocean is negatively related with PC2 but the Northern Atlantic omega anomaly which is positive is appropriately yielding positive correlation with the second rainfall main pattern of the Island.

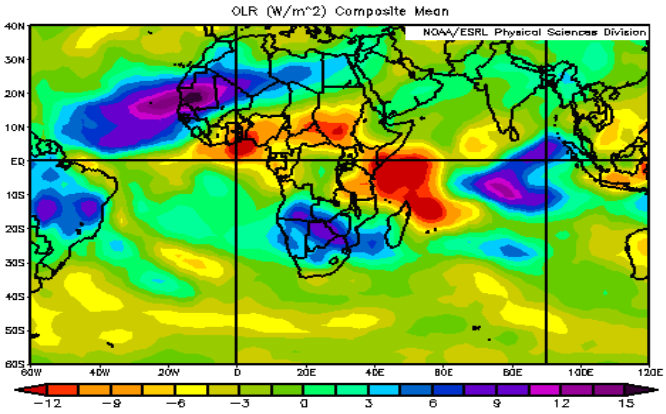

Figure 44: Regional composite OLR pattern.

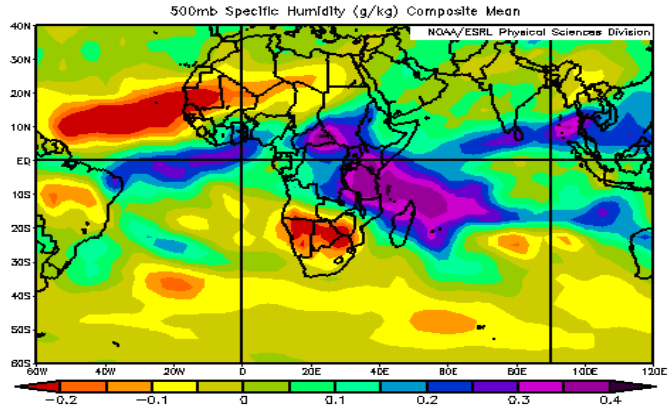

Figure 45: Regional composite specific humidity pattern in the mid (500 hPa) level.

Especially concerning Madagascar, negative OLR anomaly enhancing deep convection is detected in the northern region (Fig. 44). Associated with the specific humidity at 500mb (Fig.45), it corroborates features seen from the surface precipitable water which still indicates a propagating wave-like structure making the north of Madagascar one key area extremely sensitive to wet events during the active phase of monsoon (Fig. 46).

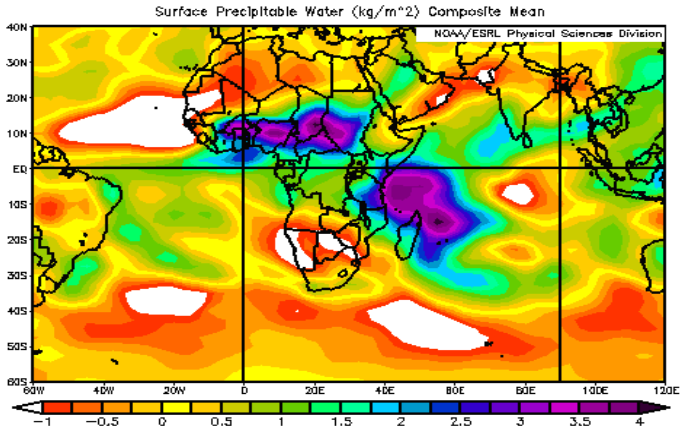

Figure 46: Regional Composite surface precipitable water pattern.

c) Third extreme mode dynamics

Until recently, knowing the common misunderstandings about PCA gives the source to use the proposed techniques to analyze global weather measurements. Measurements of some major atmospheric variables are used to describe the third main feature of the rainfall over Madagascar. Meanwhile, the underlying physical mechanisms patterns have not only significant difference from PC3 regarding the East-West contrast but also exhibit unexpected and prominent maps.

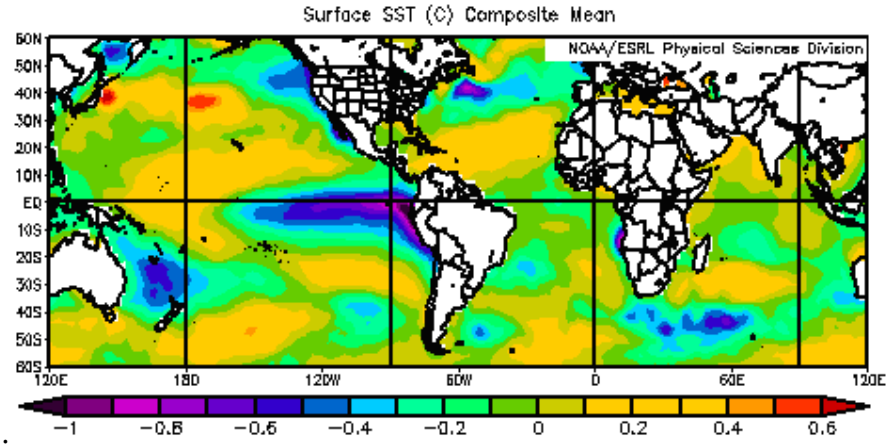

Figure 47: Global tropical SST composite pattern (^{o}C).

Derived from the correlation studies of the surface variables used considerable link is identified between Indian Ocean SST at (40-70^{o}E, 40-50^{o}S) (Fig. 47) and African OLR at (0-

20^oE, 10^oN-0^oS) (Fig. 44) with r^2=0.53. Similarly, teleconnection is detected between North Pacific Ocean (NPO) OLR anomaly and the North Atlantic Ocean (NAO) SST composite patterns with significance 54%.

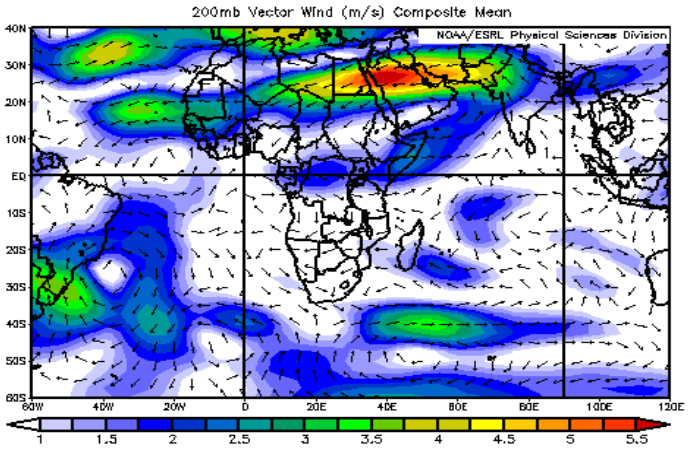

Figure 48: Regional composite wind circulation pattern in the upper level.

Moreover, the regional wind circulation features from the upper (Fig. 48) to the lower level elucidates the coupling of mid latitude and tropical systems in the Indian Ocean to form upper level divergent flow. This environmental influence generally has the unfortunate effect of weak prediction of the specific humidity producing less moisture in the north and more moisture in the south (Fig.49) embedding Madagascar. As follow, this process is enhancing insufficient moisture in the lower level in the eastern despite its classification in the most 'sprinkled' region of Madagascar. Based on the large-scale circulation features, the underlying composite patterns are representing a good agreement between areas of upper-air divergence and area of convection inferred from the Outgoing Longwave Radiation (OLR) satellite data (Fig.50). South American OLR can also explain the third Malagasy rainfall pattern after proceeding with Pearson correlation test (see Appendix) reaching 99% level of significance i.e over southern America attaining the Atlantic Ocean dominates the regional connection.

However, the contrast East-West consistent with PC3 pattern reappeared from the composite surface precipitation rate pattern. The specific humidity composite shows the possibility of having rain in the extreme south region of Madagascar during summer season remarkably with a very small amount.

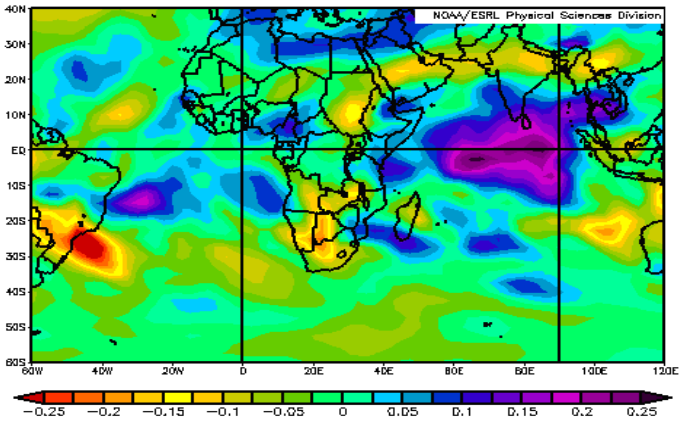

Figure 49: Regional composite specific humidity pattern in the mid level.

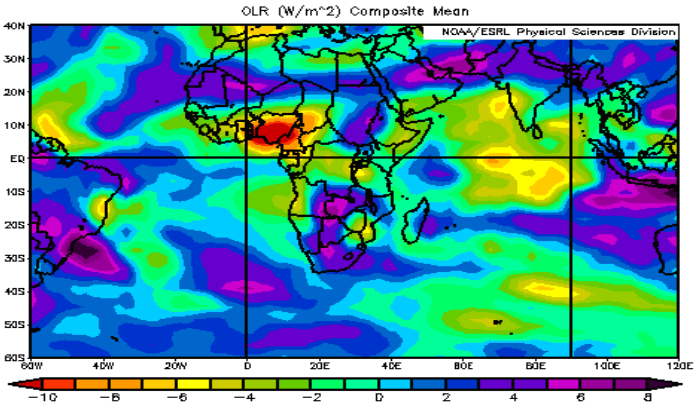

Figure 50: Global Composite OLR pattern.

Three dimensional atmospheric analysis illustrated by the velocity potential describes the evidence of two distinct centres of action that could be defined as Pacific Ocean – America dipole. Most of the divergent and convergent flows are concentrated respectively in the Pacific Ocean and America (Fig.51).

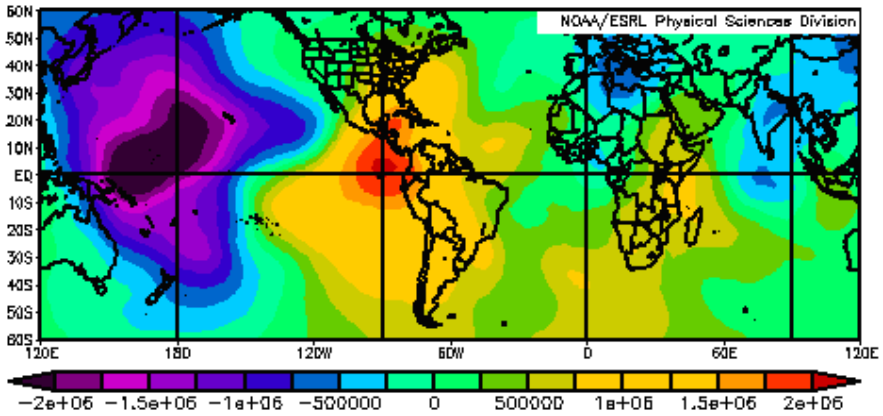

Figure 51: Composite upper Velocity Potential pattern significantly defining contrast between the Indian Ocean and the Pacific Ocean.

1.6. Conclusion

The reduction of the dimension of the monthly rainfall over Madagascar from 1951 to 2000 through the PCA methods is thus able to bring out the dominant spatial and temporal patterns with the most prominent interannual variability such as 1983, 1991, and 1997.

The most meaningful of the extracted components may not even exist however the most important thing is the one closest to the index used to characterize phenomenon displaying in contemporary climatology. Therefore, it is identified by the first component that Madagascar rainfall is directly linked to the QBO and the TC index. From the second component, the contrast between North and South is more highlighted. This feature could be modulated by the Southern Oscillation (ENSO, SOI). The third mode describes the polarity between Eastern and Western region of Madagascar. This is an evidence that local effect such as the orography influence is present even during the summer season.

Notice that the extraction technique adopted provided the dimension reduction of the rainfall data were able to reveal the dominant physical process that gives rise to rainfall in the country.

Understanding the physical mechanisms responsible for the occurrence of the main rainfall patterns over Madagascar is one key issue resolved here. For better understanding, salient factor that determines these modes are investigated. Thus, the leading mode representing almost 49% of the rainfall could be optimally derived as a contrast between the North and the South stating that the southern region receives less precipitation than the northern region. Consistently, this polarity is shifted to NE and SW provided that 24% of the rainfall datasets constitutes the second mode. Conversely, strong East-West opposition is depicted from the third mode explaining almost 10% of Madagascar rainfall. It can be assumed that the relief effect hardly contributes to the rainfall occurrence during the summer season because of the extra-tropical trade winds shift in its easternmost geographical location. All in all, synergy between the dynamical variables is fundamentally the mechanism modulating rainfall over Madagascar.

Chapter 2: Tropical cyclone role in the modification of Madagascar climate

2.1. Introduction

Recently, Purdue University researchers have found evidence that tropical cyclones and hurricanes play an important role in the ocean circulation patterns that transport heat and maintain the climate of North America and Europe (Purdue University Researchers, 2007). This research provides evidence that hurricanes may be one of the missing pieces in the climate modeling puzzle.

However, in some area such as Madagascar, there is no doubt that the climate is modulated by the tropical cyclone and storms since it is surrounded by the Indian Ocean in the east and the channel of Mozambica in the west. Previous studies of principal component analysis allow us to estimate that one source of explanation about the main rainfall pattern is the tropical cyclone phenomenon crossing this island.

The objective of this study is to highlight how the tropical cyclone modulates the climate over Madagascar.

Different steps will be adopted in order to achieve this goal such as analysis based on the cyclogenesis formed in the Indian Ocean basin and its susceptible effect. It will be followed by the direct impact of this phenomenon over Madagascar and end by the local contribution of the tropical cyclone in the different regions during the rainy season.

2.2. Data and Method

In this analysis, we make use of the tropical cyclone tracking information offered by http://www.weather.unisys.com/ in the southern hemisphere. Then, Tropical Cyclone indices datasets collected and archived by the La Reunion Regional Specialized Meteorological Centre (RSMC) restricted in the Western and Central portion of the South Indian Ocean (West of 100^{o}E) are also included in this study. Finally, we produce our results from Malagasy regional rainfall basically extracted from VASClimO dataset (Variability Analysis of Surface Climate Observations) by Beck and Rudulf (2004) using data from 1951 to 2000 at 0.5^{o} resolution.

Simple Pearson correlation method has been applied to these data in order to detect and investigate the possible relationship between the variables.

2.3. Results

a) Cyclogenesis scenario in the Indian Ocean basin

a-1) Tropical cyclone formation

Several conditions must be met before tropical cyclones can form. Updated recently, the necessary conditions for TC Genesis can be read from the review of Lin (2007) entitled Mesoscale Dynamics. Briefly, from his findings,

1. a large body of ocean water of at least 26.5^{o}C, throughout a sufficient depth at least 50 m to provide the thermal energy;
2. Sufficiently large planetary vorticity, i.e. a distance of at least 500 km from the equator, so that the near gradient wind balance can occur;
3. A near-surface preexisting disturbance with sufficient localized vorticity and convergence, such as easterly waves, to generate a convergent low-level wind,

triggering convection, and helping to organize and sustain the mesoscale convective systems and cloud clusters;

4. Divergence associated with an upper-level trough overlaying the low-level cyclonic disturbance to enhance and sustain the deep upward motion;
5. A potentially unstable atmosphere to allow the heat stored in the ocean to be released for the tropical cyclone development;
6. Relatively moist middle troposphere for allowing the continuous development of widespread thunderstorm activity; and
7. Weak vertical wind shear, with less than 10 ms-1between the ocean surface and the tropopause, to avoid the disruption of the vertical development of deep convection around the cyclone center.

a-2) Indian Ocean environment during the summer season

Unlike the Channel of Mozambica, Indian Ocean basin is one of the most effective locations where the tropical cyclone and storms are formed.

All the basins susceptible to this phenomenon have their own seasonal profile after extracting the cyclone tropical events in the station implanted in the vicinity of each basin considered.

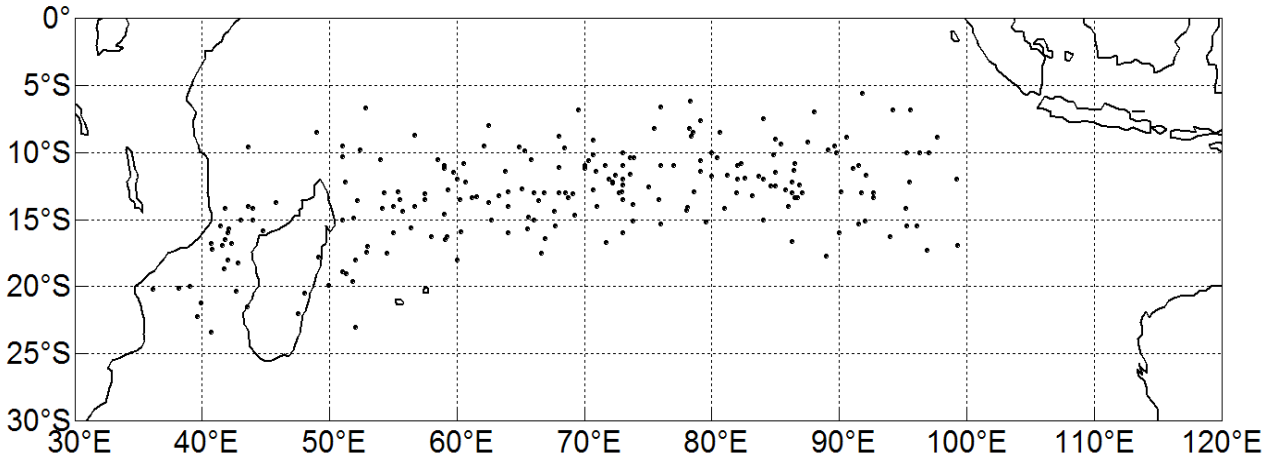

Figure 52: Cyclogenesis from 1979 to 2004: Geographical distribution **(**Bessafi and Wheeler, 2005).

Hence, this observation provides evidence that hurricanes play an important role in the climate of Madagascar. Effectively, Madagascar Island is "swimming" in a zone favorable to the cyclogenesis that occurs during the austral summer season. By restricting to the longitude from 30°E to 100°E and the latitude from 5°S to 25°S, it can be estimated that since 1979 until 2004, 75% of the cyclogenesis were born in the Indian Ocean and the remaining in the Channel of Mozambica. (Fig. 52)

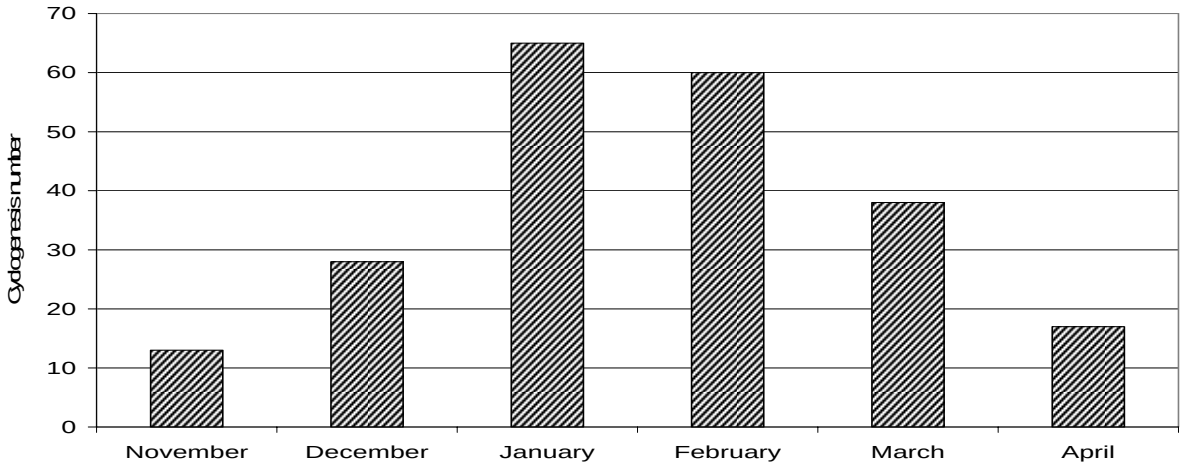

Figure 53: Cyclogenesis per month from 1979 to 2004: Number of cyclogenesis (Bessafi and Wheeler, 2005).

Figure 53 is a supplement of the Fig. 54 since it shows the number of cyclogenesis per month at the same place and at the same period. It can be deduced from this figure that the cyclonic activity begins in November and ends in April defining the summer season over Madagascar. Monthly number of cyclogenesis in January is recorded 65 times within 25 years in the period 1979 to 2004.

b) Tropical cyclone impact over Madagascar

Further analysis can be dwelled from the cyclone tracking specifically in the Southern Hemisphere provided by the http://www.weather.unisys.com/. Obviously, counting hurricanes and storms touching Madagascar inland is one of our interests from this offered trajectory information.

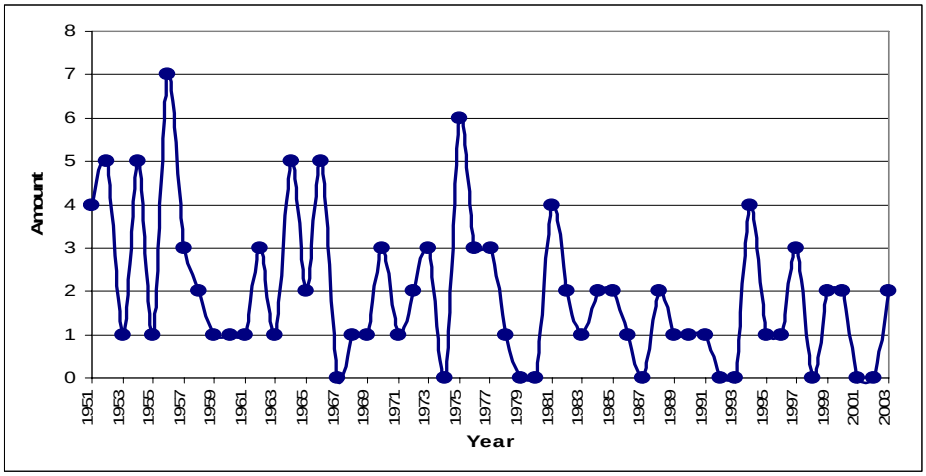

Figure 54: Storms and tropical cyclones hitting Madagascar from 1951 to 2003.

Hence, Fig. 54 shows the yearly total amount of the tropical storms and cyclones hitting Madagascar from 1951 to 2003. This will help to diagnose and observe the connection between the resulting tropical cyclones affecting the island and its intra seasonal rainfall variability. Apart from happening over a certain area for a defined amount of time, it is also sporadic and cannot be easily predicted. From this chart also can be identified some critical events such as the severe drought in 1992 plaguing especially the southern Madagascar and

causing 200 deaths can be identified. The famous Sea Surface Temperature anomalies from January 1991 to July 1992 mixed with the Outgoing Longwave Radiation anomalies in the same period 1991-1992 throughout the globe enhanced El-Niño event blocking the mechanism to produce heavy rainfall which is the fundamental water resource in this area.

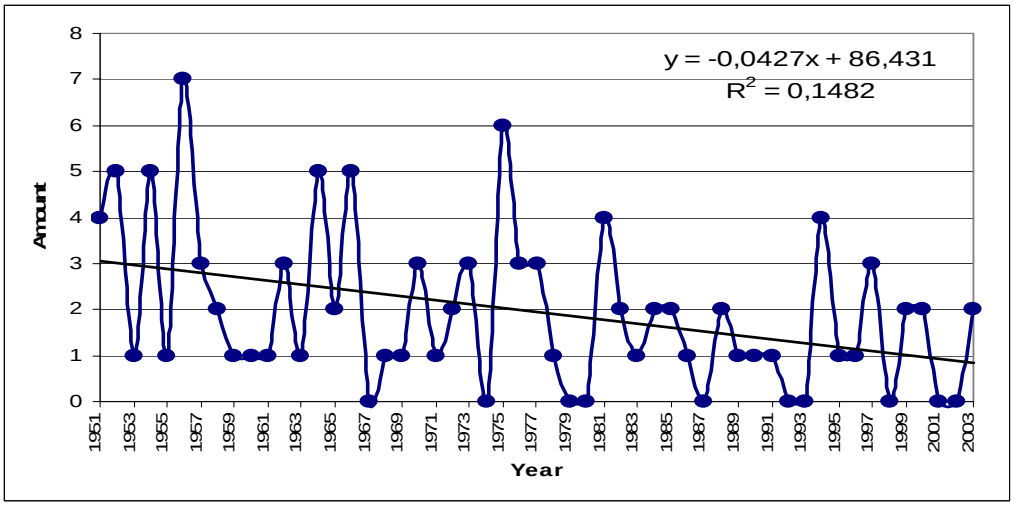

Figure 55: Trend of the Malagasy tropical cyclone.

The maximum number of storms recorded in 1956 stirring toward the island is seven. This episode indicates that SST anomalies tend to form favorable conditions for convective activity and may sustain enhanced precipitation anomalies over the convergence region. Despite this vital explanation, the process of getting cyclone is being curtailed after evaluating the number of storms trend (Fig. 55). Based on the Pearson correlation statistical test of 99% significance, Madagascar risks a severe shortage of rain water in the next five decades if few tropical cyclones reach the island.

The following three composite results (Fig. 56a,b,c) exhibit prominent behaviour based on two successive climatology time period which are 1951-1976 and 1977-2002.

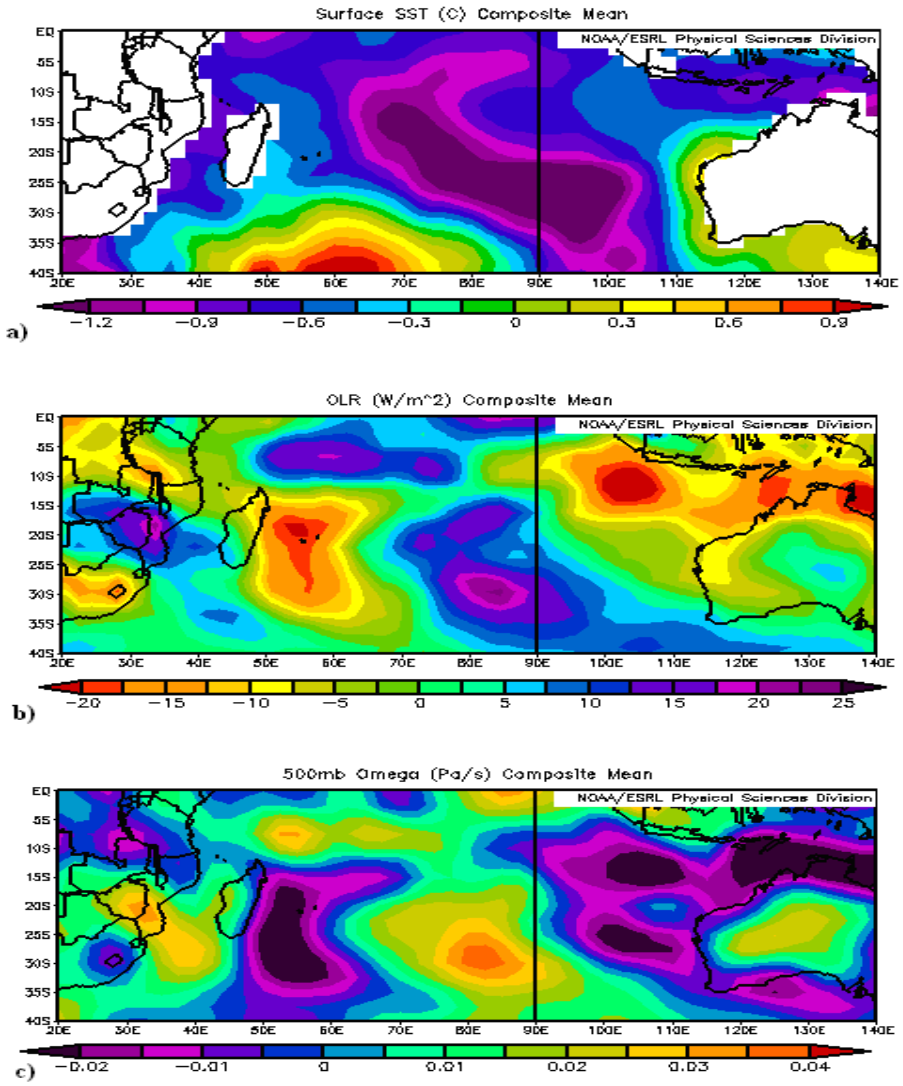

Figure 56: Mean Composite Patterns between two successive 25 years climatology time period: a) Sea Surface Temperature, b) Outgoing Longwave Radiation, c) Mid-level Omega.

Moreover, monthly mean composite analysis reveals a clear distinction between these two time periods which clears doubts if the climate changes from score and decade to another. In the past 25 years, the favourable conditions allowing the tropical cyclone to develop are important and justified by the combination between warm SST, high convective activity according to the OLR anomaly, and upper-level outflow resulting moisture in the immediate basin where Madagascar is included. This yields expected precipitation reduction for the next 25 years enhancing desertification in the near future.

From Fig. 57, January is observed to be the wettest month recorded getting more than 80 storms in different categories within 52 years. April is the month with a poor number of cyclones, less than 10. It is identified from the same plot that Malagasy rainfall is modulated by the tropical cyclone since the cyclonic period is developed in austral summer season. Furthermore, intra seasonal rainfall variability determined by the mentioned strong phenomenon characterizes the climate over Madagascar.

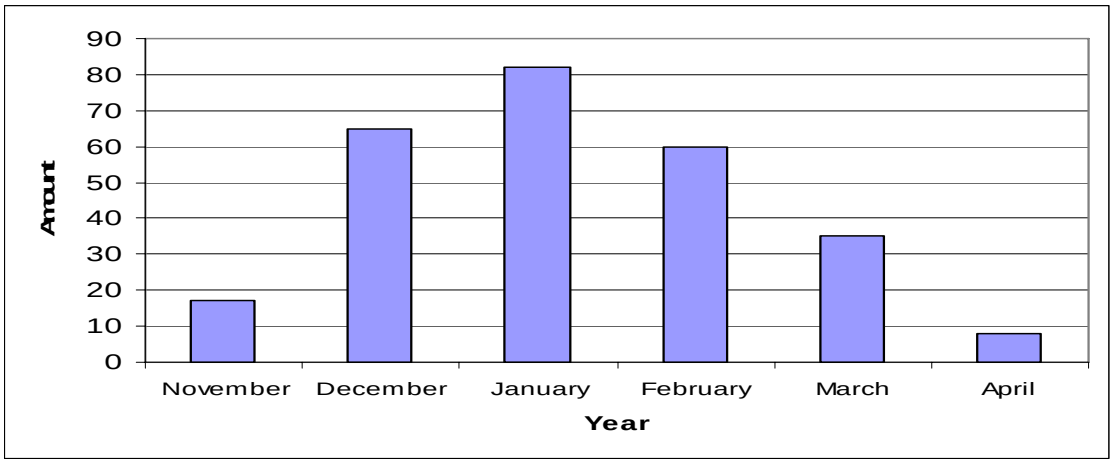

Figure 57: Storms and tropical cyclones hitting Madagascar during the summer season.

c) Characteristics of the basin during the active phase of the austral summer season

In order to understand the mechanism responsible for seasonal change, investigation based on the dynamical variables over the southern Indian Ocean basin is led from December to February. It can be identified that each month has typical description regarding what is happening in the basin while considering the climatology time period 1951-2003.

c-1) December

As shown in Fig.58a,b and c, the southern Indian Ocean basin is exactly characterized by a lower level cyclonical circulation located in the middle (60-100^{o}E;12-32^{o}S). Deep convections enhancing upward motion are also detected at (50-70^{o}E; 12-27^{o}S) connecting the first key location and Madagascar. Evidently, a huge amount of moisture is filtered at the mid-

level of the atmosphere related to this 'strategic' location. Therefore, eastern Madagascar is the immediate region benefiting from this in terms of water resource.

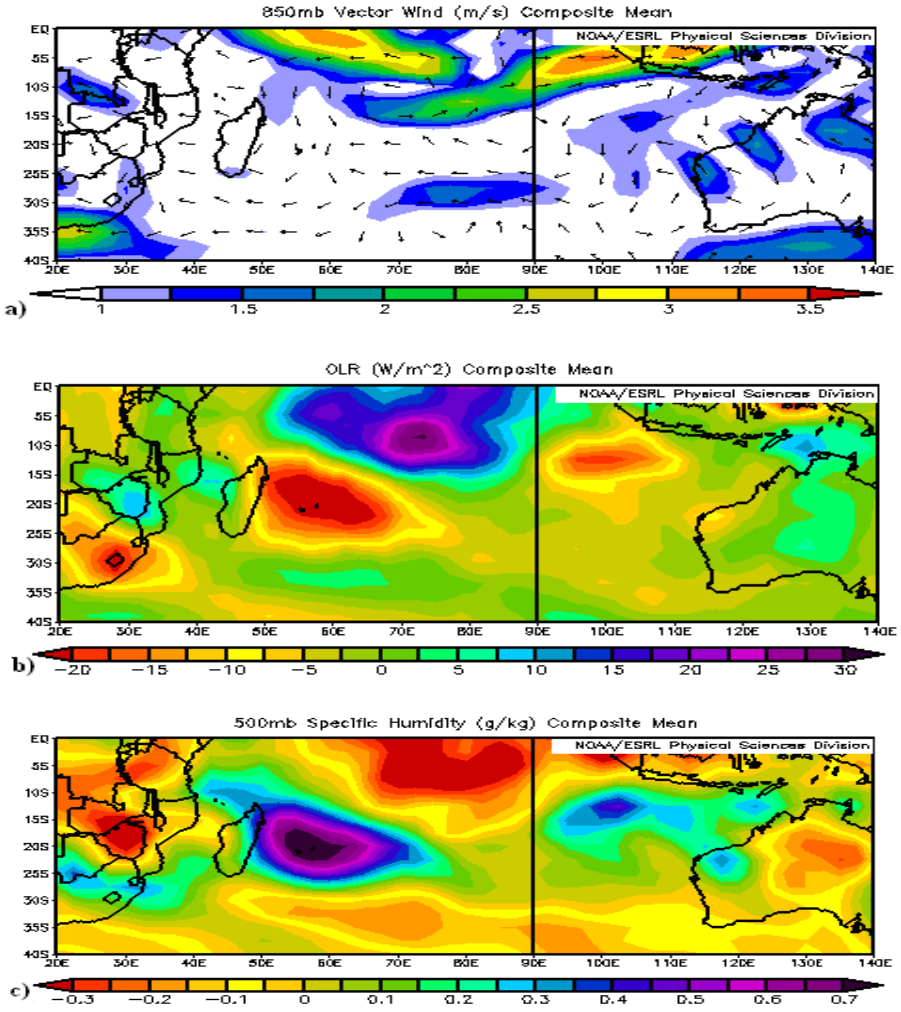

Figure 58: January Mean Composite Patterns for 1951-2003 climatology time period: a) Low-level wind vector, b) Outgoing Longwave Radiation, c) Mid-level specific humidity.

c-2) January

January event differs from December by the presence of an additional favorable condition to the cyclogenesis along the channel of Mozambica. As shown by the mean composite features (Fig. 59a,b,c), cyclonical circulation is directed to the Southern Africa reaching Mozambica. It results deep convection and upward motion if we look respectively at the OLR and mid-level Omega over Mozambica and slightly affect Madagascar occident region.

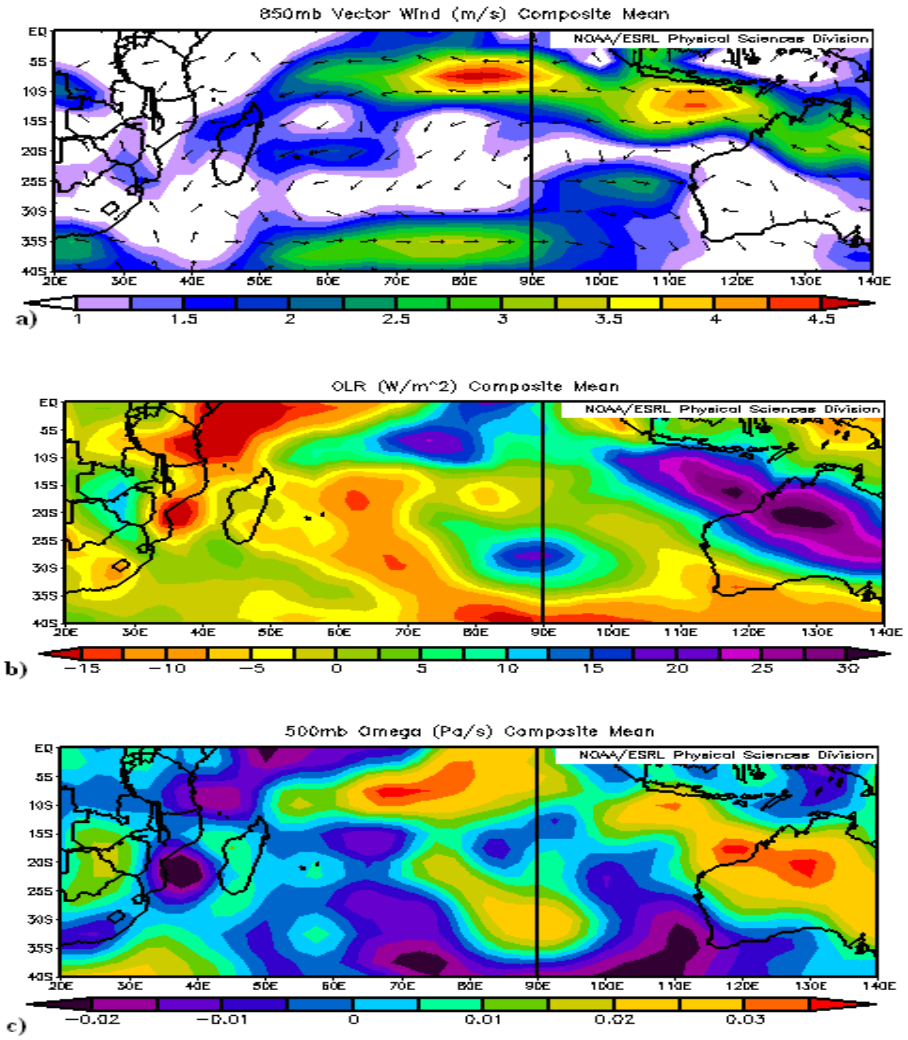

Figure 59: January Mean Composite Patterns for 1951-2003 climatology time period: a) Low-level wind vector, b) Outgoing Longwave Radiation, c) Mid-level Omega.

Moreover, deep convective activity is observed in that area. Obviously, the number of storms is susceptible to reach maximum in January and found to be the basic explanation of the peak number of either cyclogenesis in the southern Indian Ocean or cyclone tropical registered introducing Madagascar.

c-3) February

The current cyclonical circulation depicted in the mid-southern Indian Ocean basin is shifting toward the south letting the anti-cyclonic circulation growing instead. Generally, a warm and

small ocean temperature gradient ocean, more than 5° from the equator, a surface trough overlain by small wind shear through the troposphere, and an essential condition of intense divergence outflow in the high troposphere are almost inspected in the extra tropical zone according to the three following plots (Fig. 60a,b,c). Consequently, these conditions play an important role as well as inhibit the tropical cyclone affecting Madagascar making the record numerous in December and January.

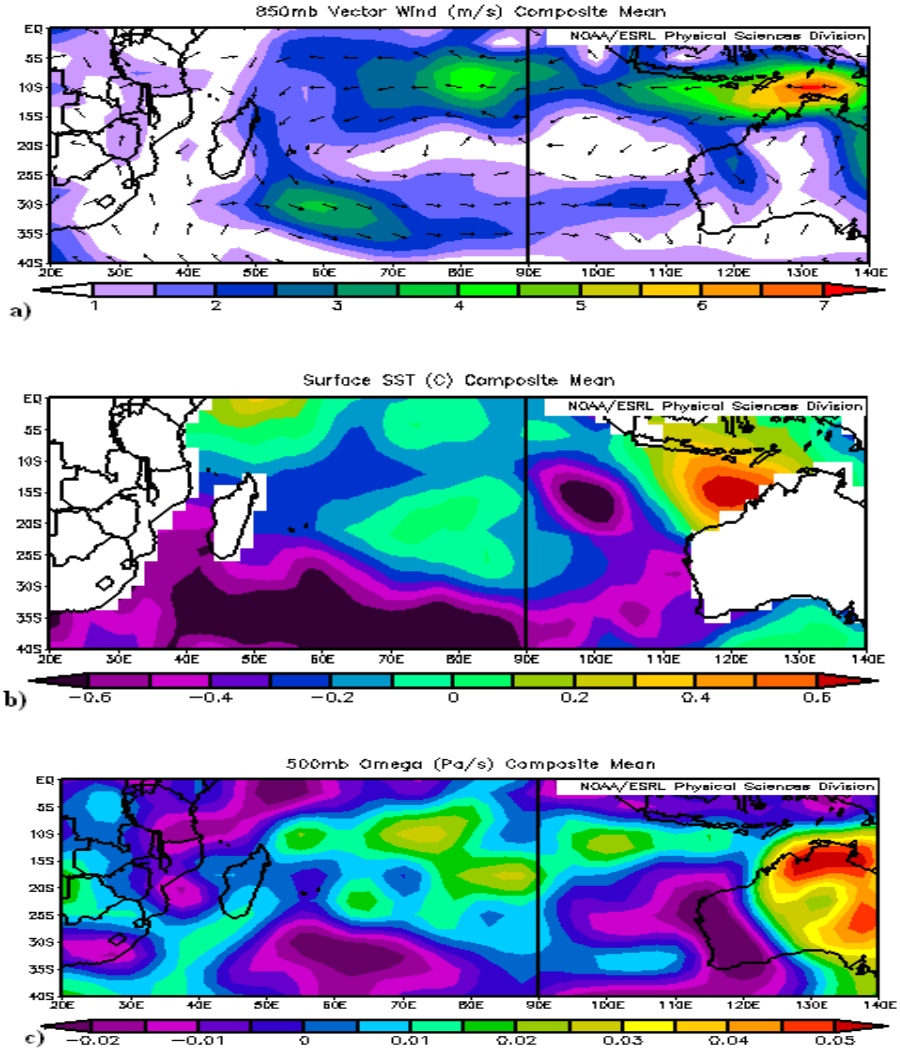

Figure 60: February Mean Composite Patterns for 1951-2003 climatology time period: a) Low-level wind vector, b) Sea Surface Temperature, c) Mid-level Omega.

d) Local contribution of the tropical cyclone

Malagasy regional rainfall data have been correlated with the tropical cyclone indices data from 1951 to 2000. It is assessed that there is relationship between the tropical cyclone and the eastern region. Local statistical significance at 95% significance level is obtained with Pearson simulation window (Table 3).

Table 3: Correlation table between regional rainfall and tropical cyclone (TC) indices

	TC	East	Highland	West	South
TC	1	*0,26	0,21	0,12	0,06
East	*0,26	1	0,92	0,60	0,48
Highland	0,21	0,92	1	0,76	0,60
West	0,12	0,60	0,76	1	0,66
South	0,06	0,48	0,60	0,66	1

*Correlation is significant at the 95% significance level.

The significant relationship between the TC and the eastern region explains the classification of this region into the very humid climate. Moreover, the eastern region is exposed directly to the Indian Ocean where a great number of cyclogenesis is being monitored during the austral summer season.

Nevertheless, weak correlation depicted specifically in the southern region improves our lack of understanding of the relationship between tropical cyclone and rainfall over the semi-arid part in which southern is categorized. Similarly, the amount of rainfall in the western is associated with 25% of the cyclone formed in the channel of Mozambica. This percentage is low to establish linearity between these two distinct time series. As far as the highland concerned, its location next to the eastern region could give more explanation to the insufficient correlation coefficient. Unlike the western region, precipitation recorded in the

highland is a bit less than the rainfall recorded in the east because the maximum of moisture 'inundates' the eastern region before penetrating into the centre. (Fig.61)

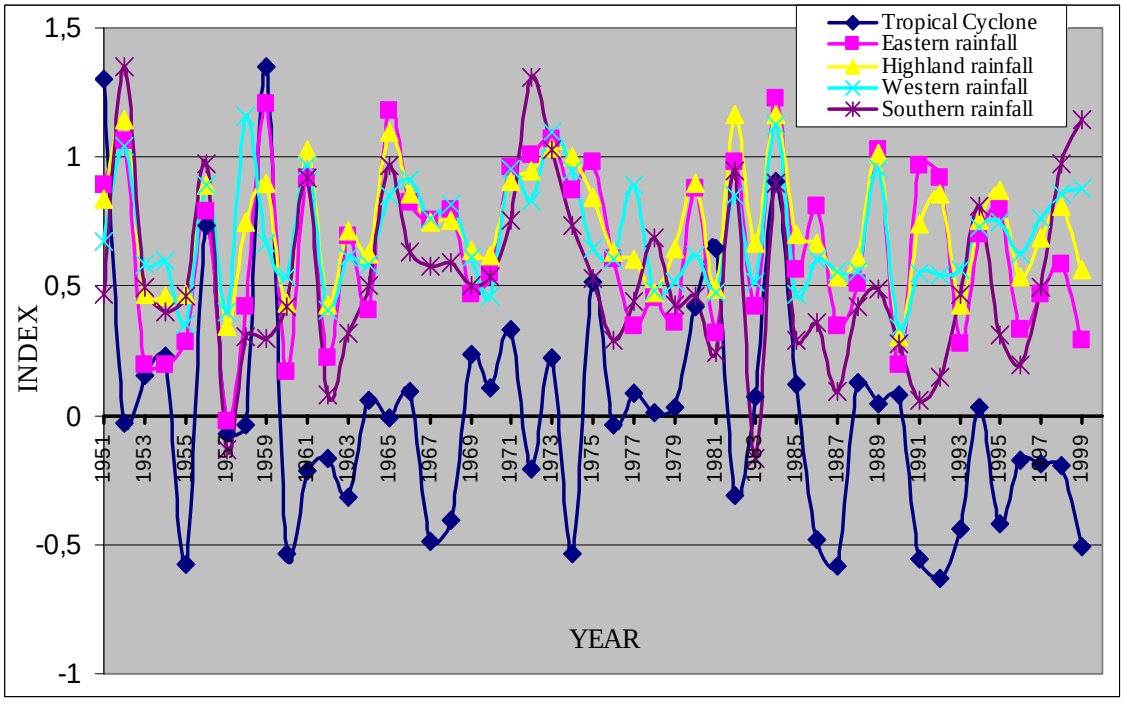

Figure 61: Malagasy standardized regional rainfall combined with the tropical cyclone indices in the period 1951 to 2000.

Besides, there are events in which the tropical cyclone indices and the regional yearly time series within the period 1951-2003 rarely coincide. By setting blinders, however, other phenomenon may induce the mechanism responsible for producing or not producing rainfall over Madagascar during the austral summer season. But hopefully in this work, we search for meaningful physical explanation by employing monthly composite analysis which would possible give more insight to the prevailing mechanism inducing severe or poor moisture in the area of study.

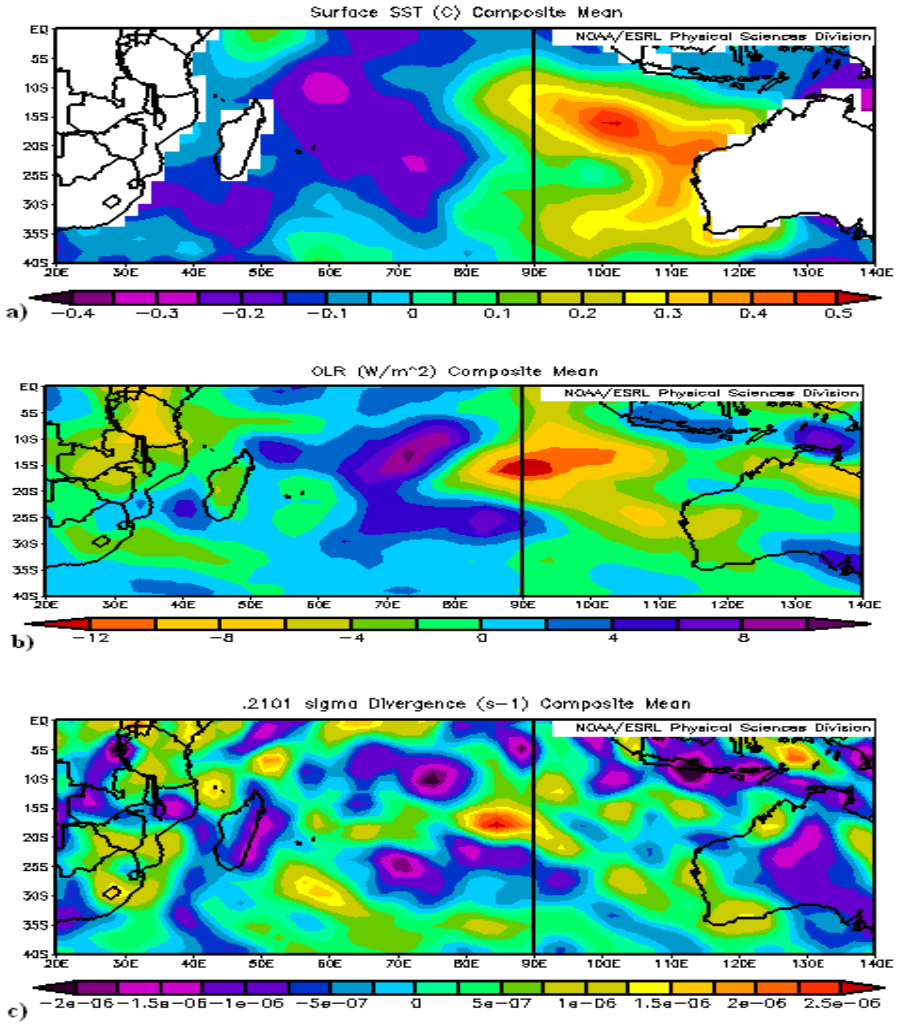

Figure 6372: Mean Composite Patterns for 1951-2003 climatology time period considering tropical cyclone years coinciding to wet and dry events: a) Sea Surface Temperature, b) Outgoing Longwave Radiation, c) Upper-level divergence.

Consequently, it appears from the illustrated results (Fig.62a,b,c) that despite the warmer SST surrounding the island and its measly embedded negative OLR anomaly, weighted downward motion measured by the negative upper-level divergence generating low-level subsident motion is proceeding to diminish the positive effect of the cyclogenesis. Thus, it is certainly assumed from this study that the heat is increasing with a very high speed in the southern Indian Ocean more specifically in Madagascar. Moreover, El-Niño Southern

Oscillation phenomenon could be more frequent and more virulent (so more destructive) in a measure the temperature anomaly dramatically goes up.

2.4. Conclusion

The analysis suggests that tropical cyclone can never be neglected from the rainfall climatology of Madagascar. It is also found from the correlation analysis that there is a relationship between the eastern region and the tropical cyclone. The amount of rainfall in each region is influenced by the cyclone passage despite its lack in number.

The key factor prohibiting the rainfall occurrence is the observed SST anomalies which is one of the crucial conditions for tropical cyclone development. Generating El-Niño event, almost the whole island was strongly affected.

The conclusion that can be drawn from this study is the tropical cyclone phenomenon ability to modify the climate over Madagascar which is responded exclusively by the rainfall recorded in that area.

Part III: Extreme value theory applied to the regional precipitation data of Madagascar

Summary

Extreme events of Malagasy rainfall going beyond the normal state are detected. SPI method (Standardized Precipitation Index) introduced by McKee, T.B., N.J. Doesken and J. Kleist, (1993) is particularly applied. However, SPI method is hardly linked to the gamma distribution because the rainfall record is not distributed normally as Gaussian distribution. Moreover, Generalized Extreme Value and Generalized Pareto distribution of Madagascar rainfall studies are also established by using VASClimO (Variability Analysis of Surface Climate Observations) dataset in the period 1951-2000 at 0.5^{o} resolution. The tail studies are expected to answer one of the most interesting questions: what are the extreme events? Have we already seen the heaviest ones or are we going to experience even heavier events? Answers to such questions are essential. It turns out that we can answer these questions within the framework of extreme value theory analysis using a code developed using MATLAB.

Chapter 1: Standardized Precipitation Index

1.1-Introduction

Extreme precipitation events in Africa can be related to a variety of catastrophic events including drought, famine, flooding, and the spread of disease. Due to a variety of factors infrastructure is not set up to alleviate the stress caused by these extreme events, leaving Africa more prone to such precipitation-related disasters. It is important to attempt to anticipate when these extreme events are likely to occur so that disaster relief efforts can be implemented and reduce the potential impacts of such extreme events.

The fact that Madagascar is located in the Indian Ocean and also part of Africa, a number of studies has so far been done in these large areas. Among those studies are the climate of Madagascar and relationships to Southern Africa (Jury and Raholijao, 1991), modification of the southern African rainfall variability/ENSO relationship since the late 1960s (Richard et al., 2000), structures and mechanisms of South Indian Ocean Climate Variability (Xie et al., 2001). However, this chapter is devoted to the development of a method for applying the standard precipitation index (SPI) to the different regions of Madagascar which was not considered previously.

The goal of this research is to analyze the dry episodes in order to monitor and prepare areas that may be susceptible to food shortages. Therefore, this chapter **is** started with the introduction of the datasets and followed by the methods used in the study. The results and interpretations are presented next ended by the conclusion.

1.2. Data

Although various methods of restitution have been applied earlier, there is still uncertainty in terms of the quality of the data provided since the time series itself present a high number of inhomogeneities and discontinuities. In order to avoid such discrepancies, our further analysis would be based directly on Madagascar monthly rainfall series extracted from the global Land Areas gridded climate dataset (VASCLIMO) for the period 1951 to 2000 (Beck and Rudulf, 2004) with a spatial resolution of 0.5^{o} x 0.5^{o}. Such analysis requires reliable high quality precipitation fields, thus the precipitation data from the stations have to meet such standards. In fact, only station time series with 90% minimum data availability during the period (1951-2000) are used for interpolation to a regular 0.5° x 0.5° grid in order to minimise the risk of generating temporal inhomogeneities in the gridded data due to varying station densities. Thus, the resulting gridded dataset is highly suitable for the application in studies concerning long-term aspects of climate variability, such as SPI, GPD, etc. In order to minimize the uncertainty, the statistical analysis demands long time data series, at least 50 years of daily records.

Regional Data: From the gridded data, we built one regional data time series which is composed of 59 coordinates and quite similar to the stations used in part I chapter 1. Admittedly, most of these coordinates do not coincide exactly with these stations but to its closest neighbour within 0.5^{o} x 0.5^{o} resolution. Effectively, the idea of regionalisation rises from this ambiguity and leads us to define the correlation between the data before taking their average that serves eventually for regional rainfall data.

The following map shows how the 56 coordinates are split up into groups according to their correlations. Thus, the analysis applied to the monthly mean precipitation time series of nine regions of the island respectively based on 7, 10, 10, 4, 7, 7, 4, 4, 6 stations, is shown on (Fig. 63)

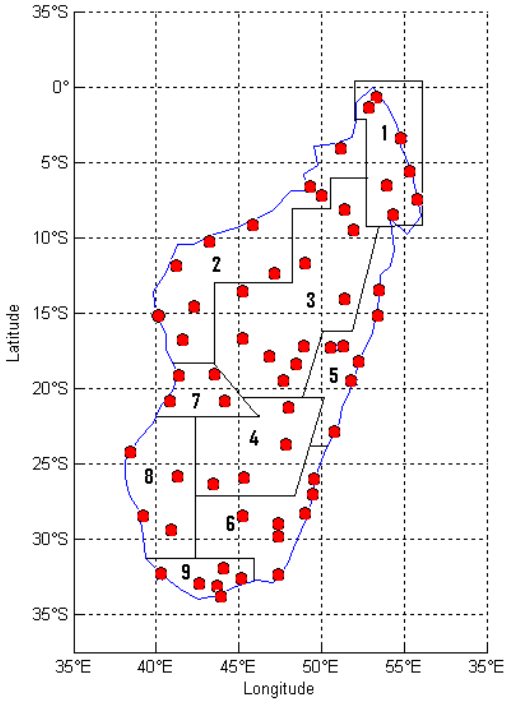

Figure 63: Location of 59 coordinates and their subdivisions

1.3. Methods

a) Factors affecting rainfall anomalies

Many factors at work may determine the rainfall variation of Madagascar, and Africa in general. These factors combine to create the short-term and seasonal weather at any location. In fact, the rain in the east region is typified by a bimodal seasonal precipitation distribution but demonstrating only a single rainfall season in the other areas. As mentioned in the previous chapter, rainfall in Madagascar is due primarily to the latitudinal procession of the ITCZ with the zone of maximum incoming radiation. In addition to the movement of the ITCZ, Ropelewski and Halpert (1987) highlighted that African region including Madagascar has entirely a coherent response to warm ENSO events. Hence, rainfall has been shown to vary with El Niño events. Due to an equatorward shift of the ITCZ, extreme Southern region tends to experience dry conditions during the austral summer following El Niño events.

In the study by Nicholson and Kim (1997) about the African rainfall response to ENSO events concludes that the important factor regarding the rain forecasting is to understand how ENSO events affect the SST of the Atlantic and the Indian Oceans. The relative importance of El Niño versus Indian Ocean SSTs in affecting African rainfall especially the southern part is tested using modeled analysis (Goddard and Graham, 1999). This study found that the dominant SST anomalies in the Indian Ocean, where Madagascar is located, were a larger contributor to rainfall patterns in southern Africa including Madagascar than Pacific SST anomalies. In addition to the ENSO cycles, there has been research performed on the effect of the QBO on rainfall in that area. (Mason S.J., Lindesay J.A., 1993) studied how the phase of the QBO, along with extreme SOI events, impact southern hemisphere summer rainfall in southern Africa. This study showed that during the westerly phase of the QBO, high SOI years produce wet conditions over southern Africa while low SOI years produce dry conditions. However, during the easterly phase of the QBO the association between rainfall and SOI phase is statistically meaningless. Another finding of this research was that early season rains (October – December) were unaffected by the phase of the QBO. The conclusion of this study notes that during the peak rainfall season of southern Africa, the effects of SOI on rainfall are only valuable during the westerly phase of the QBO.

Other factors have also been tied to rainfall, especially anomalous amounts, in southern Africa. Mason S.J. and Tyson P.D. (1992) found a link between rainfall and solar activity during the easterly phase of the QBO. This study showed that an increase in solar activity early in the rainy season lead to an increase in rainfall early in the season but a decrease late. Other studies found a relationship between increased carbon dioxide and anomalous short-term rainfall events. Indeed there may be many factors at work in determining the rainfall variation in our area of study. These factors combine to create the short-term and seasonal weather at any location.

b) Standardized Precipitation Index

The SPI was introduced (McKee, T.B., N.J. Doesken and J. Kleist, 1993) as a method of measuring drought severity for a particular rain station. The SPI attempts to standardize precipitation values in an attempt to calculate a z-score for new values. For a normal distribution the z-score is the difference of a value from the mean divided by the standard deviation.

The main advantage of the SPI is that it allows for areas with different rainfall regimes to be compared. What constitutes a "drought" in a tropical area might be the same rainfall amount that would be considered "heavy rain" in a desert region. The SPI provides a method for comparing an area against its own history and giving a normalized value to describe the current rainfall conditions. Through this normalization, rainfall values at different locations can be compared.

The challenge is using an appropriate time scale. McKee analyzed time scales varying from three months to 48 months. One discovery from this work is that at time scales of less than 12 months, McKee found that the data was not normally distributed. To correct this non-normal distribution the data was fitted to the gamma distribution to capture the probability of precipitation (Fig.64).

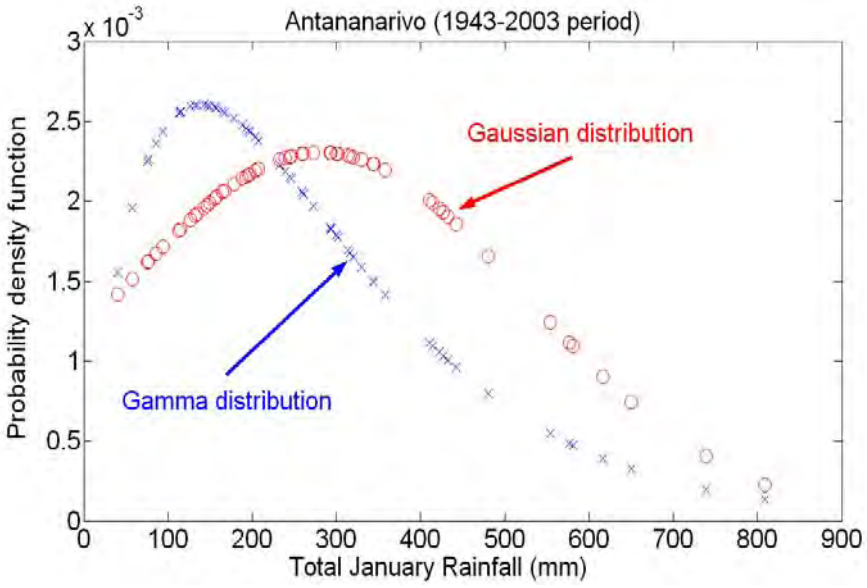

Figure 64: Probability density function.

The gamma distribution uses two parameters to define the curve. The alpha parameter describes the shape of the curve. An extremely low alpha corresponds to a curve that is quite similar to an exponential decay function. Large shape value corresponds to near-normal distributions. The beta parameter describes the scale of a curve. This coefficient will describe the values associated with the distribution. These two parameters together describe a wide array of possible rainfall regimes, making the gamma distribution an intelligent choice for precipitation patterns. Hence, gamma distribution linked to the SPI is defined

$$g(x) = \frac{1}{\beta^{\alpha}\Gamma(\alpha)} x^{\alpha-1} e^{-x/\beta} \qquad (25)$$

for x >0. As can be seen, g(x) uses two parameters to define the curve

$$\alpha = \frac{1}{4A}\left(1+\sqrt{1+\frac{4A}{3}}\right) \qquad (26)$$

which is the shape of the curve and the scale of the curve $\beta = \bar{x}/\alpha$ (27).

The A is an intermediate step in the calculation of the shape parameter α.

$$A = \ln(\bar{x}) - \frac{\sqrt{\ln(x)}}{n} \qquad (28)$$

with x the monthly precipitation value and n the number of precipitation observations.

$$\text{Therefore } \bar{x} = \frac{\sum_{i=1}^{n} x_i}{n} \qquad (29).$$

Once A is calculated, the shape can be estimated. The objective of this next step of computation is to have gamma distribution g(x) similar to Gaussian distribution through the cumulative probability given by: $G(x) = \int_0^x g(x)dx = \frac{1}{\hat{\beta}^{\hat{\alpha}}\Gamma(\hat{\alpha})}\int_0^x x^{\hat{\alpha}-1}e^{-x/\hat{\beta}}dx$ (30).

However, zero values which may contain into the precipitation distribution have made gamma function undefined otherwise x=0. In that case, the cumulative probability becomes:

$$H(x) = q + (1-q)\, G(x) \qquad (31)$$

where q = m/n, is a zero probability, m is the number of zero value, n is the number of observed precipitations. Now, the Z or SPI value is more easily obtained computationally using an approximation provided by Abramowitz and Stegun (1965) that converts cumulative probability to the standard normal random variable Z:

$$\begin{cases} Z = SPI = -\left(t - \dfrac{c_0 + c_1 t + c_2 t^2}{1 + d_1 t + d_2 t^2 + d_3 t^3} \right) & \text{for } 0 < H(x) \le 0.5 \\ Z = SPI = +\left(t - \dfrac{c_0 + c_1 t + c_2 t^2}{1 + d_1 t + d_2 t^2 + d_3 t^3} \right) & \text{for } 0.5 < H(x) < 1 \end{cases} \qquad (32)$$

$$\text{where } t = \sqrt{\ln\left(\frac{1}{(H(x))^2}\right)} \text{ for } 0 < H(x) \le 0.5 \quad (33)$$

$$\text{and } t = \sqrt{\ln\left(\frac{1}{(1.0 - H(x))^2}\right)} \text{ for } 0.5 < H(x) < 1.0 \quad (34).$$

With c_0=2.515517; c_1=0.802853; c_2=0.010328; d_1=1.432788; d_2=0.189269; d_3=0.001308

1.4 Results and interpretations

When interpreting the SPI, it is critical to have an understanding of the time interval used to create the values. In this context an interval is defined by the length (how many months) and timing (when the months fall during the year) of the period. The interval used in calculating the SPI will determine the impacts an extreme value may have. Keeping in mind the drought types defined by Rassmussen (1993), it is important that the interval for the SPI matches the type of drought and consequently relates to the impacts of any rainfall shortage. Additionally, the temporal scale used to define the SPI for a chosen time interval may not reflect extreme SPI values for other time intervals, thus hiding an extreme event.

McKee, T.B., N.J. Doesken and J. Kleist (1993) set up a set of thresholds for classifying a drought according to SPI. SPIs ranging from zero to -0.99 were classified as "mild drought". If the values ranged from -1.0 to -1.49 were classified as a "moderate drought". SPIs from -1.5 to -1.99 were indicative of "severe drought" conditions. Finally, all SPI less than -2.0 were classified as extreme drought conditions. These categories are very broad and may not be applicable in every instance, but for the most part they provide a good framework for the SPI and relate it to terms that people can understand.

$$SPI \leq -2.0 \ldots \text{extreme drought}$$

$$-1.99 < SPI \leq -1.5 \ldots \text{severe drought}$$

$$-1.49 < SPI \leq -1.0 \ldots \text{moderate drought}$$

$$-0.99 < SPI \leq 0 \ldots \text{mild drought}$$

Utilizing the SPI to understand the intensity of precipitation events for different areas does eliminate some of the need for an intimate understanding of precipitation regimes at individual location. However, it is still important to understand the continental precipitation patterns throughout the season. Knowing the approximate location of the ITCZ during the time period of interest and general rainy seasons will help determine the critical nature of an

extreme SPI amount. For example, on the fringes of the ITCZ an extreme SPI value may be closely related to an early/late latitudinal procession of the ITCZ during a time when rainfall is typically sporadic in these areas. That is not to say that this rainfall is not important or should be ignored, merely that it is not the heart of the rainfall season in these locations, and therefore there is likely less dependence on precipitation during this period for the well-being of the people. As a method for analysis of precipitation over an entire continent with varied regimes and seasonal characteristics the SPI proves to be extremely valuable.

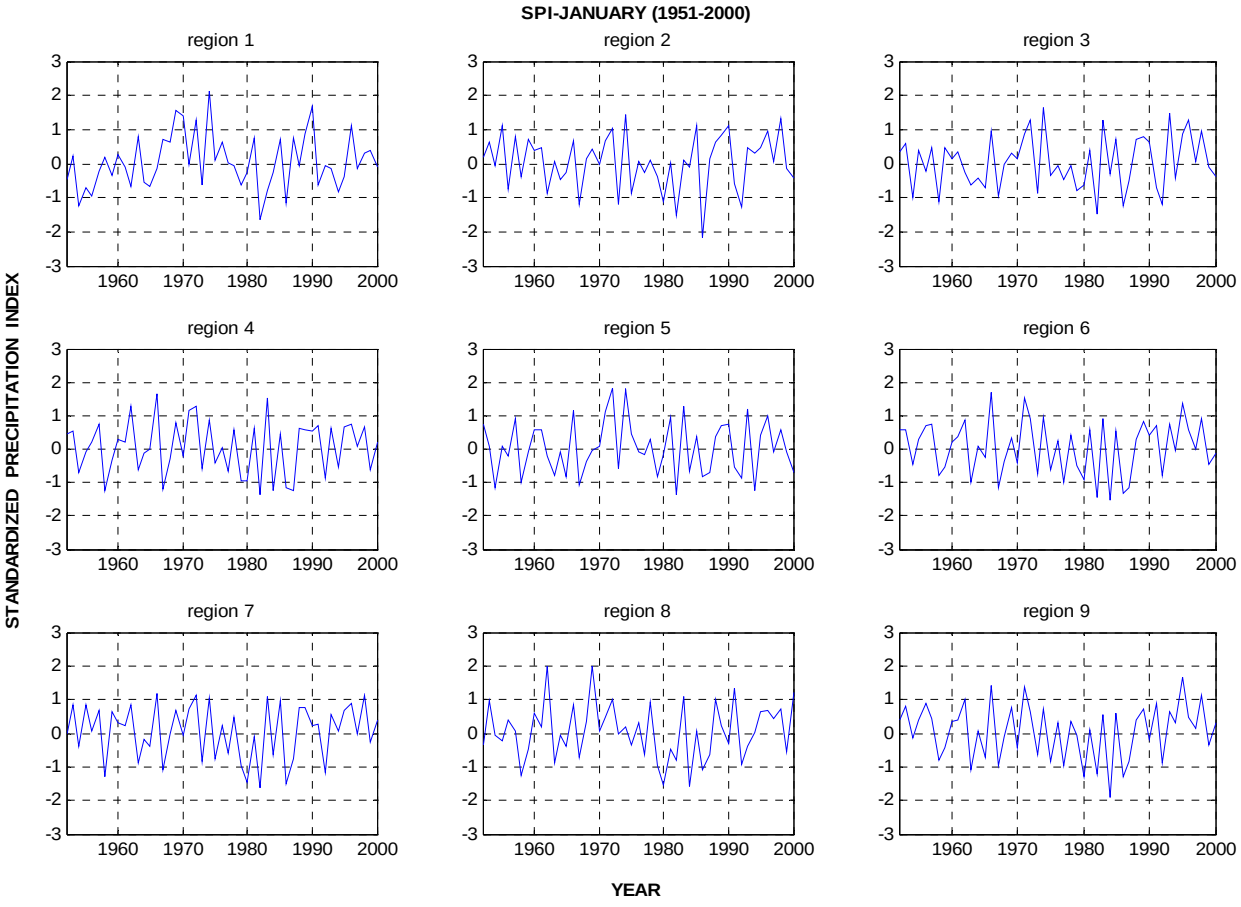

Figure 65: A plot of January SPI values is shown for 9 different regions in Madagascar.

Areas such as that plotted in Fig.65 have a more transient precipitation pattern in which the factors contributing to storm enhancement or suppression change frequently. One characteristic of the above subplots is that there appear to be balance between positive values and negative values in the subsets.

However, there are a number of reasons that a subset of SPI would not have a distribution close to normal that corresponds to the SPI value between 1 and -1. The physical dynamics at a particular location will vary, but low-frequency oscillations in sea-surface temperature and atmospheric gradients may offset the SPI for sequential subsets of the time-series. Subsets of the SPI that exhibit this type of shift probably reflect a time period in which there were precipitation-related hazards. In addition to low-frequency oscillations in physical controls, there may be even longer-term trends in the data related to a number of factors ranging from human-related modifications to the land surface, to changes in the composition of the atmosphere. These trends in the data would reflect the land/atmosphere interaction and how deforestation, desertification, increased carbon dioxide or global warming may affect precipitation. How and if changes such as these affect the precipitation in location specific, but a change in precipitation based on these factors may result in a trend in the data that will only be apparent by analysis of the entire time-series.

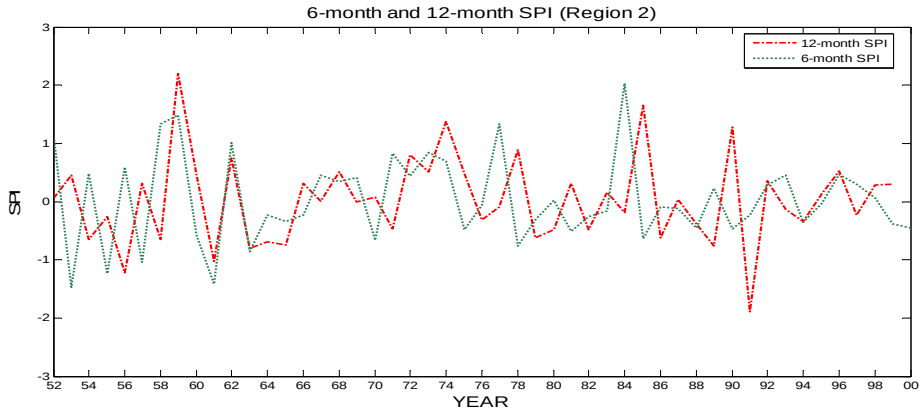

Figure 66: Plot of the seasonal SPI (Nov-Apr) and the12-year SPI (Jan-Dec) of the region 2.

A plot of the seasonal or six-month SPI (Nov-Apr) for the 12-year (Jan-Dec) SPI subset (Fig. 66, 67) exposes that region 2 and 3 are showing significant feature. Some differences appear from the subset of the SPI for the two time-series six-month dataset with one-year values. Although there is year overlapping during the rainy season, the two time series are in general quite close during the five decades.

The very noticeable divergence appears in 1991 from these figures when a series of six-month values near zero results in negative values in the 12-month data. It is known that this year represent the dry season in most region of southern Africa and still put its signature more precisely in the north western Madagascar based on the 12-month SPI subset. This dry event during 1991 is also supported by the non occurrence of storm hitting directly Madagascar which is one of the important rainfall contributors in that area especially the region 2 and 3.

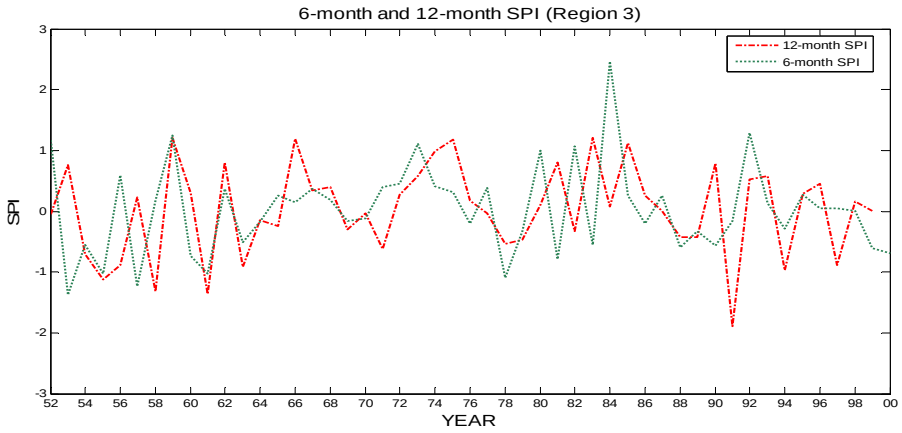

Figure 67: Plot of the seasonal SPI (Nov-Apr) and the 12-year SPI(Jan-Dec) of the region 3.

However, the multi-month SPI values may miss some short-term events, but capture severity at a scale where the influence of single events is less influential. Analysis at this multi-month scale may be especially applicable to drought, which has repercussions at a long time-scale, while flooding is usually seen as a result of quick but extreme precipitation. For instance, Fig.67 displays from the 12-month SPI that there was flood hitting mostly the north western region of Madagascar in 1959.

1.5 Conclusion

Drought can be characterized into three major types related to the duration of the event (Rasmussen et al., 1993). Short-term or meteorological drought is typically on the order of days or weeks. Agricultural drought involves a water shortage lasting from a few weeks to a

few months during the growing season, indicating that agriculture will be adversely affected by the water shortage. Finally, hydrological drought is a seasonal event that indicates a shortfall which will adversely affect the volume of water storage or flow (Wilhite, 2000). Analysis of SPI for different durations will determine the type of drought an area is experiencing.

The temporal invariance of the SPI allows for the significance of short-term and long-term precipitation events to be captured using the same methodology. The SPI allows for the simultaneous display of events at multiple scales. This is an important feature given that it is possible to experience drought conditions for one time-scale while experiencing wet conditions for another. It is this temporal invariance, the ability to measure rainfall at multiple timescales with the same method that makes the SPI such a versatile tool for reporting precipitation conditions. Additionally, a user with even a minimal understanding of the SPI can analyze values and determine the significance of rainfall for multiple time-scales.

As an example, it may be possible to have dry conditions when analyzed at an annual period, but experience flooding in the short term. The effects of the long-term drought may mean that reservoir levels are below average and water supplies may have to be rationed. Conversely, the effects of the short-term flood may mean that crops have been washed away, waterborne disease may be rampant, and people's lives may be at risk due to areas being underwater. For these reasons it is necessary to monitor precipitation conditions at a variety of time scales. Hence, it is shown that SPI is a powerful tool for this purpose. Remarkably, the famous scenario of drought in 1991 is revealed by the 12-month time scale of SPI in this study. The other extreme events could be emphasized just by modifying the time scale because climate phenomena having their different characters can produce heavy precipitation recorded in the area of study.

Chapter 2: Generalized extreme value and generalized Pareto distribution

2.1. Introduction

One of the most important statistical disciplines for the applied science over the last six decades is the extreme value theory. Because of its large applicability in different fields of study, extreme value techniques are widely used. Application of extreme value modeling has been published in ocean wave modeling (Dawson, T.H., 2000); wind engineering (Harris, R.I., 2001); thermodynamics of earthquakes (Launda & Cipollone, 2000); assessment of meteorological change (Thomson et al., 2001). Extreme value is also a powerful and yet fairly robust framework on rainfall climatology study which is one of the main objective of this research. Specifically, the aim of this chapter is to study the estimation not only of the quantile of Madagascar rainfall record but also its tails and risk measures using the extreme value theory. Another important issue of this study is the return level of the excess of the precipitation record in order to extract the main temporal pattern of severe rain which occurred in Madagascar.

So in the following section, we present a review and summarize of the extreme value theory, relevant to climate change studies, in terms of precipitation. Further insight is gained by implementing the monthly regional rainfall of Madagascar data recorded in a period of 50 years into the appropriate model reformulated in this review with respect of the goal of this chapter. It turns out that we can establish our data analysis within the framework of 'EVIM'. EVIM is a Software Package for Extreme Value Analysis in MATLAB (Ramazan Gençay, Faruk Selçuk, Abdurrahman Ulugülyağc, 2001).

2.2. Data

As stated previously, in this analysis we still make use of the VASCLIMO dataset which is a New Monthly Precipitation Climatology for the Global Land Areas for the Period 1951 to 2000 (Beck & Rudulf, 2004) with a spatial resolution of 0.5^o x 0.5^o. It is available in http://www.dwd.de/en/FundE/Klima/KLIS/int/GPCC/Projects/VASClimO/VASClimO.htm website. Furthermore, one purpose of this choice is to avoid the problem of bias between the dataset used to establish the distribution parameters and that used as observations. Similarly, we consider nine regions with respect not only to physical aspect of the key area but also to the correlation among the precipitation data.

2.3. Method of analysis

a) Fisher & Tippet theorem

The normal distribution is the important limiting distribution for sample sums or averages as summarized in a central limit theorem. Similarly, the family of extreme value distributions is the one to study the limiting distributions of the sample maxima. This family can be presented under a single parameterization known as the generalized extreme value distribution (GEV). The theorem of (Fisher & Tippett, 1928) is the core of the extreme value theory. The theory deals with the convergence of maxima. Suppose that $x_1, x_2, \ldots, x_m$ is a sequence of independently and identically distributed random variables from an unknown distribution function $F(x)$ where $x \sim (\mu, \sigma^2)$ and m is the sample size. Denote the maximum of the first $n<m$ observations of x by $M_n = max(x_1, x_2, \ldots, x_n)$. Given a sequence of $a_n > 0$ and b_n such that $(M_n - b_n)/a_n$, the sequence of normalized maxima converges in the following GEV distribution

$$H(x) = \exp\left[-\left(1 + \xi \frac{x}{\beta}\right)^{-1/\xi}\right] \quad \text{if} \quad \xi \neq 0, \quad (35)$$

$H(x) = \exp [- \exp (-\frac{x}{\beta})]$ if $\xi = 0$ (36)

where $\beta > 0$ and x is such that $1 + \xi x > 0$ and ξ is the shape parameter. When $\xi > 0$, the distribution is known as the Fréchet distribution and it has a fat-tail. The larger the shape parameter, the more fat-tailed the distribution. If $\xi < 0$, the distribution is known as the Weibull distribution. Finally, if $\xi = 0$, it is the Gumbel distribution. The Fisher-Tippett theorem suggests that the asymptotic distribution of the maxima belongs to one of the three distributions above, regardless of the original distribution of the observed data. Therefore, the tail behavior of the data series can be estimated from one of these three distributions.

The class of distributions of $F(x)$ where the Fisher-Tippett theorem holds is quite large. One of the conditions is that $F(x)$ has to be in the domain of attraction for the Fréchet distribution ($\xi > 0$) which in general holds for the precipitation time series. Gnedenko, B.K. (1943) showed that if the tail of $F(x)$ decays like a power function, then it is in the domain of attraction for the Fréchet distribution. The class of distributions whose tails decay like a power function are large and include the Pareto, Cauchy, Student-*t* and mixture distributions. These distributions are the well-known heavy tailed distributions. The distributions in the domain of attraction of the Weibull distribution ($\xi < 0$) are the short tailed distributions such as uniform and beta distributions which do not have much power in explaining rainfall time series. The distributions in the domain of attraction of the Gumbel distribution ($\xi = 0$) include the normal, exponential, gamma and lognormal distributions where only the lognormal distribution has a moderately heavy tail.

b) Generalized Pareto Distribution

In general, we are not only interested in the maxima of observations, but also in the behaviour of large observations which exceed a high threshold. Given a high threshold *u*, the distribution of excess values of *x* over threshold *u* is defined by the following theorem (1)

$$F_u(y) = \Pr\{X - u \le x / X > u\} = \frac{F(y+u) - F(u)}{F(u)} \quad (1)$$

which represents the probability that the value of *x* exceeds the threshold *u* by at most an amount *y*. A theorem by Balkema and de Haan (1974) and Pickands (1975) shows that for sufficiently high threshold *u*, the distribution function of the excess may be approximated by the Generalized Pareto Distribution (GPD) such that, as the threshold gets large, the excess distribution *F(u*(*y*)) converges to the GPD which is

$$G(x) = 1-(1 +\xi\frac{x}{\beta})^{-1/\xi}] \quad \text{if} \quad \xi \neq 0 \quad (37) \text{ and}$$

$$G(x) = 1- \exp(-\frac{x}{\beta}) \text{ if} \quad \xi = 0 \qquad (38)$$

where ξ is the shape parameter. The GPD embeds a number of other distributions. When $\xi > 0$, it takes the form of the ordinary Pareto distribution. This particular case is the most relevant for financial time series analysis since it is a heavy tailed one. For instance, the GPD has an infinite variance for $\xi = 0.5$ and, when $\xi = 0.25$, it has an infinite fourth moment. For the security returns or high frequency foreign exchange returns, the estimates of ξ are usually less than 0.5, implying that the returns have finite variance (Jansen and deVries 1991, Longin 1996, Müller et al. 1996, and Dacorogna et al. 2001b). When $\xi = 0$, the GPD corresponds to exponential distribution and it is known as a Pareto II type distribution for $\xi < 0$. The importance of the Balkema and de Haan (1974) and (Pickands, J. , 1975) results is that the distribution of excesses may be approximated by the GPD by choosing ξ and β and setting a high threshold *u*. The GPD can be estimated with various methods such as the method of probability weighted moments or the maximum likelihood method. For $\xi > -0.5$ which

corresponds to heavy tails, Hosking and Wallis (1987) present evidence that maximum likelihood regularity conditions are fulfilled and the maximum likelihood estimates are asymptotically normally distributed. Therefore, the approximate standard errors for the estimators of β and ξ can be obtained through maximum likelihood estimation.

c) Modeling threshold excesses

c-1) Threshold selection

The theorem (1) suggests the following framework for the extreme value modelling. The raw data consist of a sequence of independent and identically distributed measurements x1,…,xn. Extreme events are identified by defining a high threshold u, for which the exceedences are $\{x_i : x_i>u\}$. Label these exceedences by x(1),…,x(k), and define threshold excesses by y_i=x(j)-u, for j=1,…,k. By theorem (1), the y_i may be regarded as independent realizations of a random variable whose distribution can be approximated by a member of the generalized Pareto family.

In general, data analysis with such model is performed in two steps. In the first one, the threshold, u, is chosen graphically looking at the mean excess plot (see Embrechts et al., 1997) or simply setting it as some high percentile of the data (see DuMouchel, 1983). Then, assuming that u is known, the other parameters are estimated, as suggested, for instance, in Smith (1987). The main drawback of this idea is that only the observations above the threshold are used in the second step. Moreover, the threshold selection is by no means an easy task as observed by David and Smith (1990) and Coles & Twan (1994). If, on the one hand, a considerably high threshold is chosen in order to reduce the model bias, on the other hand, this would consequently imply that only a few observations are used for estimating β and ξ, thus increasing the variances of the estimates.

There is uncertainty in the choice of the threshold, *u*, even in the traditional theory to select it because it implies a balance between bias and variance. In this case, too low a threshold is likely to violate the asymptotic basis of the model, leading to bias; too high a threshold will generate few excesses with which the model can be estimated, leading to high variance. The standard practice is to adopt as low a threshold as possible, subject to the limit model providing a reasonable approximation. Two methods are available for this purpose: one is exploratory technique carried out prior to model estimation; the other is an assessment of the stability parameter estimates, based on the fitting of models across a range of different thresholds.

In more details, the first method is based on the mean excess of the sample defined by the equation: $$e_n(u) = \frac{\sum_{i=1}^{n}(X_i - u)}{\sum_{i=1}^{n} 1_{\{X_i > u\}}} \qquad (39)$$

which is the sum of the excesses over the threshold *u* divided by the number of data points which exceed the threshold *u*. It is an estimate of the mean excess which describes the expected overshoot of a threshold once an exceedance occurs. If the empirical mean excess is a positively sloped straight line above a certain threshold *u*, it is an indication that the data follows the GPD with a positive shape parameter ξ. On the other hand, exponentially distributed data would show a horizontal mean excess while short tailed data would have a negatively sloped line. Admittedly, the interpretation of a mean excess plot against threshold is not always simple in practice.

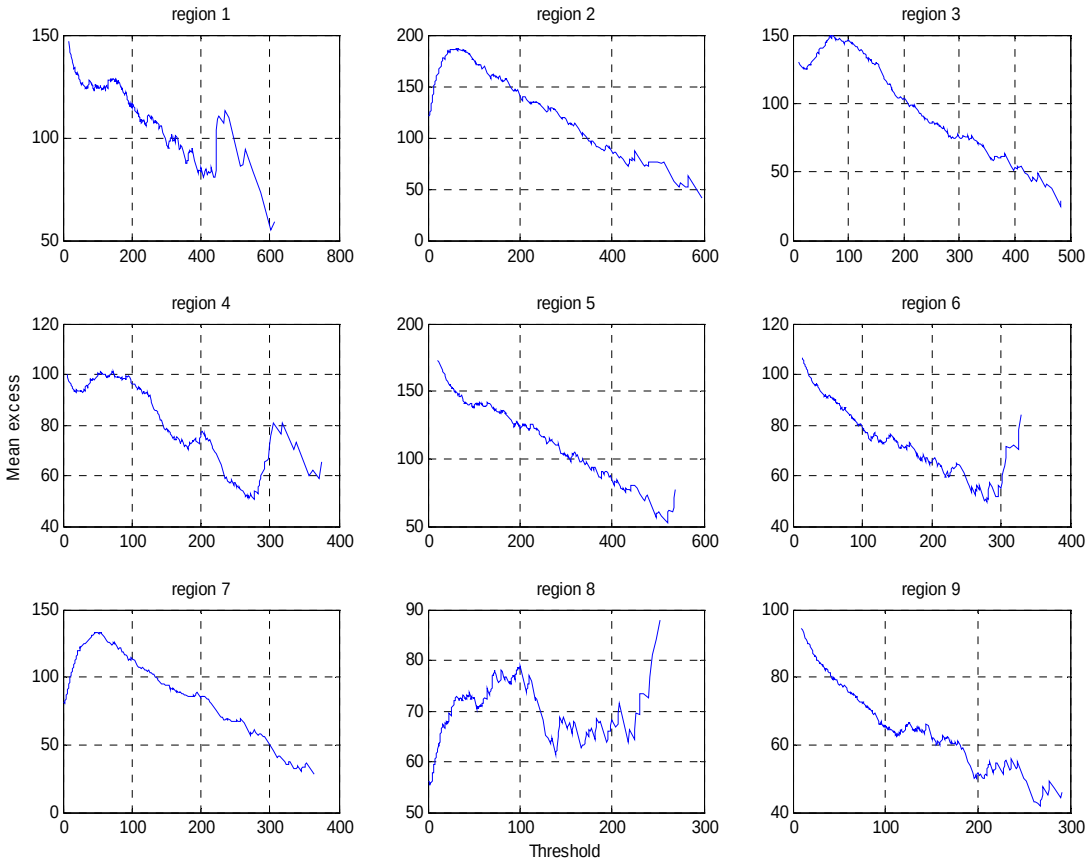

Figure 68: Example of mean excesses plots against threshold

Fig. 68 shows the mean excess plot of the monthly rainfall data in which the first graph illustration the region 1 appears to fluctuate negatively from u=0 to $u \approx$ 182, then it continues fluctuating until $u \approx$ 440 beyond which it is approximately linear until $u \approx$ 470, whereupon its decays sharply. It is tempting to conclude that there is no stability until $u \approx$ 470, after which there is approximate linearity. This suggest that we take u=470. However, there are just 11 exceedences of the threshold u=470, too few to make meaningful inferences. Moreover, the information in the plot for large values of u is unreliable due to the limited amount of data. Accordingly, it is probably better to conclude that there is some evidence for linearity above u=182, and to work initially with a threshold set at u=182. For the other regions, we process on the same way.

(Hill, 1975) introduced the second tool in threshold determination in which he proposed the following estimator for ξ, $\hat{\xi} = \frac{1}{k-1}\sum_{i=1}^{k=1} \ln X_{i,N} - \ln X_{k,N}$ for k≥2 (40)

where k is upper order statistics (the number of exceedances), N is the sample size, and $\alpha = 1/\xi$ is the tail index. A Hill-plot is constructed such that estimated ξ is plotted as a function of either k upper order statistics or of the threshold. A threshold is selected from the plot where the shape parameter ξ is fairly stable.

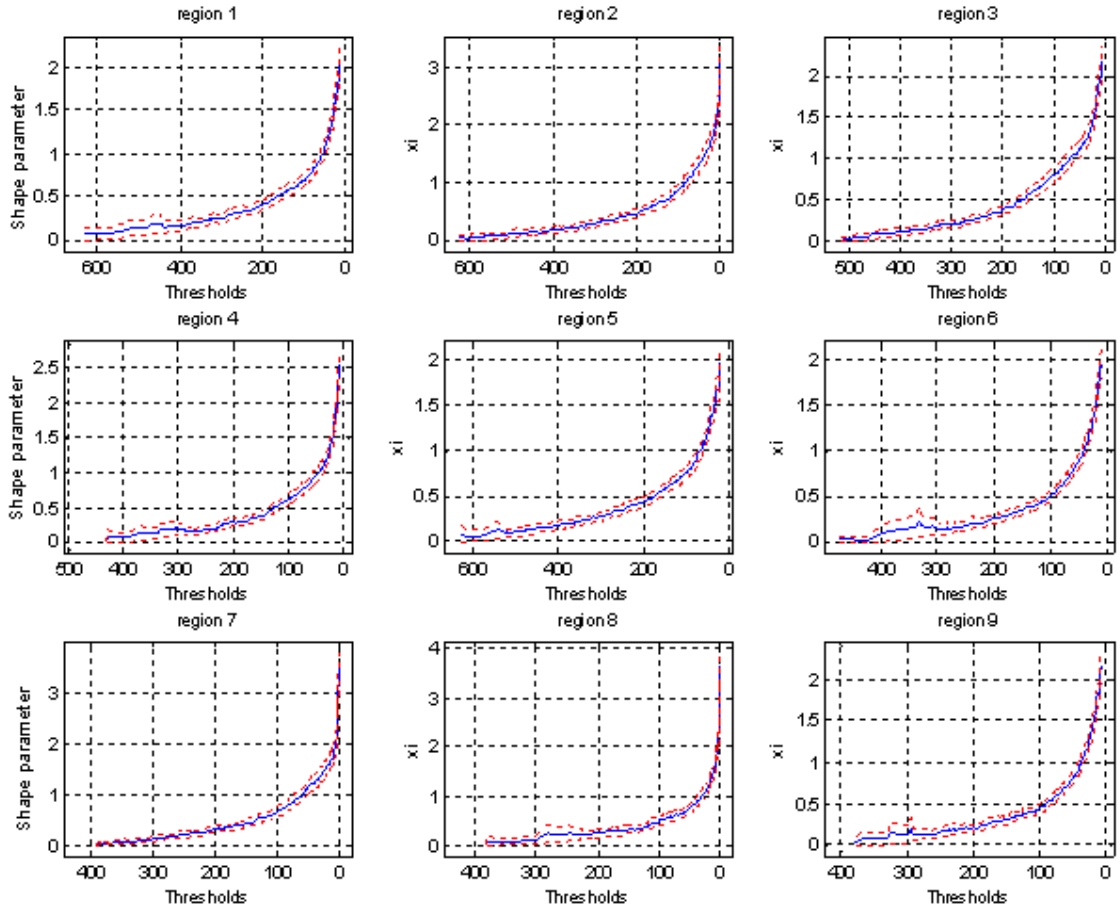

Figure 69: Hill estimate plots of the tail index against different threshold

Apparently, the graph of region 1 in Fig. 69 shows the change in pattern for very high thresholds that was observed in the mean excess plots. Hence, the selected threshold of u=182 appears reasonable.

c-2) Parameter estimation

Having determined the threshold, the parameters of the generalized Pareto distribution can be estimated by maximum likelihood. Suppose that the values $x_1,\ldots,y_k$ are the k excesses of a threshold u, for $\xi \neq 0$ the log likelihood is derived from (37) as

$$\ell(\beta,\xi) = -k\log\beta - (1+1/\xi)\sum_{i=1}^{k}\log(1+\xi x_i/\beta) \quad (41),$$

provided that $(1+\beta^{-1}\xi x_i) > 0$ for i=1,…, k; otherwise, $\ell(\beta,\xi) = -\infty$ (42).

In the case ξ=0, the log likelihood is obtained from (38) as $\ell(\beta) = -k\log\beta - \beta^{-1}\sum_{i=1}^{k} x_i$ (43).

Analytical maximization of the log-likelihood is not possible, so numerical techniques are again required to avoid numerical instabilities when $\xi \approx 0$, and ensuring that the algorithm does not fail due to evaluation outside of the allowable parameter space. Standard errors and confidence intervals for the generalized Pareto distribution are obtained in the usual way from standard likelihood theory.

c-3) The Tail Estimation

In statistics, a QQ-plot (quantile-quantile plot) is a convenient visual tool to examine whether a sample comes from a specific distribution. Specifically, the quantiles of an empirical distribution are plotted against the quantiles of a hypothesized distribution. If the sample comes from the hypothesized distribution, the QQ-plot is linear. In the extreme value theory

and applications, the QQ-plot is typically plotted against the exponential distribution (i.e, a distribution with a medium-sized tail) to measure the fat-tailness of a distribution. If the data is from an exponential distribution, the points on the graph would lie along a straight line. If

there is a concave presence, this would indicate a fat-tailed distribution (see Fig. 70), whereas a convex departure is an indication of short-tailed distribution.

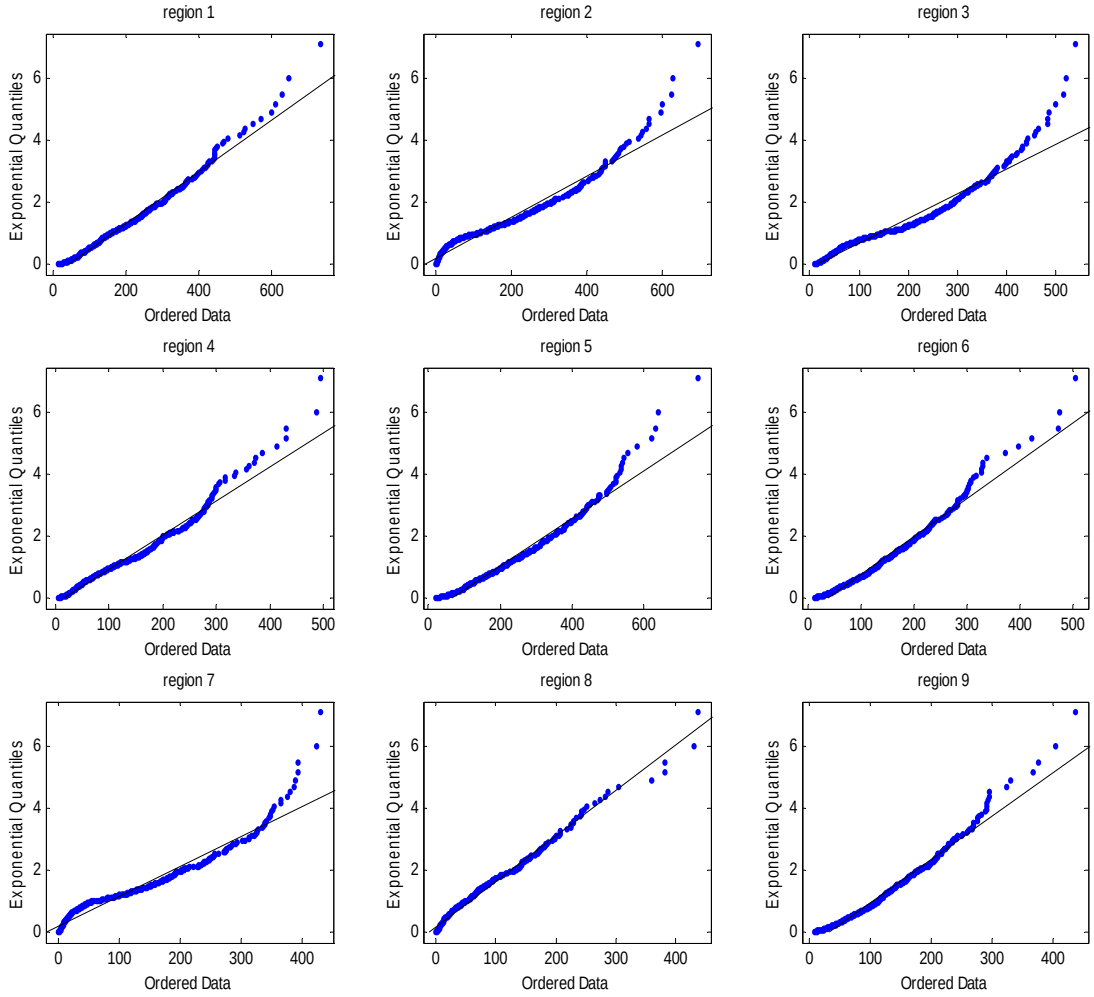

Figure 70: QQ-plot for data against exponential distribution without excluding any point.

The data points in the tail ($x \geq u$) are represented by:

$$F(x) = \Pr\{X \leq x\} = (1 - \Pr\{X \leq u\})F_u(x-u) + \Pr\{X \leq u\} \quad (44).$$

For large u, we can estimate $F_u(x-u)$ by $G(x-u)$. Also $\Pr\{X \leq u\}$ can be estimated from the data by $F_n(u)$. Therefore, the tail estimate is $\hat{F}(x) = (1-F_n(u))G(x) + F_n(u)$ (45)

which approximates the distribution of $F(x)$. It can be shown that $\hat{F}(x)$ is GPD which has the same shape parameter value (ξ) of $F(x)$. Given a threshold u, an estimate of $F_n(u)$ may be obtained as $(n - N_u)/n$ where n is the sample size and N_u is the number of exceedances. The tail estimator, therefore, is calculated by $\hat{F}(x) = 1 - \frac{N_u}{n}\left(1 + \hat{\xi}\frac{x-u}{\hat{\beta}}\right)^{-1/\hat{\xi}}$ (46).

For a given probability $q > F(q)$, a percentile $(\hat{x}_q)$ at the tail is estimated by inverting the tail estimator in Equation 46, $\hat{x}_q = u + \frac{\hat{\beta}}{\hat{\xi}}\left(\left(\frac{n}{N_u}(1-q)\right)^{-\hat{\xi}} - 1\right)$ (47).

In statistics, this is the quantile estimation and it is the Value-at-Risk (VaR) in the finance literature.

d) Return Levels

In common terminology, $\hat{x}_q$ is the return level associated with the return period N=1/(1-q) (48).

Since to a reasonable degree of accuracy, the level $\hat{x}_q$ is expected to be exceeded on average once every N years. Plotting $\hat{x}_q$ against q on logarithmic scale produces the same qualitative features as return level plots based on the GEV model: linearity if ξ=0; concavity if ξ>0 ; convexity if ξ<0. However, for presentation it is often more convenient to give return levels on annual scale, so that the N-year return level is the level expected to be exceeded once every N years.

2.4. Discussions and results

Before stating any results, choosing the thresholds of each regional rainfall data is relevant. Therefore, a careful combination of the QQ-plot, the Hill-plot and the MEF should be

considered in order to define the threshold. Admittedly, we face a trade off between bias and variance in the threshold determination. If we choose a low threshold, the number of observations (exceedances) increases and the estimation becomes more precise. However, choosing a low threshold also introduces some observations from the center of the distribution and the estimation becomes biased. Anyway, the following table illustrates the threshold values implemented in the further model from which we fetch most of our results.

Table 4: Selected threshold per station

Region	*1*	*2*	*3*	*4*	*5*	*6*	*7*	*8*	*9*
Threshold (mm)	182.29	262.10	252.20	162.25	276	130.71	159	107.85	129.33

The determination of the thresholds indicates directly that we are dealing with GPD as a limiting distribution. Basically, the aims of this analysis is to estimate the parameters so that the tail and the return levels respectively can be estimated and calculated by the mean of the sample maximum value studies. Here, the flood case within a half century from 1951 until 2000 would be particularly considered. Although each monthly regional rainfall records in a period of 50 years constitutes sample of 600 cases, it would be restricted depending on the value of the threshold.

The approximation of the shape parameter is one of the issues that should be established if we want to assess the quantile. Indeed, estimation of return levels requires the substitution of parameters values by their estimates. Accordingly, better estimates of precision for shape parameters of each regional rainfall data are obtained from the following figures that illustrate the output results. Effectively, Fig. 71 shows how the shape parameter varies with exceedances; the dotted lines are upper and lower 95 % confidence intervals. Hence, it is possible to say that the increase of the exceedences implies decrease of the threshold. Fig. 72 shows that qualitative behaviour of the generalized Pareto distribution can be explained by the

shape parameter which generates the duality between the GEV and the generalized Pareto families. Similarly to the GEV, if ξ<0 the distribution of excesses has an upper bound of $u - \beta / \xi$ (or beta distribution); if ξ>0 the distribution has no upper limit, it is a heavy-tailed (or Pareto itself) distribution. The distribution is unbounded if ξ=0 or again light-tailed (or exponential) distribution. Furthermore, Smith (1985) studied this problem in detail and obtained the following results:

- When ξ >-0.5, maximum likelihood estimators are regular, in the sense of having the usual asymptotic properties;
- When -1< ξ <-0.5, maximum likelihood estimators are generally obtainable, but do not have the standard asymptotic properties;
- When ξ <-1, maximum likelihood estimators are unlikely to be obtainable.

The case $\xi \leq -0.5$ corresponds to distributions with a very short bounded upper tail. This situation is rarely encountered in applications of extreme value modeling, so the theoretical limitations of the maximum likelihood approach are usually no obstacle in practice. Indeed, this plot (Fig. 71) emphasizes that the estimations of ξ do not go under the value of -0.5 in general which means that the maximum likelihood estimates ($\hat{\beta}, \hat{\xi}$) are obtainable. It is also observed that there is change in pattern for very high thresholds with small perturbation implying the selected thresholds appear reasonable.

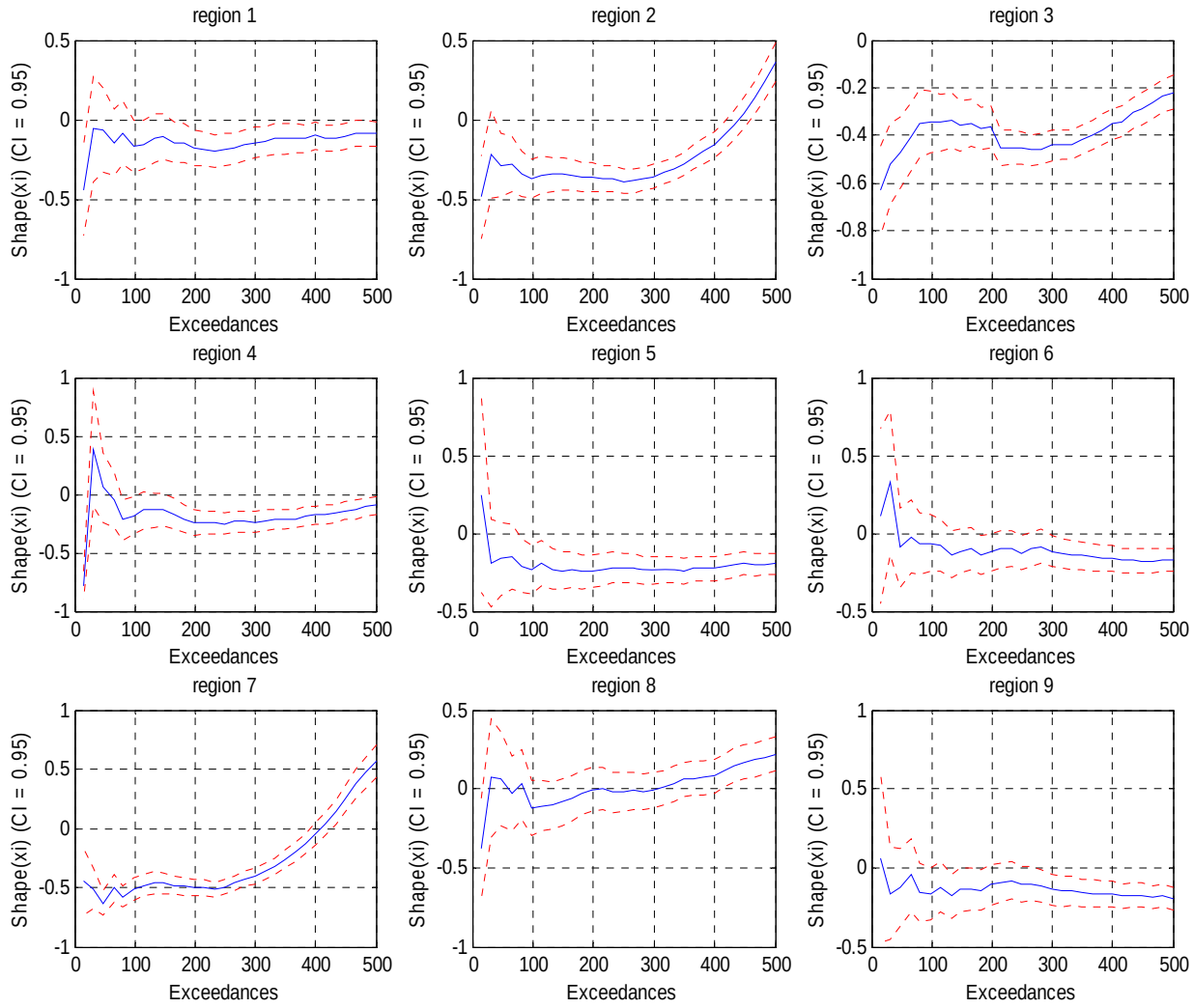

Figure 71: Estimates of shape parameter, ξ, at different number of exceedances for the nine regions.

For assessing the quality of a fitted generalized Pareto model, quantile plots, return level plots and density plots are useful. Assuming a threshold of *u* provided $\hat{\xi} \neq 0$, the quantile plots can be presented as shown in Fig.73. Definitely, it appears that quantile plots consists of points that are approximately linear which makes the generalized Pareto model plausible for modelling excesses of *u*. Again this linearity rises from the dependence of the scale

parameter β on the threshold u because like the GEV, a GP quantile is linear in β, but highly nonlinear in ξ.

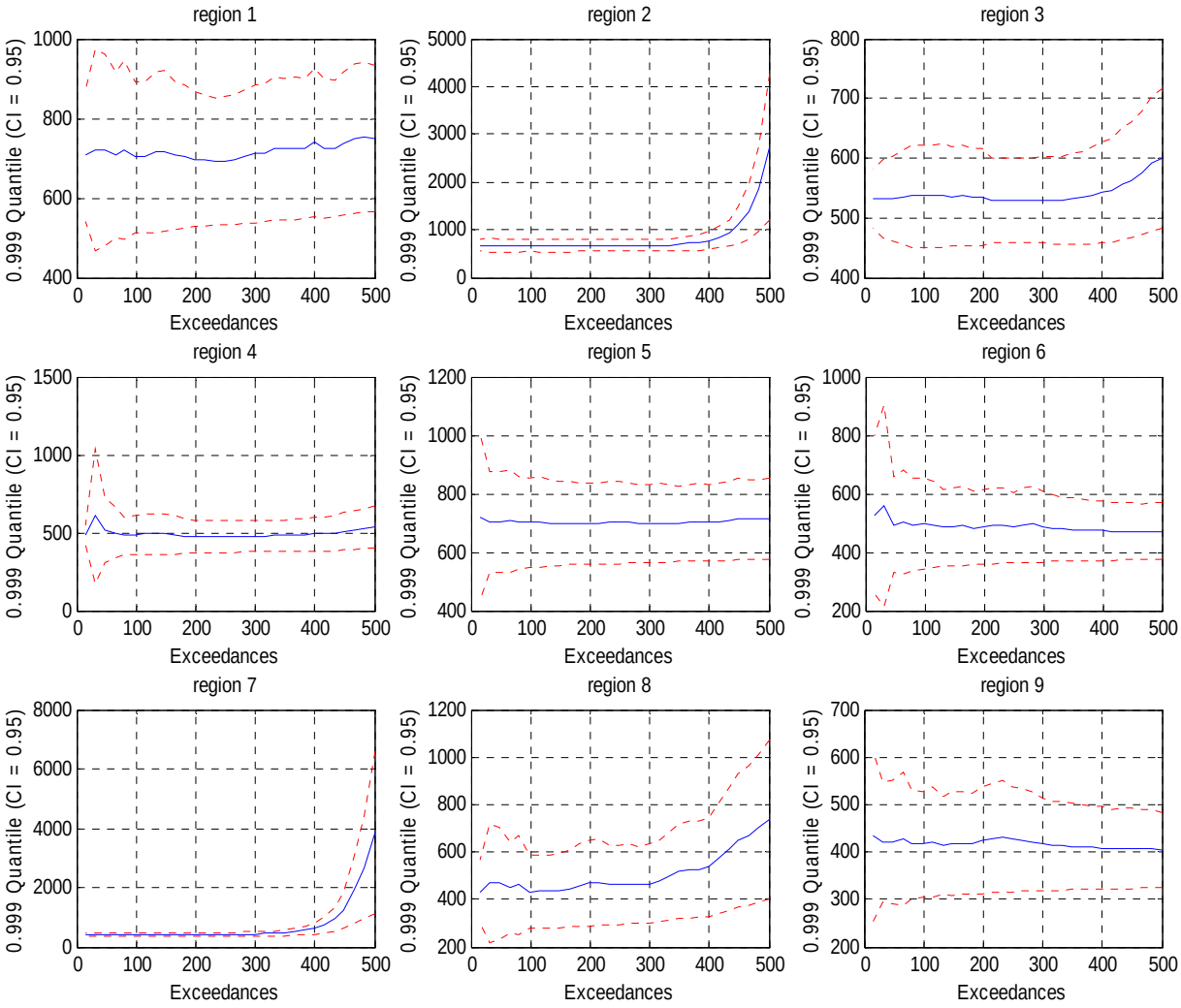

Figure 72: Regional rainfall data estimates of quantile 99.9 as a function of exceedances. Dotted lines are upper and lower 95 percent confidence intervals.

Yet, the tail probabilities could be estimated and essentially, the point estimate at the tail 0.999th quantile estimate at 95% confidence interval for the regional rainfall data could be yielded from it. As shown into the Fig. 73, horizontal dotted lines are estimated regional rainfall at 0.999th quantile (middle dotted line), lower confidence level (left dotted line) and

upper confidence level (right dotted line). In the first region, estimated value (694.5609), upper confidence band (1022.3454) and lower confidence band (635.3372) can be read at the upper *x*-axis. Both axes are on logarithmic scale because the data covers a large range of values so the logarithm reduces it to a more manageable range.

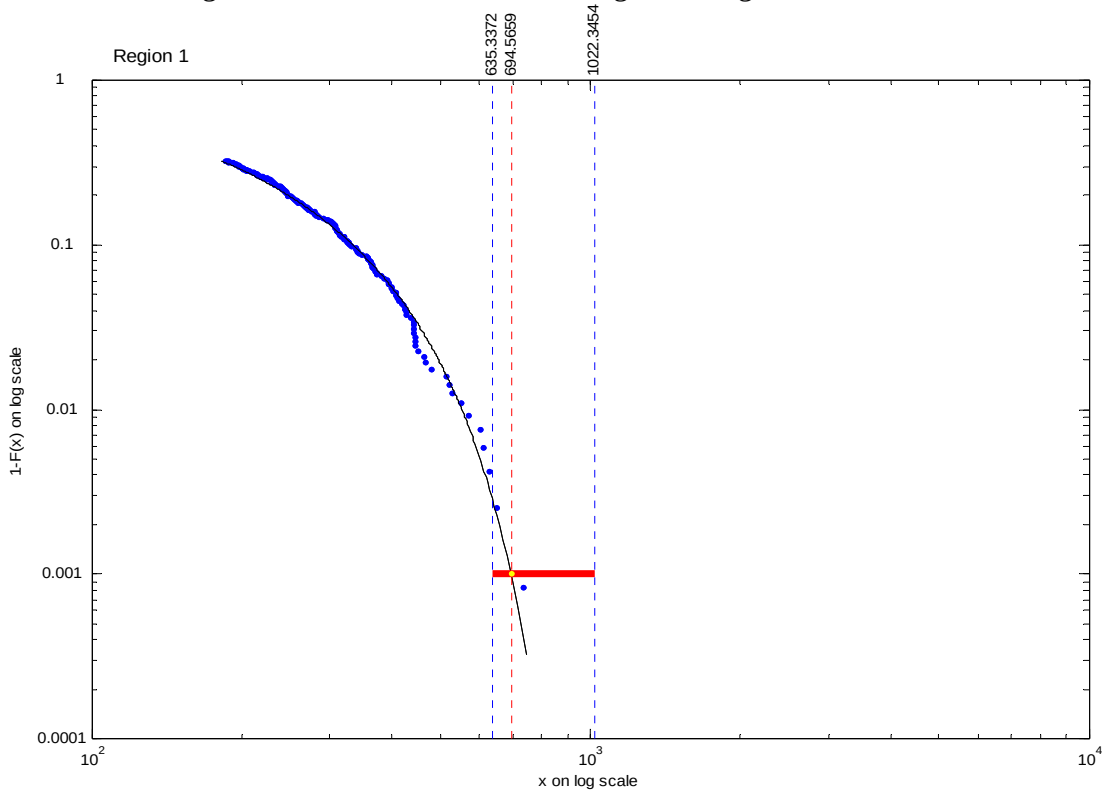

Figure 73: Point estimate at the tail 0.999th quantile estimate and 95 percent confidence interval of the region 1 rainfall data.

The following table resumes the results from the nine regions in which the study is done.

Table 5: Estimated value at the tail 0.999th quantile estimate at the lower and upper confidence band of each defined region.

Region	***Value at the lower confidence band***	***Estimated value at the 0.999th quantile***	***Value at the upper confidence band***	***Maximum value (mm)***

1	635.3372mm	694.5659 mm	1022.3454 mm	735
2	645.18 mm	669.8195 mm	1012.2502mm	694.10
3	510.8695 mm	537.0553 mm	771.5048mm	539.4
4	440.2054 mm	489.3432 mm	672.8549 mm	494.25
5	654.2474 mm	700.048 mm	817.1095mm	748
6	438.0812 mm	495.1139 mm	670.3673mm	504.43
7	609.8652 mm	424.6057 mm	643.125mm	428.75
8	376.071 mm	434.578 mm	605.4183 mm	435.75
9	377.5732 mm	419.0173 mm	553.8083mm	437.33

Compared with the maximum value of each regional time series, small differences have been observed which is normal because the maximum values are approximately defined by the maximum order of the quantile. Once the parameters are known, it also often of interest to compute the return levels. In fact, for a given return period (N-year) versus N-year return level for monthly rainfall, it is expected that there is an excess of level x_N every N-th observation. In other words, there is a 1/N probability to exceed the level x_N. Essentially, we have to be careful with the probability of an exceedance of the threshold. Relatively, we can use as an example the return level plot of region 6 of the Fig.74 to illustrate that for the recurrence interval N=100 , x_N is equal to 355, which means that we expect annual monthly maximum to exceed 355mm every 100 years. This approximation helps us also to figure out generally that within a period of 30 years (from N=0 to N=30), we can observe dramatic increase of the return level followed by remarkable gradual increase which characterize the extrapolation of the available period into a lager time-scale. Anyway, it shows that the time-scale of estimation is limited otherwise there is uncertainty of the value approximated that may damage the design of major structures.

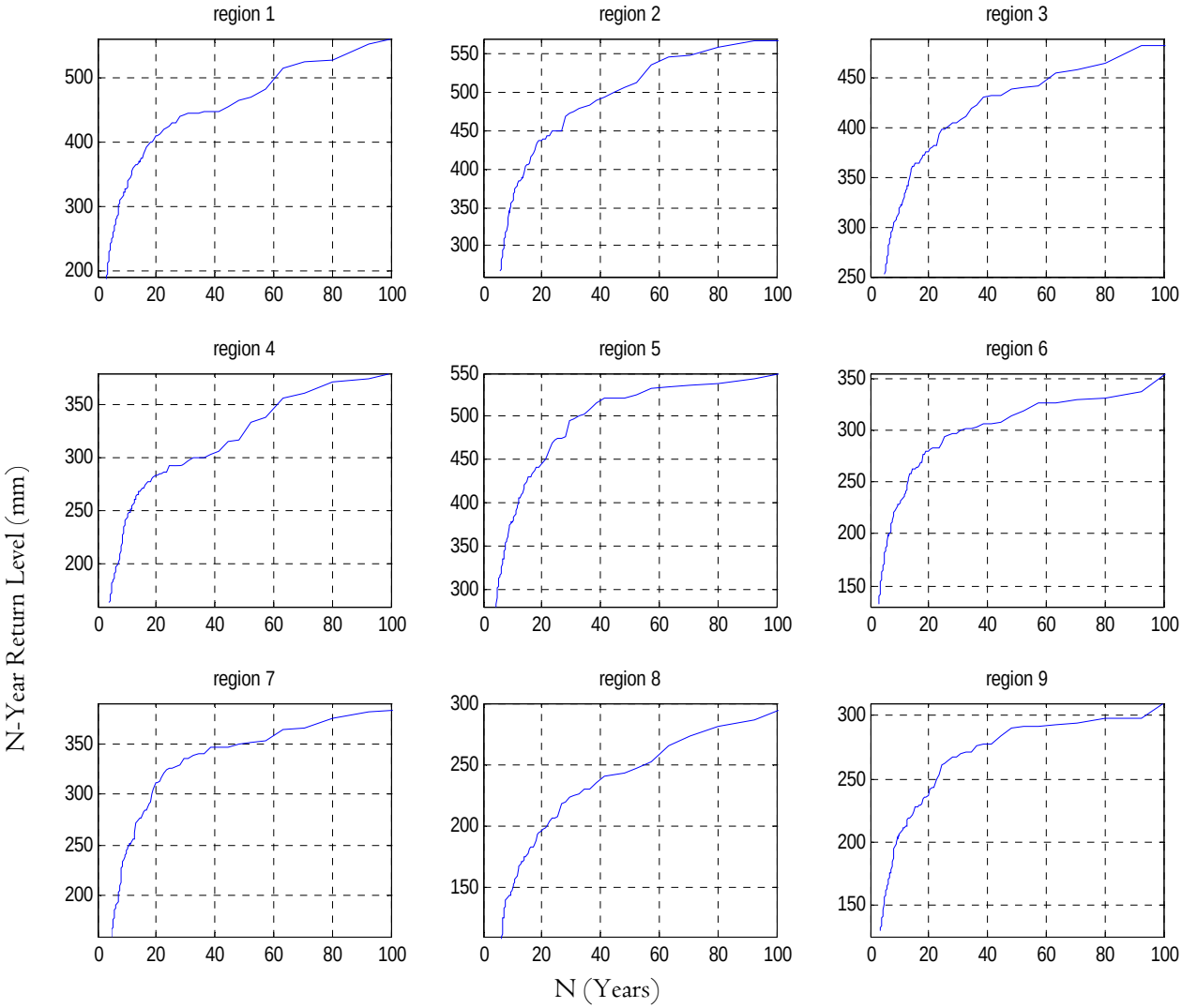

Figure 74: Return level plot for monthly rainfall time series for each region.

2.5. Conclusion

Some potential advantages of extreme value theory in modeling rainfall time series have been pointed out. The reliance on more conventional statistical methods can result in labeling regional precipitation over Madagascar as more "surprising" than they ought to be. Strong evidence of heavy tail distribution has been presented from the Q-Q plot although its origin is not quite identifiable because of the fluctuation due to the composition of different phenomenon prevailing around the area of study. Hopefully, it has been demonstrated from

our regional analysis how the statistics of exceedences can readily incorporate information about the accurate estimates of flood probabilities, exploiting the fact that some extreme parameters only gradually vary within a region. It is useful to use more data in order to have not only the approximation valid but the degree of uncertainty less. Furthermore, we have focused only on the temporal pattern in our treatment of extremes because in principle, fully spatial-temporal modeling is unrealistic as well as its applications so far are rather limited. However, the main advantage of this study is the establishment of the return period of the very huge amount of rainfall that occurs in different region of Madagascar. Moreover, it seems to play an important role to the extreme events prediction for different purposes such as allegation of many sorts of damage.

Part IV: Dynamics of Southern region rainfall

Summary

Atmospheric dynamics for dry episodes over southern Madagascar is studied using dynamical variable data from the National Centre for Environmental Prediction (NCEP) available at 2.5^{o} resolution for the period 1948 until present. The outset of this analysis is the identification of Madagascar region and its characteristics based on the rainfall gridded data provided by Vasclimo from 1951 to 2000 with resolution 0.5^{o}x0.5^{o}.

From the composite analysis of the major dynamical variables such as wind vector, Omega, OLR, specific humidity, prominent mechanisms are uncovered in different aspects explaining that southern Madagascar is a prone area of dryness.

Despite that Madagascar southern region is currently fragilized by the lack of rainfall, a skilful forecast is developed based on month-lead prediction models. Climate data from NCEP is analysed and used to identify the key predictors that makes the predictability possible. Teleconnection of the southern rainfall with the Pacific Ocean through the sea surface temperature is found. On the other hand, significant relationship is also analysed between the OLR and the target variable during the break phase of the monsoon whether in the Atlantic Ocean or in the Indian Ocean. Those strategic areas apparently contribute to the rainfall forecast that tends to be in gradual increase within 50 years climatology more precisely from 1951 to 2000.

Chapter1: Atmospheric dynamics for dry episodes over Southern Madagascar

1. Introduction

The rainwater constitutes a crucial natural resource for Madagascar. Although it is unevenly distributed, some regions are extremely 'fragilized' by the cyclone passage that provokes important floods. Hence, serious damage in different aspects had been recorded for example in 1970, 1977, 1984, 1994, 1998. Some areas are recurrently hit by the drought primarily the southern part of the country but it seems periodic in the other regions. In fact, the extreme South of the island is a semi-arid area where the annual average of precipitations is lower than 600 mm with deficiency in water from 9 to 11 months. So, whatever classification adopted and criteria employed, the south remains as the driest region (Doncques, 1975). Certain authors consider that this area does not form part of the tropical field, asserting the fact that the winter temperatures of oceanic surface observed are lower than 18°C (McGregor and Nieuwolt, 1998). Hopefully, improving knowledge on dry or wet events is an action that can be taken to mitigate the risk and economic consequences caused by the climate extremes.

Therefore, this present study devotes considerable space to the dynamics atmospheric of dry events over the southern part of Madagascar which was not previously considered.

The objective of this paper therefore is to understand meteorological patterns and perturbations that would have an impact and modulate the occurrence of drought over southern part climate during the extreme summer season. The mechanisms which would induce drought are analysed through composites analysis tools. Therefore, the paper is

organized as follows, section 2 introduces the datasets. The methods used in the study are discussed briefly in section 3. The results are presented in section 4 followed by the conclusion in section 5.

1.2. Data

a) Precipitation data ***(c.f. Part II, chap1, §1.2, a)***

b) Meteorological data

We employ different atmospheric reanalysed data to highlight the features of the atmospheric circulations during drought period in the summer season over the southern part of Madagascar. This dataset consists of a reanalysis of the global observational network of meteorological variables (wind, temperature, geopotential height, humidity on pressure levels, surface variables and flux variable like precipitation rate) and reported on a 2.5^{o}x2.5^{o} grid every 6 h (0000, 0600, 1200, 1800 UTC), on 17 pressure levels from 1000 to 10hPa, which are good resolutions for studying synoptic weather systems.

Furthermore, we also make use of Outgoing Longwave Radiation (OLR) derived from satellite. Launching polar orbital National Oceanic and Atmospheric Administration (NOAA) Television Infrared Observation Satellite (TIROS) satellites has made it possible to establish measures of outgoing longwave radiation (OLR) at the top of the atmosphere and at a resolution of 2.5^{o} latitude-longitude (Gruber and Krueger). The OLR unit is W/m². The NCEP re-analysis system assimilates all archived data from 1948 to the present via a numerical model. The details of NCEP reanalysis can be found in (Kalnay et al., 1996) and (Kistler, R., and Coauthors, 2000).

1.3. Methods

a) Pearson correlation

Concerning the precipitation data, significant correlation test is made with n-2 degree of freedom within t-distribution given by the equation $t = \frac{\bar{x} - \mu_o}{[\hat{Var}(\bar{x})]^{1/2}}$ (49)

where $\bar{x}$ the sample is mean of n values of dataset and μ_o is specified mean. The correlation map topography information precipitation regime of Madagascar is identified.

b) Atmospheric variables (c.f. Part II, Chap 1, §1.3, b)

c) Composite analysis

The seasonal (January –February) rainfall variability of southern Madagascar from 1951 to 2000 is used to identify the drought years as shown in Fig. 75. From the rainfall time series, the five driest years 1957, 1962, 1974, 1976, and 1983 were considered for composite analysis in order to find out the atmospheric mechanisms.

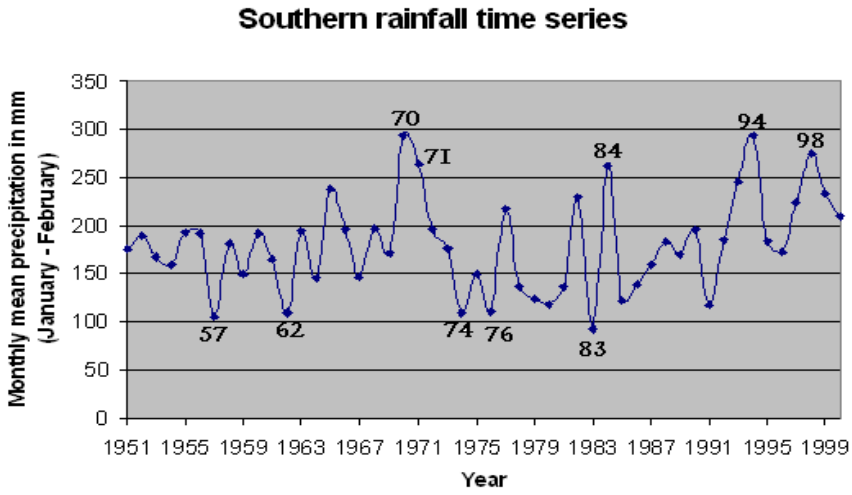

Figure 75: Southern Madagascar averaged rainfall time series from six stations during the rainy season depicting the extreme events (dry and wet years).

1.4. Results

a) Rainfall regimes

The correlation is not such a robust method by its own to define the regions that another technical aspect should be considered. Thus, correlation and topography are used to delineate the rainfall regime of Madagascar. As a matter of fact, Madagascar precipitation is strongly influenced by the relief. One can distinguish four areas with respect to the climate: the East coast, the West coast, the highland and the extreme South. However, any idea of regionalization rises from the nonsymmetrical physical aspect of Madagascar (Fig. 76) manifested in classifications.

a-1) The East coast

East coast is the most 'sprinkled' area of the island. It is under the influence of trade winds of South-East throughout the year. The interaction of the airflow and sharp peaks lying along the eastern coastal ultimately results strong precipitations in this area. This humid zone is even more significant during the austral summer since the low pressures associated with the Inter Tropical Convergence Zone coupled with the cyclones which develop in the North of the Island and brings supplementary rainfall. During the austral winter the trade winds are stronger because of the anticyclones centered on the Indian Ocean; in September-October, precipitations are weaker because of the weakening of the trade winds which occur before the increase of the ZCIT in November-December. This zone is very wet whose annual average reaches more than 1800mm.

a-2) The West coast

During the winter, West coast is under the influence of the trade winds of South-East; the air masses are dry. The moisture has been already deposited in the eastern slope of the island.

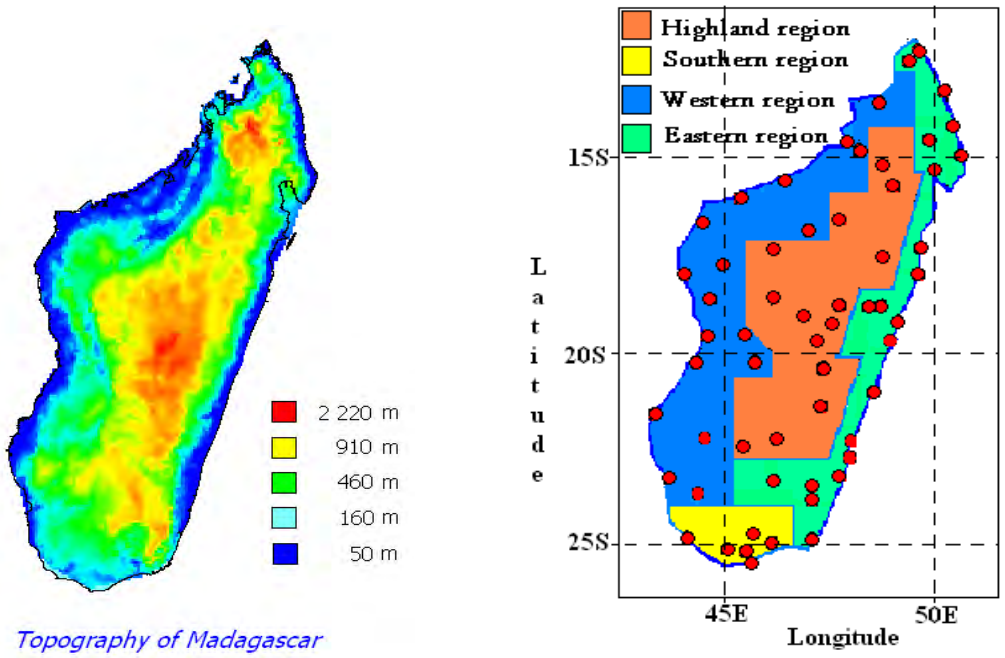

Figure 76: Regionalization of Madagascar with respect to the topography and its precipitation.

a-3) The Highlands

The Highlands corresponds to the high level of the land (between 700 and 1400 m) and is also subjected to the trade winds of South-west but precipitations are weak; the orographical ascents are not very significant and the humid air is not very thick. The most significant precipitations occur during the southern summer, i.e. during the passage of Inter Tropical Convergence Zone in the Southern hemisphere.

a-4) The extreme South

The extreme South is a semi-arid area where the annual average precipitations is lower than 600mm. One observes during the dry season that the temperatures of oceanic surfaces are lower than 18° C, thus the quantity of energy in the ocean is not high enough to return it in a gas state to induce evaporation.

b) Causes of dry events in southern Madagascar

A great deal of information can be gained in studying the dynamics of the atmosphere by the mean of the composite analysis. By considering different atmospheric variables, some deductions can be made simply as the origin of the extreme periods having a great impact

over specific part of Madagascar. Here the study focused on south Madagascar for its rainy season (January to February). In this analysis, many important quantities arise and are described that show a relatively strong spatial consistency over the study region.

Consequently, it can be observed that winds at lower troposphere is depicting anti-cyclone during the drought years over southern Madagascar over the rainy season (Fig. 77).

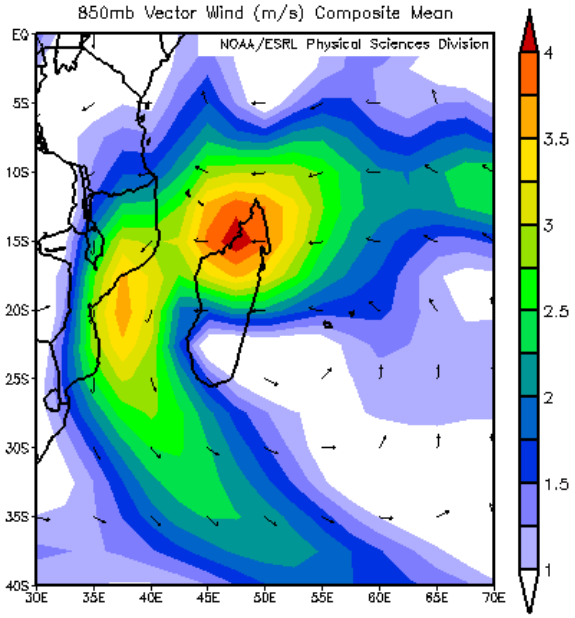

Figure 77: Vector winds (m/s) at 850Pa for drought years in the rainy season of southern region.

This phenomenon is strengthened by the momentum zonal flux that displays the presence of significant features. It exhibits zonal dipole structure accompanied by an increase convective activity in the north that brings heavy rainfall over this region and severe drought over south region with negative configuration (Fig. 78).

As pointed previously, anticyclonic wind flow prevailing over Madagascar analyzed during the dry minus wet episodes in the lower level becomes one of the most important factors for the causes of drought over the south area. As a result of this process, Fig. 79clearly shows deficit of moisture accompanied by high temperature due to adiabatic process. The available moisture is diverted to other area that constitutes a major factor of dryness in southern part of Madagascar.

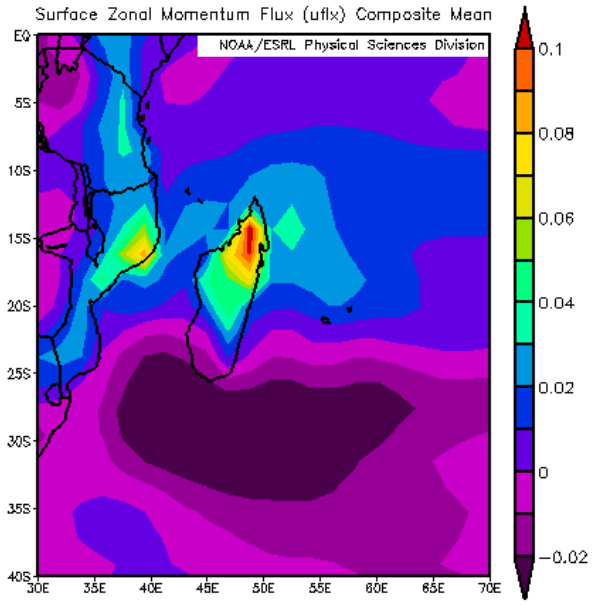

Figure 78: Surface zonal momentum flux averaged over (0-40°S; 30°E-70°E).

This process is also supported by the negative divergence flow in the upper level, which means that there is downward motion indicating depletion of air in the lower level for the southern region of Madagascar (Fig. 80).

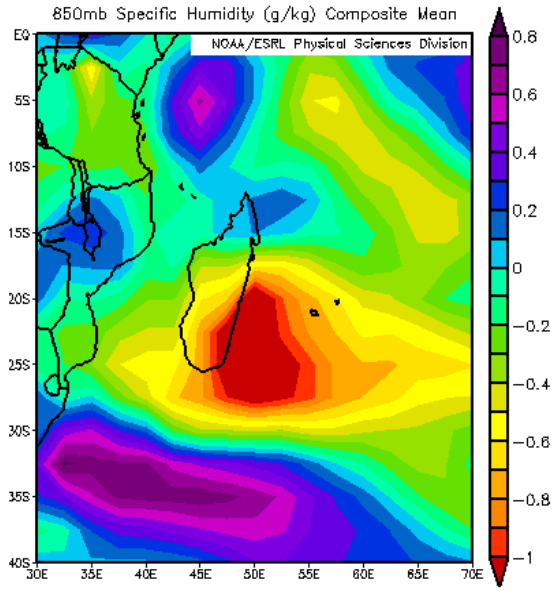

Figure 79: Low level specific humidity for dry minus wet episodes (g/kg).

An investigation is also conducted in parallel through use of the outgoing longwave radiation (OLR) during the southern hemisphere summer season. The OLR alternative signs

represent southwest-northeast wave propagations. The positive OLR over southern Madagascar shows a suppression of convective development as a result of subsidence affecting significantly the climate swings over the region in point regime (Fig. 81).

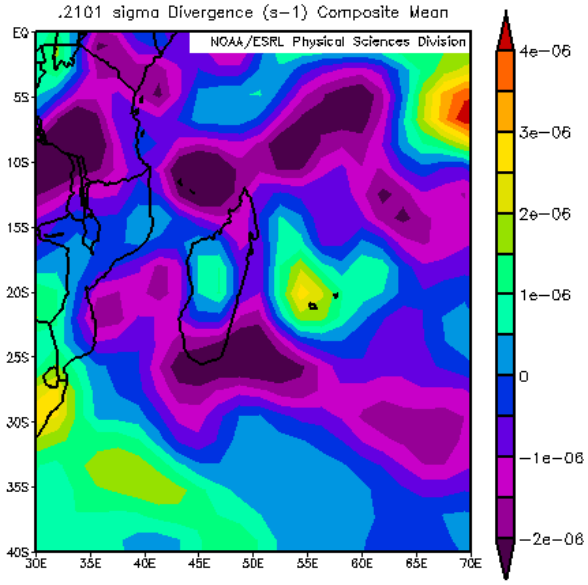

Figure 80: Upper level divergence flow for dry minus wet episodes averaged over (0-40^{o}S; 30^{o}E-70^{o}E).

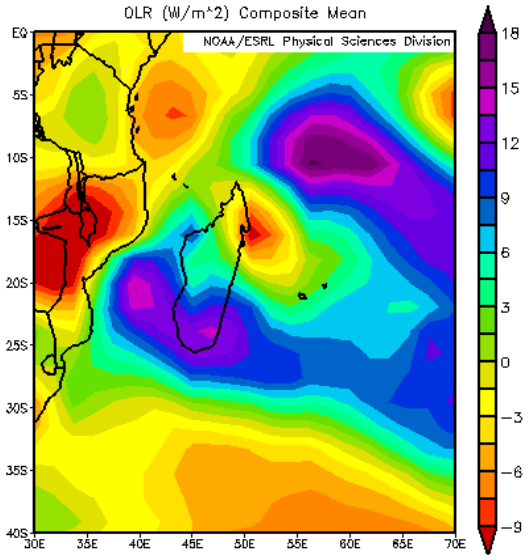

Figure 81: Composite OLR pattern illustrating positive values for dry minus wet episodes.

Furthermore, the geo-potential height anomaly at 500-hPa is considered to further highlight the thermodynamically causes for drought over the region under consideration (Fig. 82). The composite anomaly for geo-potential reveals significant positive values signifying the presence of high geo-potential as a result of the conversion of the available kinetic energy to available potential energy. This conversion results to raise potential energy to higher level and as result enhances anticyclonic motion and descending motion at that level.

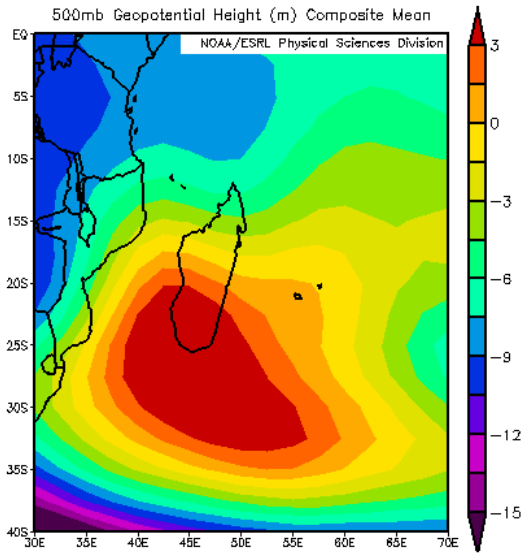

Figure 82: Mid level troposphere Geopotential Height (m) illustrating descending motion.

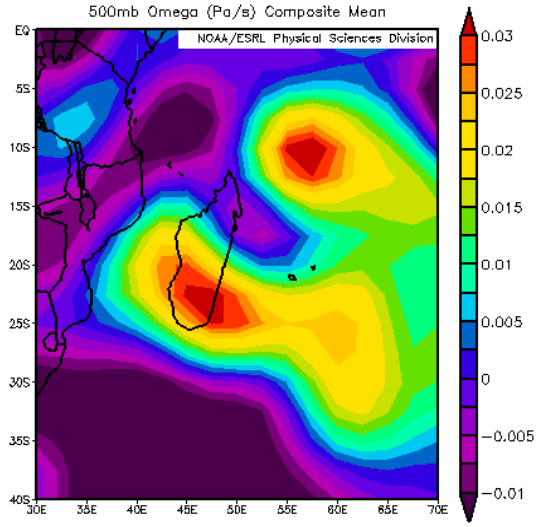

Figure 83: Mid level tropospheric composite Omega (Pa/s) showing the existence of downward motion responsible for the dry condition in the key area i.e. the southern Madagascar.

The omega field clearly demonstrates this process (Fig. 83), where there is positive omega implying a strong subsidence motion at 500-hPa as part of a wave propagation. From lower to upper levels, the dynamical and thermo-dynamical systems are coupled. Over the upper troposphere, the divergent field reveals a wave structure with convergence over areas under investigation linked vertically and horizontally in the low-levels, i. e., upper level convergence and lower level divergence (as a result of the anticyclone) generates subsiding motion (Fig.84). This coupled system produces recurrent drought over south Madagascar.

Circulation for dry events

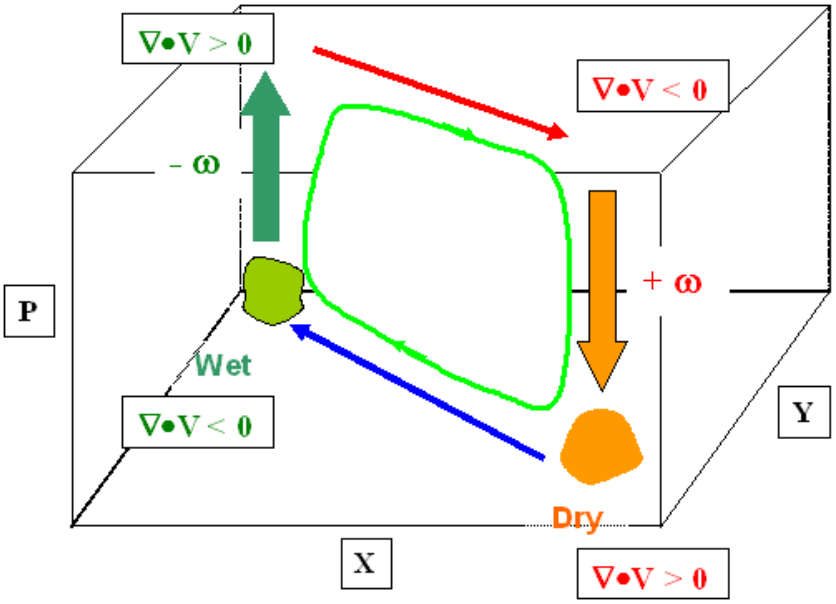

Figure 84: Circulation constructed based on the low and upper-level vector winds indicating the dynamical mechanisms for dry condition over south Madagascar.

c) Modeling the governing dynamics for drought years

In the very first step, cross-correlation (Table 6) has been applied to the atmospheric variables in order to detect which contribute more to the local mechanism enhancing dryness in the southern Madagascar. In the second step, equations (Table 7) have been established by taking account the high correlated variables that constitutes and displays

with the precipitation times series relevant features. They evoke the main source of extreme episodes along the period of study 1951-2000 in January and February.

Table 6: Cross-correlation table of the atmospherics variable time series

With geop=Geopotential; OLR=Outgoing Longwave Radiation; spec_500=Specific Humidity at 500mb; spec_850=Specific Humidity at 850mb; u_200=Zonal wind at 200mb; u_850=Zonal wind at 850mb; v_200=Meridional wind at 200mb; v_850=Meridional wind at 50mb; prec=Precipitation.

	Geop	OLR	Omega	Spec_500	Spec_850	u_200	u_850	v_200	v_850	prec
Geop	1									
OLR	0,08	1								
Omega	-0,02	0,88	1							
Spec_500	-0,2	-0,64	-0,48	1						
Spec_850	0,29	-0,35	-0,28	0,54	1					
u_200	-0,17	-0,07	0	-0,23	-0,23	1				
u_850	0,33	-0,11	-0,24	0,1	-0,07	-0,02	1			
v_200	0,25	0,12	0,14	0,22	0,28	-0,48	0,11	1		
v_850	-0,1	0,36	0,46	-0,48	-0,38	0,54	-0,14	-0,42	1	
prec	-0,26	-0,47	-0,34	0,26	0,33	0,21	-0,32	-0,28	0,08	1

With geop=Geopotential; OLR=Outgoing Longwave Radiation; spec_500=Specific Humidity at 500mb; spec_850=Specific Humidity at 850mb; u_200=Zonal wind at 200mb; u_850=Zonal wind at 850mb; v_200=Meridional wind at 200mb; v_850=Meridional wind at 50mb; prec=Precipitation.

Table 7: Three best combinations of the atmospheric variables based on their correlation.

Predictors	Correlation	Equation
u_850 u_200 OLR	0,623	Y_1= - (0,499 x OLR) + (0,169 x u_200) - (0,37 x u_850) (50)
Geopotential OLR u_850	0,607	Y_2= - (0,339 x u_850) - (0,499 x OLR) - (0,105 x Geop) (51)
Spec_850 Omega OLR	0,520	Y_3= - (0,643 x OLR) + (0,266 x Omega) + (0,184 x Spec_850) (52)

As a matter of fact, Fig. 85, Fig. 86 and Fig. 87 are clearly showing the presence of significant events in 1970 and 1984. It is concluded that after several analyses this very high amount of precipitation comes from the cyclone passage over this area which are categorized as tropical storms. Although tropical storms does not result automatically heavy rainfall, in our case it does for the reason in which how long it takes to cross the interested region.

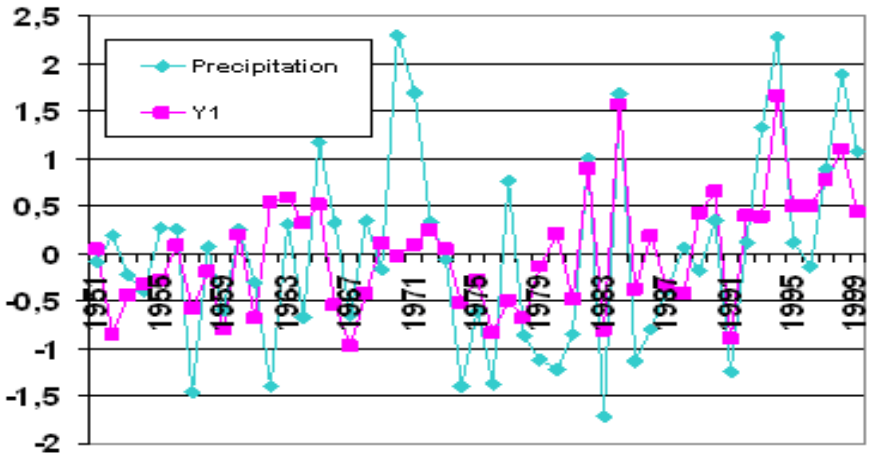

Figure 85: Southern Precipitation index plotted with the optimal combined variables u_850, u_200 and OLR

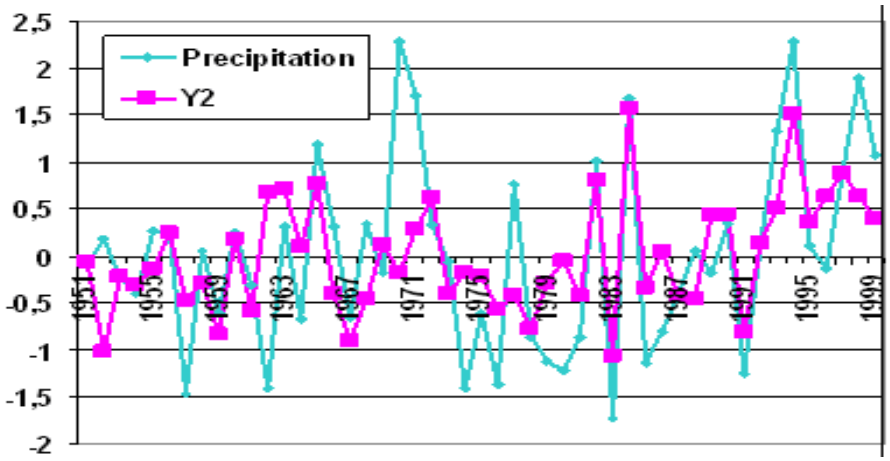

Figure 86: Southern Precipitation index plotted with the optimal combined variables geop, OLR and u_850.

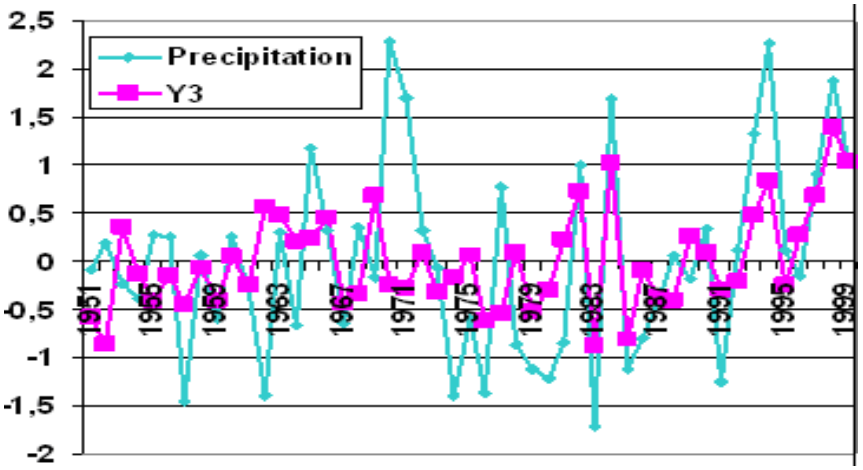

Figure 87: Southern Precipitation index plotted with the optimal combined variables spec_850, Omega and OLR.

Therefore by observing the tropical cyclone tracking information extracted from the website weather.unisys.com/hurricane, it is revealed that the tropical cyclone was passing the key area in January during 48 hours (Fig. 88) and in February during 24 hours (Fig. 89). Thus, this could be one of the explanations of the heavy rainfall mechanism that makes Fig. 85, Fig. 86 and Fig. 87 inconsistent.

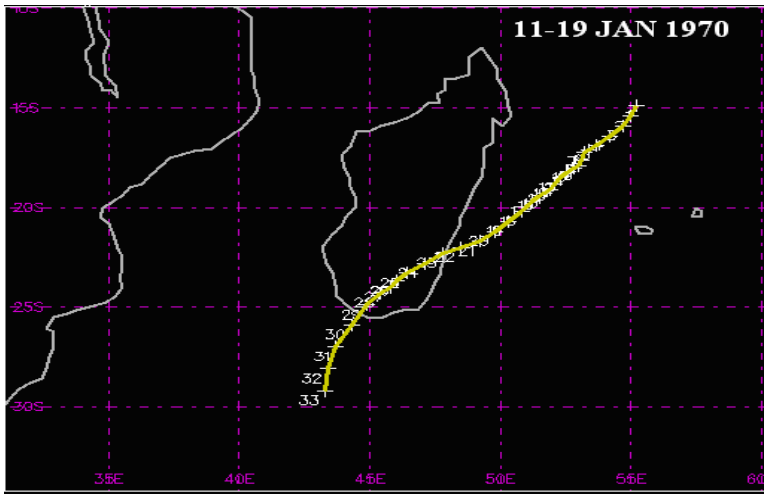

Figure 88: Storm track every 4 hours over the southern Indian Ocean from 11 to 19 January 1970.

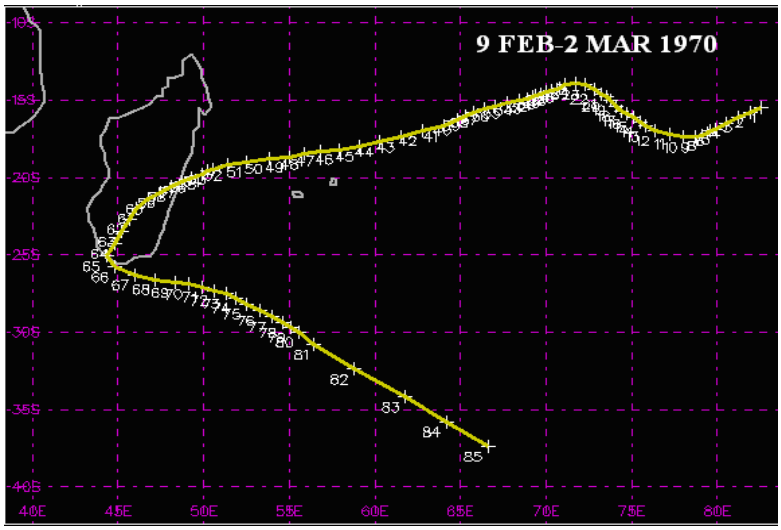

Figure 89: Storm track every 4 hours over the southern Indian Ocean from 9 February until 2 March 1970

1.5. Conclusion

It would be difficult to regionalize without consideration of orography as it modulates the flow pattern and its response to easterly westerly or northerly southerly wind in quite different topography hence considered in the regionalization. Four regions are detected and these are the East coast, the West coast, the highland and the extreme South region. This study is focused on the southern rainfall regional as it is dry prone area of the country. It attempts to search for the mechanisms for dry events in this region. Based on the atmospheric composite analysis salient governing factor is uncovered that constitutes the main contribution of this study. Apart from the atmosphere, it is shown that the ocean plays an important role to the rainfall occurrence over Madagascar by the mean of the tropical cyclone.

Chapter 2: Comparison of predicted results by model with the observed rainfall data of southern Madagascar

2.1 Introduction

It is found from the previous studies that Southern Madagascar rainfall during the austral summer season depends on quantitative dynamical atmospheric variables. This simple conceptual framework suggests that the ability to predict seasonal mean rainfall during its active phase will depend on the relative contribution of these externally forced components. Indeed, it is important to develop an early warning system for rainfall variability based on a sound scientific understanding of its causes. Likewise, regional outlooks are produced only a few months before the onset of the Southern rainy season. As rainfall has a great effect in many sectors of society, this lead of time may not be sufficient but makes our study more efficient.

In short, African rainfall prediction basically related to the climate variability has progressed in recent years. It has been recognized that atmospheric variables over the tropical oceans may be skillful in climate prediction as SST indices (Jury MR, Mulenga HM, Mason SJ, Brandao A, 1997). The presence of wind forced, ocean Rossby waves is believed to contribute to this ((Xie et al., 2001); (Jury MR, Huang B, 2004)) and outlined in part one of (Yeshanew & Jury, 2006a). An alternative statistical technique is the stepwise selection of predictors drawn from the key areas based on the correlation maps with respect to rainfall etc. ((Jury MR, Mulenga HM, Mason SJ, Brandao A, 1997); (Jury MR, 2002a); (Camberlin P, Jaincot S, Poccard I, 2001). Stepwise regression is also used in the part three of (Yeshanew &

Jury, 2006c) to construct multivariate models for climate, stream flow and agricultural resource indices. Similarly, rainfall prediction of Southern Madagascar is analysed through stepwise of regression based on the NCEP reanalysis atmospheric and surface data as it is a recent and an interesting approach. This last is aimed to consider which components of the ocean-atmosphere system contribute to its water resource then to compare the predicted results by model with the observed rainfall data of southern Madagascar and finally to give contribution to the predictability of Malagasy rainfall through applied climatology.

This analysis consists of the introduction followed by the data and methods. The analyses of the results are presented in the next section and the conclusion is given at the end.

2.2. Data

Apart from the VASCLIMO rainfall data the prediction models developed for southern Madagascar consulted in this study used atmospheric data from the NCEP-NCAR reanalysis restricted from 1951 to 2000. An attractive characteristic of the NCEP-NCAR reanalysis with respect to climate study is its consistency.

a) Rainfall

Most of the Madagascar's rainfall occurs during the summer season, generally from November to April. In this study however, the peak period is considered so as we focus on the southern region the summer season is reduced to January-February only. Monthly gridded rainfall data extracted from VASCLIMO (Beck & Rudulf, 2004) 1951 to 2000 with a spatial resolution of 0.5^{o} x 0.5^{o} is used in this analysis.

b) The NCEP-NCAR reanalysis

The National Centers for Environmental Prediction-National Center for Atmospheric Research (NCEP-NCAR) have completed a reanalysis project with a current version of the

Medium-Range Forecast (MRF) model (Kalnay et al., 1996). This dataset consists of a reanalysis of the global observational network of meteorological variables (wind, temperature, humidity on pressure level, surface variable such as the Outgoing Longwave Radiation) to perform data assimilation throughout the period 1948 to present. Data are reported on a 2.5^{o} x 2.5^{o} grid every 6 h on 17 pressure levels from 1000 to 10 hPa, which are good for studying synoptic weather systems.

2.3. Methods

To establish predictability, simple linear cross-correlation analysis and stepwise regression are employed.

a) Teleconnection analysis and definition of key areas

Cross-correlation analysis is used to identify the temporal and spatial relationship between the southern rainfall dataset and the atmospheric variables. Significant results obtained from this technique help for establishing the connection between variables to predict and predictors.

Not all parts of the global atmosphere and ocean could be regions of potential predictors. In general, the source of predictability mainly detected in this study is the pacific zone as long as the sea surface temperature during the winter season constitutes one characteristic of the rainfall climatology of Madagascar.

Moreover, certain longitudes may offer greater predictability and we refer to these key areas. A key area must be large enough to provide effective information from the ocean-atmosphere interactions, for instance the equatorial and gradient modes of Atlantic SST (Camberlin P, Jaincot S, Poccard I, 2001). Furthermore, the Indian Ocean dipole is another potential key for Africa (Jury MR, Huang B, 2004).

b) Strategy in stepwise regression

In stepwise regression the strategy is to search for variables forming minimum residual errors with the target variables that could be retained in the equation. In other words, variables to maximize the partial correlation are chosen and the other previously selected variables are removed. Therefore, a list of several potential predictors is available and the list is repeatedly searched for variables to be included in the model. The optimally associated variable is used first, then the second best, and then the third; after which the application of the regression are checked.

The variation shown in the 'presumed' rainfall data series are based on the number of predictors involved in the model and the character of the target time series. The averaged southern rainfall over the peak season (January-February) which is critically determined by a random model structure is involved as target time series in this study.

Equally important, the dependence in time equation considering the year as the predictor variable and the 'presumed' rainfall data series as the dependent variable is also established. Thus, the resulted rainfall forecast through linear regression model of a single predictor by the method of linear least squares shows gradual increase and appears as an up-trend during the period considered in this analysis.

c) Validation of prediction models

The predicted and the observed values are compared and clustered in different categories (above normal, normal and below normal). Values that fall in each category are recorded to compute the hit rate. By definition, a hit rate is the proportion of events for which a warning was provided correctly (Mason SJ, 2000). The hit rate and the cross-correlation are known as a measure of performance to assess the skill of any model.

2.4. Results and discussions

a) Target and predictors

Knowing that the average southern rainfall during the peak austral summer season is the target variables, as it constitutes an important water resource for the society, the findings of predictors in order to establish regression for developing prediction models is leaded. With this in mind, different key areas from the lagged 3 and 6 months over the global map are extracted with respect to each surface and atmospheric variables.

Afterward, partial correlation considering the observed south rainfall data as dependent variable and the enlisted parameters (Table 8) as predictors helps us to select the best combination for the linear model.

Table 8: Candidate predictors: representation and domains

lag	Parameter	Variables	Acronym	Domain
3	OLR	African OLR	Afolr	(15°W-10°E, 38-22°N)
3		Indian Ocean OLR	Iolr	(50-85°E,10°N-5°S)
3		North Atlantic OLR	nAolr	(40-20°W,13-2°N)
3		North Pacific OLR	nPolr	(150-100°W, 0-15°S)
3	SST	North Atlantic SST	nAsst	(60-20°W, 40-30°N)
3		North Pacific SST-1	nPsst-1	(160-125°W, 52-39°N)
3		North Pacific SST-2	nPsst-2	(170°W-150°E,44-32°N)
3		North Pacific SST-3	nPsst-3	(110-75°W,0-15°S)
3	Q500	Indian Ocean Specific humidity-1	Iq500-1	(60-90°E,10-25°S)
3		Indian Ocean Specific humidity-2	Iq500-2	(60-110°E,30-40°S)
3	UV200	Indian Ocean zonal wind-1	Iu200-1	(60-90°E,10-25°S)
3		Indian Ocean meridional wind-1	Iv200-1	(60-90°E,10-25°S)
3		Indian Ocean zonal wind-2	Iu200-2	(60-110°E,30-40°S)
3		Indian Ocean meridional wind-2	Iv200-2	(60-110°E,30-40°S)
3	UV850	Indian Ocean zonal wind-1	Iu850-1	(60-90°E,10-25°S)
3		Indian Ocean meridional wind-1	Iv850-1	(60-90°E,10-25°S)
3		Indian Ocean zonal wind-2	Iu850-2	(60-110°E,30-40°S)
3		Indian Ocean meridional wind-2	Iv850-2	(60-110°E,30-40°S)
6	OLR	North Pacific OLR	nPolr	(135-85°W,10°N-5°S)
6	SST	Indian Ocean SST	Isst	(40-60°E, 30-40°S)
6		North Pacific SST-1	nPsst-1	(130-170°E,48-34°N)
6		North Pacific SST-2	nPsst-2	(160-130°W,45-32°N)
6		North Pacific SST-3	nPsst-3	(110-75°W,5°N-15°S)
6		South Atlantic SST	sAsst	(0-20°E,0-20°S)
6	Q500	Indian Ocean Specific humidity-1	Iq500-1	(60-90°E,10-25°S)
6		Indian Ocean Specific humidity-2	Iq500-2	(60-110°E,30-40°S)
6	UV200	Indian Ocean zonal wind-1	Iu200-1	(60-90°E,10-25°S)

6		Indian Ocean meridional wind-1	Iv200-1	(60-90°E,10-25°S)
6		Indian Ocean zonal wind-2	Iu200-2	(60-110°E,30-40°S)
6		Indian Ocean meridional wind-2	Iv200-2	(60-110°E,30-40°S)
6	UV850	Indian Ocean zonal wind-1	Iu850-1	(60-90°E,10-25°S)
6		Indian Ocean meridional wind-1	Iv850-1	(60-90°E,10-25°S)
6		Indian Ocean zonal wind-2	Iu850-2	(60-110°E,30-40°S)
6		Indian Ocean meridional wind-2	Iv850-2	(60-110°E,30-40°S)

Table 9 suggests that among the key area selected OLR, SST, mid level specific humidity appear to be significant at 95% level. As Pearson correlation includes 0.3 significant correlations, it comes out that being aware of Iolr, nAolr and nPsst three months before the summer period, season forecasting could be established for the eventual average southern rainfall (Eq.53). Similarly, a kind of warning system could be established 6 months before the austral wet event based on the surface and atmospheric variables nPsst-1, nAsst and Iq500 (Eq.54).

Predicted Rainfall $_{-3}$ = (-1.592* Iolr)-(2.345*nAolr)-(53.297*nPsst) + 482.684 ; r = 0.596 (53)

Predicted Rainfall $_{-6}$ = (23.979*nPsst)+(7.779*nAsst)-(61.196*Iq500)-361.595 ; r = 0.417 (54)

Table 9: Partial correlation between the candidate predictors and the target variable.

Parameter	Acronym	Correlation
Lag (month) 3		
OLR	Afolr	0,02
	Iolr	-0,31
	nAolr	-0,39
	nPolr	-0,13
SST	nAsst	0,19
	nPsst-1	-0,08
	nPsst-2	0,39
	nPsst-3	0,04
Q500	Iq500-1	-0,12
	Iq500-2	-0,13
UV200	Iu200-1	0,14
	Iv200-1	-0,05
	Iu200-2	-0,08
	Iv200-2	-0,11
	Iu850-1	0,24
	Iv850-1	0,02
	Iu850-1	-0,11
UV850	Iu850-2	-0,11

Parameter	Acronym	Correlation
Lag (month) 6		
OLR	nPolr	-0,06
	Isst	-0,11
	nPsst-1	0,27
	nPsst-2	-0,01
	nPsst-3	-0,09
SST	sAsst	0,22
	Iq500-1	-0,29
Q500	Iq500-2	-0,05
	Iu200-1	-0,17
	Iv200-1	0,01
	Iu200-2	-0,11
UV200	Iv200-2	0,04
	Iu850-1	0,09
	Iv850-1	0,2
	Iu850-2	0,2
UV850	Iv850-2	0,11

In other words, the best predictors are strongly linked to the actual rainfall and their grouping aimed to demonstrate the lag relationships which have forecasting application. Fig. 90 and Fig. 91 plot the sequence of the observed and the rainfall prediction based the three best predictors showing the interannual variability characteristics of rainfall generally over the Indian Ocean.

Obviously, most of the effective key areas indicate that Indian Ocean basin mainly constitutes strategic domain for rainfall prediction especially for Madagascar.

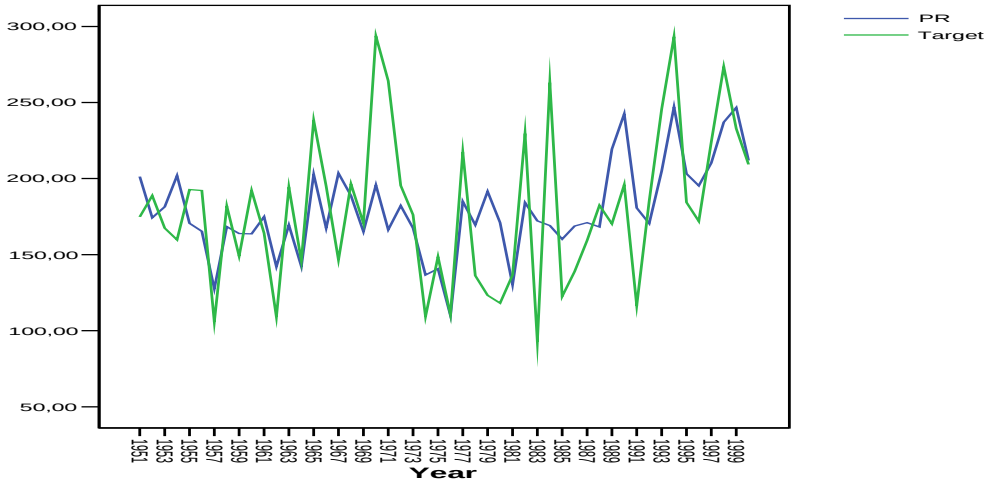

Figure 90: Interannual variations sequence plots of the observed and predicted rainfall based on the best predictors at 3-month leads.

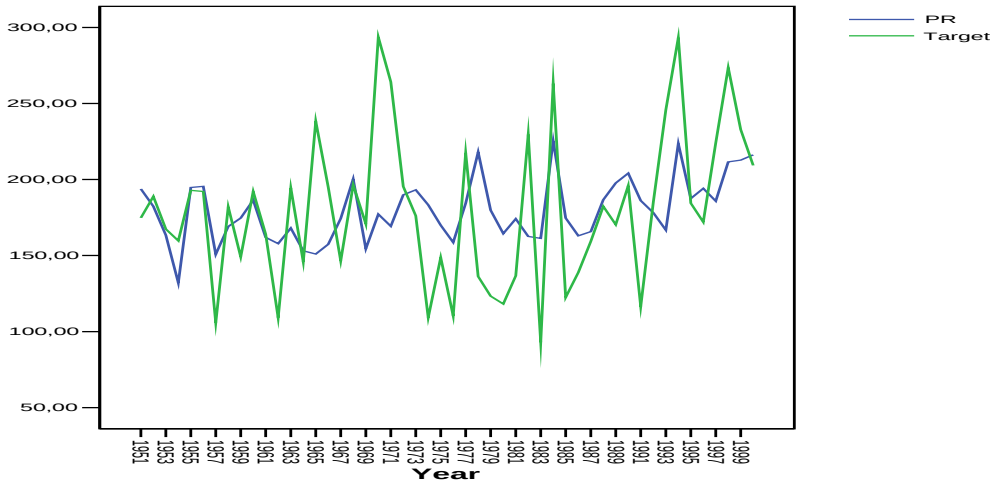

Figure 91: Interannual variations sequence plots of the observed and predicted rainfall based on the best predictors at 6-month leads.

a.1) OLR

During the break monsoon periods, the core of the jet stream source of high convectivity first identified by (Bunker, 1965) originating in the southern Indian Ocean near Madagascar is directed to Indian subcontinent leading dry condition over Madagascar. But during the active monsoon period, the core of this of source of deep moisture is directed to south Indian enhancing heavy rainfall over Madagascar at the end. Before attaining the big island the low jet flow being worth interpreted by a negative OLR anomaly is subsequently diverted towards equator resulting deep convective in that region. It describes other strategic key area and plays an important role in determining the eventual rainfall amount of the area of study. The same mechanism is likely to appear in the Atlantic Ocean as it is found in the tropical band instead with different environmental situation (Fig. 92).

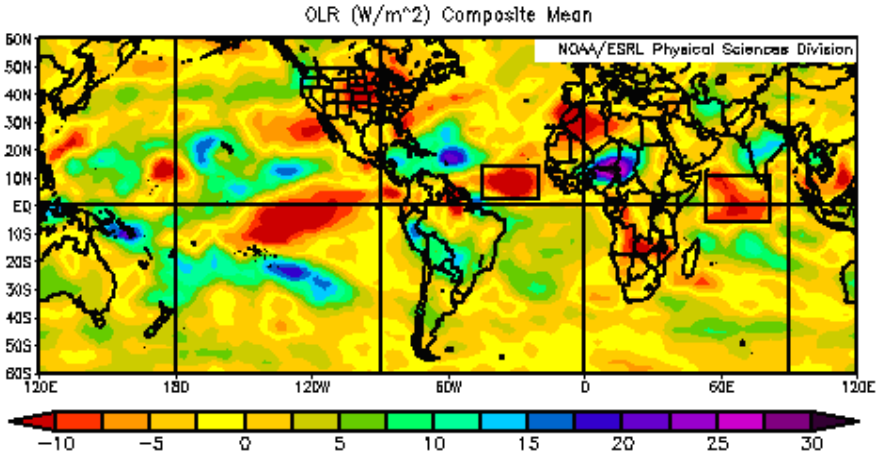

Figure 92: Global Outgoing Longwave Radiation environment three months before the austral summer season among with the strategic equatorial key areas.

a.2) SST

Among the best predictor, teleconnection between sea surface temperature in the North Pacific Ocean and Malagasy precipitation especially in the south is detected both at 3 and 6-month leads. The situation of Madagascar which is in the Indian Ocean benefits to this analysis. Indeed many authors have identified that Pacific El Nino conditions are associated

with warming of the west-central Indian Ocean ((Cadet, 1985) ; (Latif & Barnet, 1995); (Nicholson, 1997); (Reason et al., 2000)) and increased upper level westerly winds over Africa ((Harrison, 1986); (Jury, Mulenga, & Mason, 1999)).

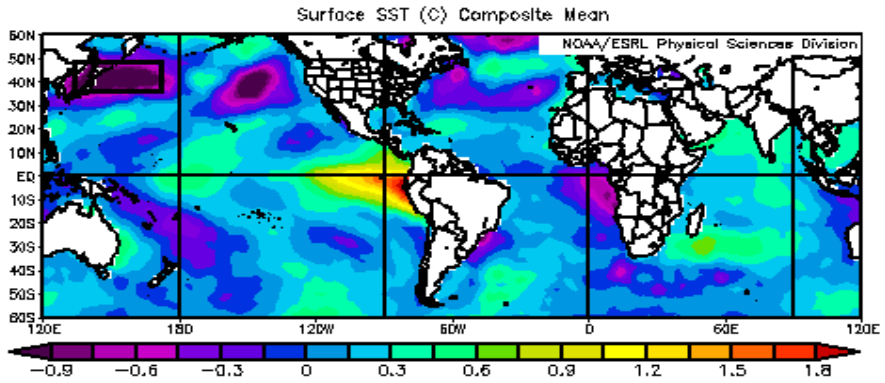

Figure 93: Global Sea surface temperature environment six months before the austral summer season and description of the key area located in the north pacific ocean.

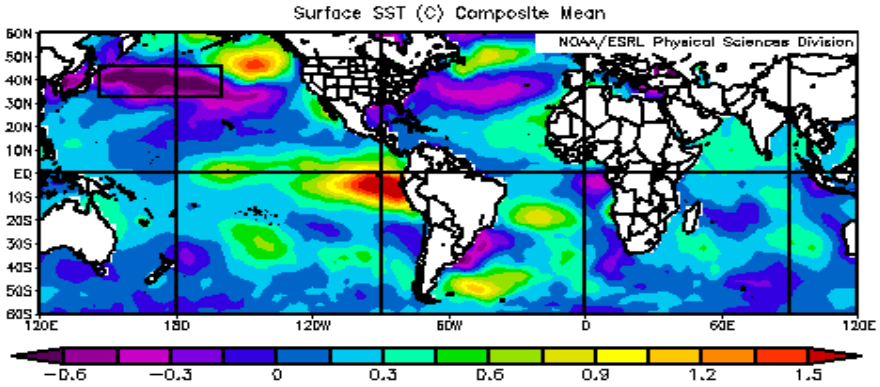

Figure 94: Global Sea surface temperature environment three months before the austral summer season and north pacific key area.

The north pacific cool SST is progressively forming dipole with positive anomaly SST known as Nino1-2 and Nino 3 enhancing generally wet conditions. The SST evolution from at 6-month to 3-month leads in the north Pacific can be identified from the Fig. 93 and Fig. 94. Prior to the development of El-Nino conditions in the eastern Pacific, the tropical eastern Atlantic Ocean begins to cool. A zonal overturning circulation arises ((Hastenrath, 2001), 2001) with upper westerly/lower easterly flow linking subsidence over central Africa and

contributes to a near-simultaneous decrease of most river flows across Africa except around Lake Victoria.

In this manner, the tropical Atlantic plays an important role in the transmission of ENSO throughout the African region. However, underlying SST anomalies over the Indian Ocean tend to form a favorable condition for convective activity and may sustain enhanced precipitation. Moreover, hurricanes can only form in extensive ocean areas with a surface temperature greater than 26.5 deg.C. This is because the warm ocean water provides sensible heat and water vapor that fuels the intense convection of hurricane, and assists the conversion of a cold-core tropical depression to a warm-core cyclone.

b) Validation test

Before analysing the southern rainfall trend, the performance of the predicted target variables eventually considered as predictors is examined. Hence, the hit rates attain 50% for both 3-month and 6-month lead. The cross-correlation between observed and predicted rainfall over southern region reveals significant results which are 0.60 and 0.42 respectively at 3-month and 6-month lead.

Focusing on the time dependent equation given by the linear regression model, significant correlation at 95% level is calculated between the observed and the predicted rainfall datasets: 0.44 for lag -3 and 0.45 for lag- 6. Normal increase of the amount of rainfall is expected in the future according to the tendencies derived from the target variables. (Fig. 95, Fig. 96)

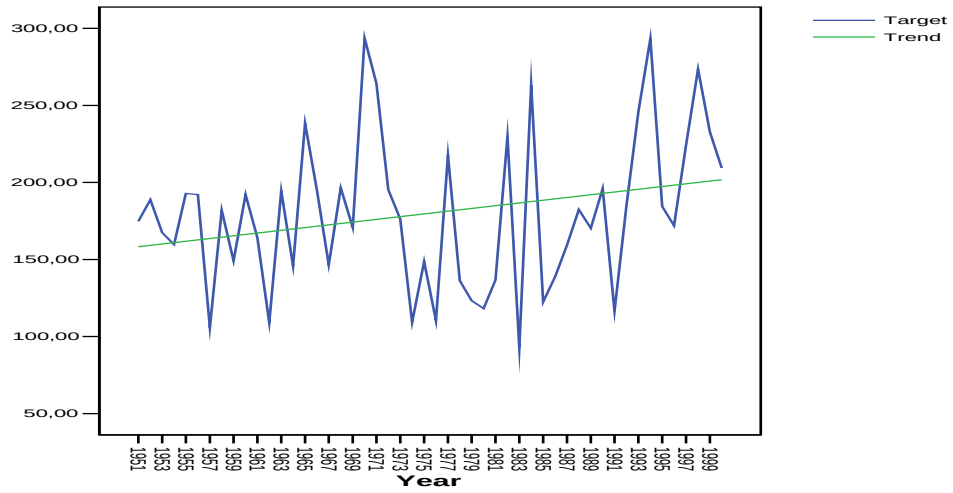

Figure 95: Predicted rainfall at 3-month lead tendency over 50 climatology years of the southern region. Trend=0.89*year-1572,24.

Skill test is also presented for rainfall in the period from 1951 to 2000 with scatter plots in order to see in which intervals the predicted values fall with respect to the observed (Fig. 97). The hit interval is [-1.0; 1.0] meaning that examining the plots many extreme years are identified by referring to the predicted values. However, it's still making the hit rates (50%) significant suggesting that our model is quite relevant and applicable for an early warning system.

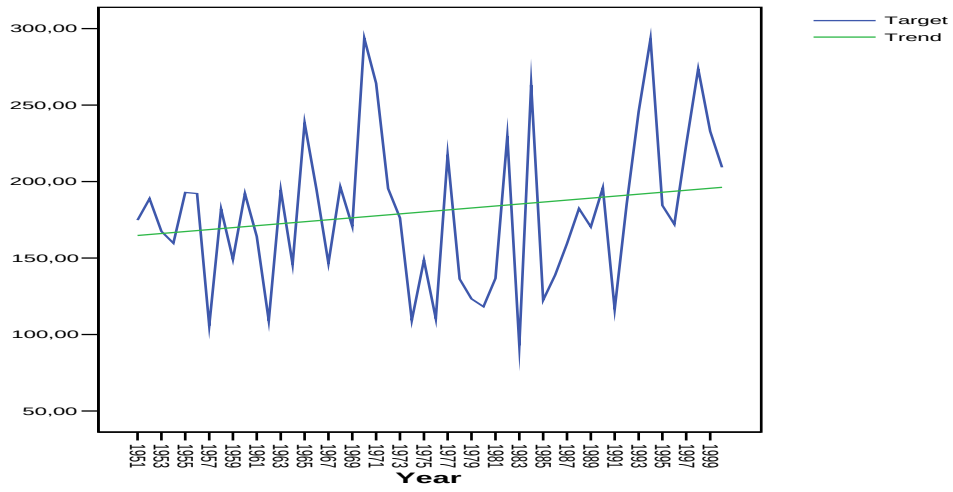

Figure 96: Predicted rainfall at 6-month lead tendency over 50 climatology years of the southern region. Trend=0.64*year-1089,80.

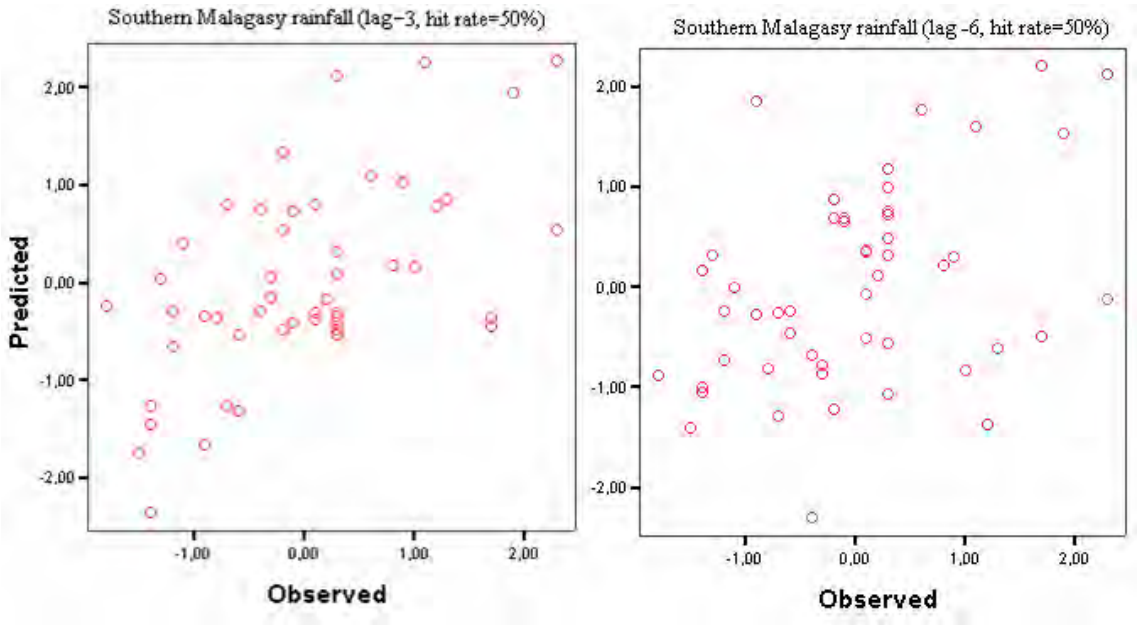

Figure 97: Southern rainfall scatter plots combining the observed and the predicted datasets.

c) Extreme events analysis

Provided that the two results are quite similar, the explanation of those extreme events could be highlighted by making composite analysis of the years corresponding to the highest (1998, 1994,1970,1990,1999 and 1994) minus the lowest (1983, 1957, 1962, 1976, 1957 and 1981) abnormal observed rainfall from 1951 to 2000 for both observed and predicted rainfall. The simulated results are obtained from the website http://www.cpc.noaa.gov/. NCEP reanalysis atmospheric and surface data are consulted in this step of study such as the lower level wind vector, sea surface temperature and the precipitation rate. Hence, Fig.99 displays that extreme events in the southern region of Madagascar can be one response to the cyclonic circulation centred in the south enhancing negative OLR anomaly (Fig. 99) and heavy precipitation rate in that region in due time (Fig. 100).

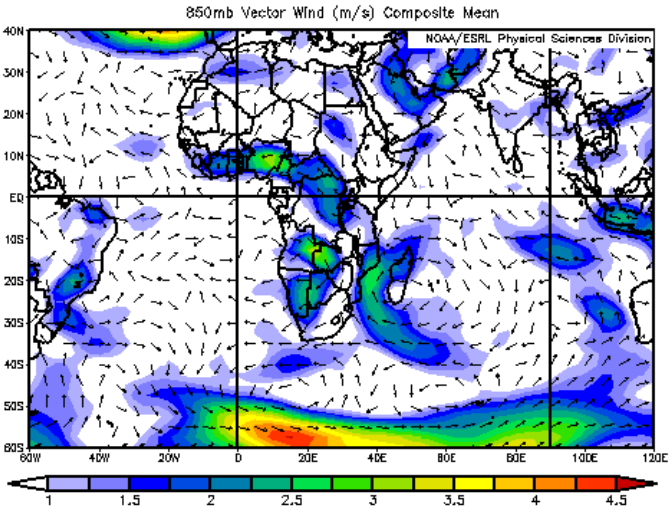

Figure 98: Regional composite low level wind vector related to the southern extreme events

Although this area of study is already proved to be as dry prone area, it occasionally experiences wet events knowing that it comes from the development of low wind pressure allowing strong depression centred near to the extra-tropical region including the southern Madagascar.

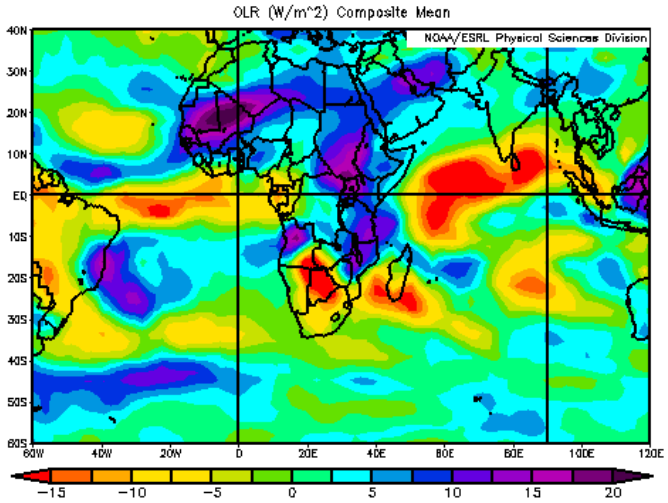

Figure 99: Regional composite OLR derived from to the southern extreme events.

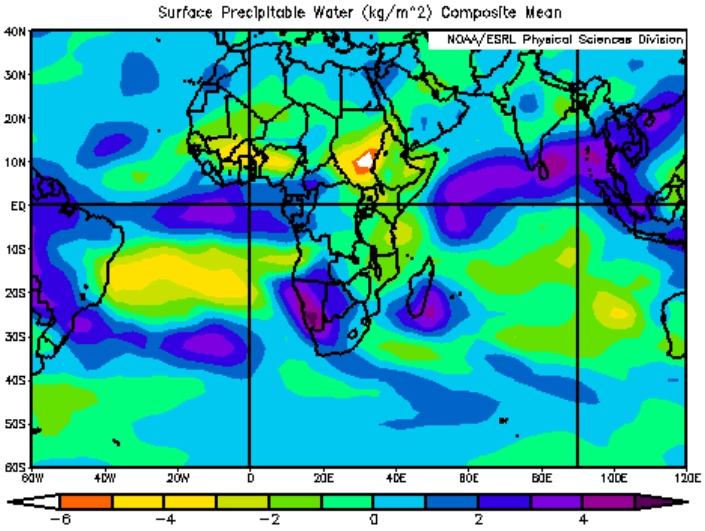

Figure 100: Regional composite surface precipitable water linked to the southern extreme events.

2.5. Conclusion

In this study, predictive models for southern Madagascar summer season rainfall is developed based on atmospheric and surface variables data 3 and 6-month leads. It is assessed from this study the model performance in order to determine the best predictors. Provided that Madagascar is located in the Indian Ocean with an inter annual variability rainfall characteristic, this present analysis could clearly bring out the importance of jet flow being worth interpreted by a negative OLR anomaly during the break monsoon activity. It is directly linked to the amount of moisture transported to the big island during the summer season enhancing an equatorial deep convection and constitutes one significant summer rainfall predictor. One consistent and strategic key area driving advantageous moisture to the southern region of Madagascar is the Pacific sea surface temperature proving the existence of teleconnection between each ocean. Despite that southern is the driest Malagasy region; it is uncovered from the temporal evolution of the predicted rainfall the normal increase which is consistent with the observed rainfall recorded from 1951 to 2000. Equally important, further

research is needed in order to have long term warning systems and for decision making to reduce adverse impacts.

General Conclusion

Climatologic study of the monthly precipitation of Madagascar during the period 1951-2003 reveals that its variability characteristic in term of precipitation is related to the general circulation model. Malagasy annual rainfall variability is strongly influenced by the zonal circulation passage such as the ITCZ during the hot season. This mechanism is followed in winter by the wind elevation from the extra tropical perturbation hitting the mountain chain along the oriental coast that brings a huge quantity of precipitation in this region and makes orography as dominant feature to the rainfall regionalization. Besides, several known circulation models and mechanisms occurring in different atmospheric layer levels are responsible for this variability.

In this work, we have also emphasized that drought becomes serious while moving at the same time to southerly and westerly according the thermal wind mechanism. Furthermore, cumulated annual rainfall for 1951-2003 periods has experienced insignificant decrease by taking account precipitation trends within the regions. In other terms, global study of the precipitations predicts light decrease between 80 and 600mm in the late century.

The reduction of the dimension of the monthly rainfall over Madagascar from 1951 to 2000 through the PCA methods is thus able to bring out the dominant spatial and temporal patterns with the most prominent inter annual variability such as 1983, 1991, 1997. The most meaningful of the extracted components may not even exist however the most important thing is the one closest to the index used to characterize phenomenon displaying in contemporary climatology. Therefore, it is identified by the first component that Madagascar rainfall is directly linked to the QBO and the TC index. From the second component, the contrast between North and South is more highlighted. This feature could be modulated by the Southern Oscillation (ENSO, SOI). The third mode describes the polarity between Eastern and Western region.

Understanding the physical mechanisms responsible for the occurrence of the main rainfall patterns over Madagascar is one key issue resolved here. For better understanding, salient factor that determines these modes are investigated. Thus, the leading mode representing almost 49% of the rainfall could be optimally derived as a contrast between the North and the South stating that the southern region receives less precipitation than the northern region. Consistently, this polarity is shifted to NE and SW provided that 24% of the rainfall datasets constitutes the second mode. Conversely, strong East-West opposition is depicted from the third mode explaining almost 10% of Madagascar rainfall.

It can be learnt from this analysis that tropical cyclone can never be neglected from the rainfall climatology of Madagascar because of its ability to modify the climate over Madagascar. It is also found from the correlation analysis that there is an evident relationship between the eastern region and the tropical cyclone. The amount of rainfall in each region is influenced by the cyclone passage despite its lack in number.

The main key factor prohibiting the rainfall occurrence is the observed SST anomalies which is one of the crucial conditions for tropical cyclone development. Generating El-Niño event, almost the whole island was strongly affected.

Analysis of SPI for different durations will determine the type of drought an area is experiencing. The temporal invariance of the SPI allows for the significance of short-term and long-term precipitation events to be captured using the same methodology. The SPI allows for the simultaneous display of events at multiple scales. This is an important feature given that it is possible to experience drought conditions for one time-scale while experiencing wet conditions for another. It is this temporal invariance, the ability to measure rainfall at multiple timescales with the same method that makes the SPI such a versatile tool for reporting precipitation conditions.

As an example, it may be possible to have dry conditions when analyzed at an annual period, but experience flooding in the short term. The effects of the long-term drought may mean that reservoir levels are below average and water supplies may have to be rationed. Conversely, the effects of the short-term flood may mean that crops have been washed away, waterborne disease may be rampant, and people's lives may be at risk due to areas being underwater. For these reasons it is necessary to monitor precipitation conditions at a variety of time scales.

Some potential advantages of extreme value theory in modeling rainfall time series have been pointed out. The reliance on more conventional statistical methods can result in labelling regional precipitation over Madagascar as more "surprising" than they ought to be. Strong evidence of heavy tail distribution has been presented from the Q-Q plot although its origin is not quite identifiable because of the fluctuation due to the composition of different phenomenon prevailing around the area of study. Hopefully, it has been demonstrated from our regional analysis how the statistics of exceedences can readily incorporate information about the accurate estimates of flood probabilities, exploiting the fact that some extremely parameters only gradually vary within a region. It is useful to use more data in order to have not only the approximation valid but the degree of uncertainty less. Furthermore, we have focused only on the temporal pattern in our treatment of extremes because in principle, fully spatial-temporal modeling is unrealistic as well as its applications so far are rather limited. However, the main advantage of this study is the establishment of the return period of the very huge amount of rainfall that occurs in different region of Madagascar. Moreover, it seems to play an important role to the extreme events prediction for different purposes such as allegation of many sorts of damage.

This study focused also on the southern rainfall regional as it is dry prone area of the country. It attempts to search for the mechanisms for dry events in this region. Based on

the atmospheric composite analysis salient governing factor is uncovered that constitutes the main contribution of this study. Hence, source of predictive models for southern Madagascar summer season rainfall is developed based on atmospheric and surface variables data 3 and 6-month leads. It is assessed from this study the model performance in order to determine the best predictors. Provided that Madagascar is located in the Indian Ocean with an inter annual variability rainfall characteristic, this present analysis could clearly bring out the importance of jet flow being worth interpreted by a negative OLR anomaly during the break monsoon activity. It is directly linked to the amount of moisture transported to the big island during the summer season enhancing an equatorial deep convection and constitutes one significant summer rainfall predictor. One consistent and strategic key area driving advantageous moisture to the southern region of Madagascar is the Pacific sea surface temperature proving the existence of teleconnection between each ocean. Despite that southern is the driest Malagasy region; it is uncovered from the temporal evolution of the predicted rainfall the normal increase which is consistent with the observed rainfall recorded from 1951 to 2000.

Equally important, further research is needed in order to have long term warning systems and for decision making to reduce adverse impacts based on the dynamical variables because the very last section is just like a kind of comparison of the predicted results model with the observed datasets. So this field of research should be further analysed.

Bibliography

Barr-Kumarakulasinghe, A., S., & Lwiza, K. (1998). Scales of deep convective clouds and the direct adjustment. *Meteor. and Atmos. Phys., in press* .

Baum, S. K. (1997). *Glossary of Oceanography and the Related Geosciences with References.* Texas Center for Climate Studies, Texas A&M University Copyright 1995-1996.

Beck, C., & Rudulf, B. (2004). *A new monthly precipitation climatology for the global land area for the period 1951 to 2000.* DWD, Klimastatusbericht KSB 2004, ISSN 1437-7691, ISSN 1616-5063 (Internet), ISBN 3-88148-402-7, 181-190.

Bessafi M. and M.C. Wheeler. (2005). Modulation of south Indian Ocean tropical cyclones by the Madden-Julian oscillation and convectively-coupled equatorial waves. *Mon. Wea. Rev.*

Bunker, A. (1965). Interaction of the summer monsoon air with the Arabian Sea. *'(Preliminary analysis)', Proc. Symp.Met. Results International Indian Ocean Expedition, Bombay* .

Cadet, D. (1985). The Southern Oscillation over the Indian Ocean . *J. Clim., 5* , 189-212.

Camberlin P, Jaincot S, Poccard I. (2001). Seasonal and atmospheric dynamics of the teleconnection between African rainfall and tropical sea-surface temperature: Atlantic vs.ENSO. *Int J Climatol 21* , 973–1005.

Coles, S., & Twan, J. (1994). Directional modelling of extreme wind speeds. *Applied Statistics 43* , 139-157.

D'Abreton P.C., Lindesay J.A. (1993). Water vapour transport over Southern Africa during wet and dry early and late summer months. *International Journal of Climatology, n° 13* , p. 151-170.

Dawson, T.H. (2000). Maximum wave crests in heavy seas. *Journal of Offshore Mechanisms and Arctics Engineering-Transactions of AMSE 122* , 222-224.

Doncques, G. (1975). *Contribution geographique a l'etude du climat de Madagascar.* Nouvelle Imprimerie des Arts Graphiques.

Duchiron, B. (2002). *Variabilite interannuelle de la pluviometrie dans l'espace riverin de l'Ocean Indien.*

Elsberry, R.L. (ed.). (1988). A Global View of Tropical Cyclones. *Naval Postgraduate School* , 185 pp.

Fisher, R., & Tippett, L. (1928). On the estimation of the frequency distributions of the largest or smallest member of a sample . *Proceedings of the Cambridge Philosophical Society 24* , 180-190.

Flohn H. (1960). Equatorial westerlies over Africa, their extension and significance. *Symposium de Nairobi* , 253-267.

Gnedenko, B.K. (1943). Sur la distribution limite du terme maximum d'une serie aleatoire . *Annals of mathematics 44* , 423-453.

Gray, W. M., J. D. Sheaffer, and J. A. Knaff. (1992). Influence of the stratospheric QBO on ENSO variability. *J. Meteor. Soc. Japan, 70* , 975-995.

Gray, W.M. (1968). Global view of the origin of topical disturbances and storms. *Mon. Wea. Rev., 96* , 669-700.

Gruber, A., and A. F. Krueger. (1984). The status of the NOAA outgoing longwave radiation data set. *Bull. Amer. Soc., 65* , 958-962.

Harris, R.I. (2001). The accuracy of the design values perdicted from extreme value analysis. *Journal of wind Engineering and Industrial Aerodynamics 89* , 153-164.

Harrison, M. (1986). A synoptic climatology of south African rainfall variations. *P.hD. thesis, Univ. Witwatersrand, Johannesburg, South Africa* , 341pp.

Hastenrath, S. (2001). In search of zonal circulations in the equatorial Atlantic sector from the NCEP-NCAR reanalysis . *Int. J. Climatol., 21* , 37-48.

Hill, B. (1975). A simple general approach to inference about the tail of a distribution. *Annals of Statistics 3* , 1163-1174.

Holton, J. R. (1976). *An Introduction to Dynamic Meteorology, Second Edition.* Academic Press,New York,416 pp.

Jeanne, I., Randremanana, R., Robert, V., Ariey, F., Tombo, M., Wilme, L., et al. (2002). Biogéographie de Madagascar. In I. Pasteur, *Atlas évolutif du paludisme à Madagascar*. Antananarivo: Institut Pasteur Madagascar.

Johnson D.H., Mörth H.T. (1960). Forecasting research in East Africa. *Symposium de Nairobi* , 56-137.

Jury MR. (2002a). Development of statistical forecast models of summer climate and hydrological resources over Southern Africa. *Water Res Comm Report 903/1/02* , 116p.

Jury MR, Huang B. (2004). The Rossby wave as a key mechanism of Indian Ocean climate variability. *Deep Sea Res (in press)* .

Jury MR, Mulenga HM, Mason SJ, Brandao A. (1997). Development of objective statistical system to forecast summer rainfall over southern Africa. *WRC Report* , 45pp.

Jury, M., Mulenga, H., & Mason, S. (1999). Exploratory long-range models to estimate summer climate variability over southern Africa. *J. Clim., 12* , 1892-1899.

Kalnay et al. (1996). The NCEP/NCAR 40-Year Reanalysis Project. *Bulletin of the American Meteorological Society 77 (3)* , 437–471.

Kistler, R., and Coauthors. (2000). The NCEP–NCAR 50-Year Reanalysis. *Bull. Amer. Meteor. Soc., in press* .

Latif, M., & Barnet, T. (1995). Interactions of the tropical oceans. *J. Clim., 8* , 952-968.

Lin, Y-L. (2007). Mesoscale Dynamics. *Cambridge University Press; Sec. 9.3*

Lindesay J.A. (1988). South African rainfall, the Southern Oscillation and a southern hemisphere semi-annual cycle. *J. Climatol., 8* , 17-30 .

Lynch, S. D., & Schluze, R. E. (1995). Techniques for estimating areal daily rainfall. *Proc. Seventh Hydrological Sciences Symposium, Rhodes University, Grahamstown.* South Africa.

M.R. Jury, Raholijao. (1991). The climate of Madagascar and relationships to Southern Africa. *8th Annual Conference of South African Society for Atmospheric Science.*
Maj. Gary D. Atkinson. (1991). *Forecaster's guide to tropical meteorology (Second Edition).* Weather Graphics.

Marco A. Giorgetta. (2003). *Is there a feeedback of the QBO to the tropical meteorology?*

Max Planck Institute for Meteorology: Whistler.

Mark R. Jury, Dave B. Enfield, Jean Luc Mélice. (2002). *Tropical monsoons around Africa: Stability of El-Nino-Southern Oscillation associations and links with continental climate.* . Journal of Geophysical Research Vol.107.

Mason S.J., Lindesay J.A. (1993). A Note on the Modulation of Southern Oscillation - Southern African Rainfall Associations with the Quasi-Biennial Oscillation. *J. Geophys. Res., 98* , 8847-8850 .

Mason S.J., Tyson P.D. (1992). The modulation of sea surface temperature and rainfall associations over southern Africa with solar activity and the Quasi-Biennial Oscillation. *J. Geophys. Res., 97* , 5487-5856 .

Mason SJ. (2000). Definition of technical terms in forecast verification scores. *Available in the International Research Institute for Climate Prediction web site http://iri.ideo.Columbia.edu/outreach/publication/seminar/Quality* .

McKee, T.B., N.J. Doesken and J. Kleist. (1993). The Relationship of Drought Frequency and Duration to Time Scales. *8th Conference on Applied Climatology*, (pp. 179-184).

McPhaden, M.J. (1999). Genesis and evolution of the 1997-1998 El-Nino. *Science, 283* , 950-954.

Nicholson, S. (1997). An analysis of the ENSO signal in the tropical Atlantic and Western Indiana Oceans. *Int. J. Climatol., 17* , 345-375.

Nicholson, S.E. and J. Kim. (1997). The relationship of the El-Nino-Southern Oscillation to African rainfall. *Int. J. Climatol.,17* , 117-135.

Ogallo, L.J., J. E. Janowiak and M.S. Halpert. (1988). Teleconnection between seasonal rainfall over East Africa and global sea surface temperature anomalies. *J. Meteor. Soc. Japan, 66* , 807-821.

Pickands, J. . (1975). Statistical inference using extreme order statistics. *Annals of Statistics 3* , 119-131.

Purdue University Researchers. (2007). *Tropical Cyclones have role in climate-control* . Science Daily. Purdue News Rev.

Ramazan Gençay, Faruk Selçuk, Abdurrahman Ulugülyağc. (2001). *EVIM: A Software Package for Extreme Value Analysis.*

Ramiaranjanahary, O., Raholijao, N., Ratiarison, A., & Rabemanotrona. (2004). Contribution to the simulation of the orographic out-flow over Madagascar using a three dimensional model to mesoscale. *2nd High-Energy Physics conference in Madagascar*, (p. 5). Antananarivo.

Reason et al. (2000). ENSO and climatic signals across the Indian Ocean basin in the global context, part 1, Interannual composite patterns. *Int. J. Climatol., 20* , 1285-1327.

Reed, R.J., W.J. Campbell, L.A. Rasmussen and D.G. Rogers. (1961). Evidence of the downward-propagating annual wind reversal in the equatorial stratosphere . *J. Geophys. Res., 66* , 813-818.

Riehl, H. (1979a). Climate and Weather in the Tropics. *Academic Press, New York* , 611 pp.

Riehl, H. (1954). Tropical Meteorology. *McGraw-Hill, New York* , 392 pp.

Ropelewski, C.F. and M.S. Halpert. (1987). Global and regional scale precipitation pattern associated with El-Nino/Southern Oscillation . *Mon. Wea. Rev., 115* , 1606-1626.

Sadler, J.C. (1976a). Tropical cyclone initiation by the tropical upper tropospheric trough. *Dept. Meteor.Univ. Hawaii, UHMET 75-02* , 103 pp.

Slingo, J. M., & Annamalai, H. (2000). The El Niño of the century and the response of the Indian summer monsoon. *Mon. Wea. Rev* .

Thomson et al. (2001). A review of statistical methods for the meteorological adjustement. *Atmospheric Environment 35* , 617-630.

Trenberth, K. E., Branstator, G. W., Karoly, D., Kumar, A., Lau, N.-C., & Ropelewski, C. (1998). Progress during TOGA in understanding and modeling global teleconnections associated with tropical sea surface temperatures. *J. Geophys. Res* .

Trendafilov, N. T., & Joliffe, I. T. (2006). Projected gradient approach to the numerical solution of the SCoTLASS. *Computational Statistics & Data Analysis* , Pages 242-253.

Wallace, J. M., Rasmusson, E. M., Mitchell, T. P., Kousky, V. E., Sarachik, E. S., & Von

Storch, H. (1998). On the structure and evolution of ENSO-related climate variability in the tropical Pacific: Lessons from TOGA . *J. Geophys. Res* .

Webster, P.J., A.M. Moore, J.P. Loschnigg and R.R Leben. (1999). Coupled ocean-atmosphere dynamics in the Indian Ocean during 1997-1998. *Nature, 401* , 356-360.

Wilks, D. S. (1995). *Statistical methods in the atmospheric sciences.* Academic press, INC.

Xie, S-P., Annamalai, H., Friedrich A. Schott and J. P. MCCreary JR (2001). Structure and mechanisms of South Indian Ocean Climate Variability. *Journal of climate, vol 15* , 864-878.

Richard, Y.; S. Trzaska; P. Roucou and M. Rouault;. (2000). Modification of the southern African rainfall variability/ENSO relationship since the late 1960s . *Clim. Dyn, 16* , 883-895.

Yeshanew, A., & M. Jury. (2006c). North African climate variability. Part 3:resource prediction. *Theor. Appl. Climatol. (in press)* .

Yeshanew, A., & M. Jury (2006a). North African climate variability. Part 1: Thermocline coupling. *Theor. Appl. Clim (in press)* .

Yoeli, P. (1975). Compilation of data for computer-assisted relief cartography. *Davis, JC and McCullagh, MJ (Eds): Display and Analysis of Spatial Data (NATO Advanced Study Institute)* , Pg 352-367.

Zwiers, F.W., & Von Storch, H. (2004). On the role of statistics in climate research. *Intern. J Climatol.* , 24: 665–680.

Appendix 1) List of key areas used in Part II, Chap1

PC	Parameter	Variables	Acronym	Domain
1	OLR	North Atlantic OLR	nAolr	(40-20°W, 28-15°N)
1	OLR	South Atlantic OLR	sAolr	(45-20°W, 10-0°S)
1	OLR	West African OLR	wAfolr	(20-30°E, 15-5°N)
1	OLR	Southeast African OLR	sAfolr	(22-40°E, 5-25°S)
1	OLR	Indian Ocean OLR	Iolr	(55-65°E, 12-22°S)
1	OLR	Indian Ocean OLR	Iolr	(70-85°E, 5-17°S)
1	OMEGA	South America OMEGA	sAmo	(50-30°W, 0-12°S)
1	OMEGA	Northwest African OMEGA	nwAfo	(13°W-15°E, 34-16°N)
1	OMEGA	North African OMEGA	nAfo	(30-42°E, 38-28°N)
1	OMEGA	Northeast African OMEGA	nwAfo	(19-38°E, 14-40°N)
1	OMEGA	East African OMEGA	eAfo	(25-40°E, 5°N-5°S)
1	Specific humidity 500mb	Indian Ocean Q500	Iq500	(50-78°E, 7-17°S)
1	Specific humidity 500mb	North Indian Ocean Specific Humidity	nIq	(95-115°E, 15°N-5°S)
1	SST	South Atlantic SST	sAsst	(20°W-10°E, 0-17°S)
1	SST	North Pacific Ocean SST	nAsst	(50-25°W, 50-40°N)
1	SST	North Pacific Ocean SST	nAsst	(140-120°W, 20-10°N)
1	SST	North Pacific Ocean SST	nAsst	(150°W-140°E, 45-35°N)
1	SST	North Pacific Ocean SST	nAsst	(170°W-140°E, 50-60°S)
1	zonal wind 200mb	North Atlantic zonal wind	nAu200	(60°W-20°E, 30-20°N)
1	meridional wind 200mb	North Atlantic meridional wind	nAv200	(60°W-20°E, 30-20°N)
1	zonal wind 200mb	North Atlantic zonal wind	nAu200	(70-10°W, 50-38°N)
1	meridional wind 200mb	North Atlantic meridional wind	nAv200	(70-10°W, 50-38°N)
1	zonal wind 850mb	North Atlantic zonal wind	nAu850	(70-10°W, 50-38°N)
1	meridional wind 850mb	North Atlantic meridional wind	nAv850	(70-10°W, 50-38°N)
2	OLR	West Indian Ocean OLR	wIolr	(40-60°E, 2°N-18°S)
2	OLR	West Indian Ocean OLR	wIolr	(70-85°E, 2-14°S)
2	OLR	SouthAfrican OLR	sAfolr	(15-35°E, 15-25°S)
2	OLR	North Atlantic Ocean OLR	nAolr	(8°W-38°E, 10N,0°S)
2	OLR	North Atlantic Ocean OLR	nAolr	(40-10°W, 23-10°N)
2	OMEGA	West Indian Ocean OMEGA	w I O	(43-62°E, 3°N-18°S)
2	OMEGA	Southwest Indian Ocean OMEGA	swIO	(62-80°E, 32-48°S)
2	OMEGA	Southwest Indian Ocean OMEGA	swIO	(40-58°E, 42-55°S)
2	OMEGA	North African OMEGA	nAfo	(10°W-10°E, 10°N-0°S)
2	OMEGA	North African OMEGA	nAfo	(20-35°E, 12-3°N)
2	OMEGA	North Atlantic Ocean OMEGA	nAO	(40-30°W, 10°N,0°S)
2	OMEGA	Southwest Indian Ocean OMEGA	swIO	(70-90°E, 5-15°S)
2	Specific humidity 500mb	East African Specific Humidity	eAfq500	(20-90°E, 10°N-20°S)
2	Specific humidity 500mb	South African Specific Humidity	sAq500	(10-35°E, 20-30°S)
2	Specific humidity 500mb	North Atlantic Specific Humidity	nAq500	(55-50°W, 20-5°N)
2	Specific humidity 500mb	North Atlantic Specific Humidity	nAq500	(40°W-0°E, 5°N-5°S)

2	SST	South Indian Ocean SST	sIsst	(20-85°E, 30-50°S)
2	SST	South Indian Ocean SST	sIsst	(70-100oE, 20-40oS)
2	SST	South Indian Ocean SST	sIsst	(85-110°E, 10-20°S)
2	SST	South Atlantic SST	sAsst	(50-10°W, 30-60°S)
2	SST	North Atlantic SST	nAsst	(30-10°W, 5°N-5°S)
2	SST	North Atlantic SST	nAsst	(35-15°W, 20-5°N)
2	zonal wind 200mb	Southwest Indian Ocean zonal wind	swIu200	(50-60°E, 30-45°S)
2	zonal wind 200mb	South Atlantic zonal wind	sAu200	(30°W-10°E, 25-38°S)
2	zonal wind 200mb	North Atlantic zonal wind	nAfu200	(60-20°W, 40-10°N)
2	zonal wind 850mb	North African zonal wind	nAfu850	(0-30°E, 15°N-0°S)
2	meridional wind 200mb	Southwest Indian Ocean zonal wind	swIv200	(50-60°E, 30-45°S)
2	meridional wind 200mb	South Atlantic meridional wind	sAv200	(30°W-10°E, 25-38°S)
2	meridional wind 200mb	North Atlantic meridional wind	nAfv200	(60-20°W, 40-10°N)
2	meridional wind 850mb	North African meridional wind	nAfv850	(0-30°E, 15°N-0°S)
3	OLR	North African OLR	nAfolr	(0-20°E, 10°N-0°S)
3	OLR	South American OLR	sAmolr	(50-40°W, 25-35°S)
3	OMEGA	Northeast African OMEGA	neAfo	(30-50°E, 30-20°N)
3	OMEGA	North Atlantic OMEGA	n A o	(50-35°W, 35-15°N)
3	OMEGA	South Atlantic OMEGA	s A o	(50-40°W, 25-35°S)
3	Specific humidity 500mb	Northwest Indian Ocean Specific Humidity	nwIq	(55-90°E, 10°N-8°S)
3	Specific humidity 500mb	Southeast Indian Ocean Specific Humidity	seIq	(95-110°E, 23-33°S)
3	Specific humidity 500mb	North Atlantic Specific Humidity	nAq500	(55-35°W, 22-35°S)
3	SST	Southwest Indian Ocean SST	sIsst	(55-80°E, 25-35°S)
3	SST	Southwest Indian Ocean SST	sIsst	(40-70°E, 40-50°S)
3	SST	North Atlantic SST	nAsst	(60-20°W, 30-25°S)
3	zonal wind 200mb	North African zonal wind	nAfu200	(10-75°E, 30-20°N)
3	zonal wind 200mb	North Atlantic zonal wind	nAu200	(50-30°W, 35-25°N)
3	zonal wind 200mb	Southwest Indian Ocean zonal wind	swIu200	(30-70°E, 35-45°S)
3	meridional wind 200mb	North African meridional wind	nAfv200	(10-75°E, 30-20°N)
3	meridional wind 200mb	North Atlantic meridional wind	nAv200	(50-30°W, 35-25°N)
3	meridional wind 200mb	Southwest Indian Ocean meridional wind	swIv200	(30-70°E, 35-45°S)
3	zonal wind 850mb	South African zonal wind	sAfu850	(15-25°E, 5-15°S)
3	zonal wind 850mb	South African zonal wind	sAfu850	(17-27°E, 15-25°S)
3	zonal wind 850mb	Southwest Indian zonal wind	swIu850	(35-60°E, 32-42°S)
3	zonal wind 850mb	North Indian Ocean zonal wind	nIu850	(60-80°E, 5°N-5°S)
3	zonal wind 850mb	North Atlantic Ocean zonal wind	nAu850	(50-30°W, 35-25°N)
3	meridional wind 850mb	South African meridional wind	sAfv850	(15-25°E, 5-15°S)
3	meridional wind 850mb	South African meridional wind	sAfv850	(17-27°E, 15-25°S)
3	meridional wind 850mb	Southwest Indian meridional wind	swIv850	(35-60°E, 32-42°S)
3	meridional wind 850mb	North Indian Ocean meridional wind	nIv850	(60-80°E, 5°N-5°S)
3	meridional wind 850mb	North Atlantic Ocean meridional wind	nAv850	(50-30°W, 35-25°N)

2) Correlation between PCs and the extracted key areas variables

	PC1
PC1	1
nwAfo	-0,02
nAfo	0,42
nwAfo	0,09
eAfo	0,26
sAmo	0,26
Iq500	-0,01
nIq	0,14
nAu850	-0,27
nAv850	0,2
nAu200	-0,12
nAv200	0,15
nAu200	-0,32
nAv200	-0,18
wAfolr	0,02
sAfolr	0,18
Iolr	-0,14
Iolr	-0,04
nAolr	-0,28
sAolr	0,1
Isst	-0,2
nAsst	-0,04
nAsst	-0,12
nAsst	-0,11
nAsst	0,18
sAsst	-0,08

	PC2
PC2	1
nAfo	-0,14
nAfo	-0,06
w I O	-0,47
swIO	-0,28
swIO	0,24
swIO	0,23
nAO	0,31
eAfq500	-0,25
sAq500	0,14
nAq500	-0,09
nAq500	0,15
swIu200	-0,27
nAu200	-0,16
sAu200	-0,11
nAfu850	0,19
swIv200	-0,18
nAv200	0,14
sAv200	0,14
nAfv850	0,31
sAfolr	0,18
wIolr	0
wIolr	0,22
nAolr	-0,06
nAolr	0,24
sIsst	-0,01
sIsst	0,02
sIsst	-0,1
nAsst	-0,01
nAsst	0,09
sAsst	-0,09

	PC3
PC3	1
neAfo	0,19
n A o	-0,12
s A o	0,32
nwIq	0,14
seIq	-0,02
nAq500	-0,23
nAfu200	-0,32
swIu200	-0,04
nAu200	-0,07
sAfu850	-0,17
sAfu850	0,26
swIu850	0,11
nIu850	0,25
nAu850	0,03
nAfv200	0,01
nAv200	-0,04
swIv200	0,06
sAfv850	-0,03
sAfv850	0,26
swIv850	-0,11
nIv850	0,1
nAv850	0,03
nAfolr	-0,08
sAmolr	0,37
sIsst	0,13
sIsst	-0,17
nAsst	0,06